UNIVERSITÉ DU LUXEMBOURG

PhD-FSTM-2022-072

The Faculty of Sciences, Technology and Communication

DISSERTATION

Presented on 03.06.2022 in Esch-sur-Alzette

to obtain the degree of

DOCTEUR DE L'UNIVERSITÉ DU LUXEMBOURG EN PHYSIQUE

by

Sangita Dutta

Born on 14 March 1994 in Purulia, West Bengal (India)

First-principles investigation of ferroelectricity and related properties of HfO_2

Dissertation Defence Committee:

Dr. Jorge Íñiguez, **DissertationSupervisor**
Luxembourg Institute of science and Technology
Professor, Université du Luxembourg

Dr. Ludger Wirtz, **Chair**
Professor, Université du Luxembourg

Dr. Emmanuel Defay
Luxembourg Institute of Science and Technology

Dr. Silvia Picozzi, **Vice – Chair**
Consiglio Nazionale delle Ricerche - Superconducting and Other Innovative Materials and Devices Institute, Chieti, Italy

Dr. Matthieu Verstraete
Professor, University of Liege, Belgium

Affidavit

I hereby confirm that the PhD thesis entitled "First-principles investigation of ferroelectricity and piezoelectricity in HfO_2-based materials" has been written independently and without any other sources than cited.

Luxembourg, _____ _____

Name: Sangita Dutta

dedicated to my beloved father

Acknowledgements

My thesis will be incomplete if I do not acknowledge some individuals. It is my pleasure to thank those who directly or indirectly assisted and encouraged me during my Ph.D. studies.

First, I would like to convey my sincere thanks and gratitude to you, Prof. Jorge Íñiguez, my Ph.D. supervisor, for your guidance. Your endless support has made my Ph.D. journey smooth. I thank you, Jorge, for teaching the difficult things in a very simple way, which I could never imagine by myself. You are one of the best teachers in my life. You always taught me how to become independent in research, I don't know how much I became, but it was great learning in my life for sure. I know I wasn't always up to your skills or expectations, but I'm really grateful for what we have accomplished together. I have always heard that the thesis writing part is always stress full. However, the way you have supervised me, I did not feel stressed, and I really enjoyed the whole process. Thanks a lot for being a great supervisor in my Ph.D. Apart from research, I can never forget the first day I met you. It was my first experience outside my home country where every little thing was new for me, and you took me to all the shops to introduce where can I find what to survive my initial days. It was so touching for me, I can't thank you enough for that.

Next, I would like to thank the jury members, Dr. Silvia Picozzi and Dr. Matthieu Verstraete, for accepting to review and evaluate my thesis work and participating in my defense. Prof. Ludger Wirtz and Dr. Emmanuel Defay, thank you for being a part of my CETs and for bringing the questions that helped me better understand my work. Emmanuel, in the CET sessions, you always asked me about the experimental aspects of my simulation, which was quite beneficial and always forced me to consider the correlation between simulations and experiments. Thank you so much for that.

I take this opportunity to thank the group of Alexei Gruverman and the group José Silva for the fruitful collaboration during my Ph.D.

Special thanks to you, Hugo Aramberri, for your continuous support throughout my Ph.D. Thanks for being my sidekick in the first two projects. It was indeed very helpful. You have always helped me with every silly question I have asked you, whether it's about the simulations or future guidance. Thank you for bearing with me. I am really grateful to you for that. Also, thank you very much for reading my thesis and giving your feedback. It was a great help.

Thank you for being my sidekick in my last project, Natalya. We did not get much time to work together. However, it was great learning from you.

Next, I would like to thank the "Theory-Team", which includes Diana, John, Natalya, Monica, Hugo, Hong-Xin, Carlos, Mauro, and Jorge for the core-theoretical discussions in every meeting. Thank you, Jorge, for enforcing the rule, which requires everyone in the meeting to ask a question. Learning how to ask a decent question was quite beneficial to me. I have enjoyed being the chair of the meeting for one year. It would have been even nicer if we could meet in person. Special thanks to Carlos and Mauro for helping me in my

initial days in LIST.

Also, many thanks to you, Tony, for the useful discussion related to HfO_2.

Thanks to the whole FMT group, including the former members. Thanks, Emmanuel, for managing our group so nicely. I believe that the working environment of our FMT group is exceptionally good. I remained quiet during the group's outdoor activities, although I have enjoyed your company in all the activities I have attended.

Thanks to my present and former office mates, Carlos, Mauro, Cosme, Youri, Alvar, Christina, Naveen, Diana, Ashwath, Barnik, Hala, Andreas, and all the former interns for creating a nice working environment in the office and also for your help whenever I asked you something. Thank you so much Cosme for always helping me with Latex and some fundamental discussion. Thank you, Ashwath and Barnik, for discussing our ferroelectric course tasks and for reading my thesis. I have enjoyed taking the course with you people. You are the best juniors.

Thanks to Van-Mien Quang, the technician of LIST, for helping me install things on my Linux machine.

Another opportunity to express my gratitude to my wonderful friends Nikhar, Ahilan, Rutuja, and Mohit, whom I met in Luxembourg and who have now become my family. Despite being so far away from my family, they did not let me feel isolated from my family. Now, even if I am with my family in India, I miss my family in Luxembourg. Thank you so much, guys, for always being there for me. I truly, believe that you can work efficiently if you are happy. I can never forget those nights of our endless laughter in stupid jokes, and I am pretty sure that only we three can laugh at those jokes. I can't express how grateful I am to you, Nikhar, and Ahilan, two of my closest friends. You were always there to put a smile on my face, no matter how busy you were in your personal lives. It's hard to find such friends, and I am truly blessed. These days would not have been as memorable as now without you two. I also thank my other friends, Rohan, Arpan, Shweta, Shreyashi, and Sachin, for our fun nights and parties. I also want to express my gratitude to my friends, Rituparna and Sumanti, for always being there for me during my school and university days. Also, thank you both for proofreading my thesis.

Last but not least, I would like to thank my parents for teaching me how to fly high. Thank you so much for your unconditional love and endless belief in me. You are the reason I am who I am today. I would also like to thank you, Subham, my brother, for your love and silent support. Many thanks to my partner Debkumar for your unwavering support in achieving my dreams and also for being there whenever I needed you. Finally, I am grateful to all my family members for your constant support and belief in me. Without you, it would not be so successful.

Abstract

Nonvolatile memories are in increasing demand as the world moves toward information digitization. The ferroelectric materials offer a promising alternative for this. Since the existing perovskite materials have various flaws, including incompatibility with complementary metal-oxide-semiconductor processes in memory applications, the discovery of new optimized FE thin films was necessary. In 2011, the disclosure of ferroelectricity in hafnia (HfO_2) reignited interest in ferroelectric memory devices because this material is well integrated with CMOS technology. Although the reporting of ferroelectricity in HfO_2 has been a decade, researchers are still enthralled by this material's properties as well as its possible applications.

The ferroelectricity in HfO_2 has been attributed to the orthorhombic phase with space-group $Pca2_1$. This phase is believed to be the metastable phase of the system. Many experimental and theoretical research groups joined the effort to understand the root causes for the stability of this ferroelectric phase of HfO_2 by considering the role of the surface energy effects, chemical dopants, local strain, oxygen vacancies. However, the understanding was not conclusive. In this part of this work, we will present our first-principles results, predicting a situation where the ferroelectric phase becomes the thermodynamic ground state in the presence of a ordered dopant forming layers.

Since the main focus was on understanding and optimizing the ferroelectricity in HfO_2, we observed that the electro-mechanical response of the system has garnered comparatively less attention. The recent discovery of the negative longitudinal piezoelectric effect in HfO_2 has challenged our thinking about piezoelectricity, which was molded by what we know about ferroelectric perovskites. In this work, we will discuss the atomistic underpinnings behind the negative longitudianl piezoelectric effect in HfO_2. We will also discuss the behavior of the longitudinal piezoelectric coefficient (e_{33}) under the application of epitaxial strain, where we find that e_{33} changes sign even though the polarization does not switch.

Aside from a basic understanding of piezoelectric characteristics in HfO_2, the application aspect is also worth considering. The piezoelectric properties of the material can be tuned to meet the needs of the applications. In this work, we will describe our findings on how the piezoelectric characteristics of the material change as a function of isovalent dopants.

Index

List of Figures

List of Tables

Acronyms

CMOS: complementary-metal-oxide-semiconductor

Hafnia: HfO_2

FE: Ferroelectric

PE: Paraelectric

FET: field-effect transistor

RAM: random access memory

ALD: atomic layer deposition

BTO: $BaTiO_3$

PZT: $Pb(Zr,Ti)O_3$

PTO: $PbTiO_3$

MEMS: micro-electro-mechanical systems

DFT: Density Functional Theory

DFPT: density functional perturbation theory

LDA: Local Density Approximation

GGA: Generalized Gradient Approximation

PBE: Perdew-Burke-Ernzerhof

PW-91: Perdew-Wang

BLYP: Beeke-Lee-Yang-Par
PBE-sol: PBE adapted for solids

PW: Plane wave

BZ: Brillouin zone

MP: Monkhorst Pack

PP: Pseudopotential

PAW: Projector-augmented wave

VASP: Vienna ab initio Simulation Package

GS: ground state

PLD: pulse laser deposition

STEM: scanning transmission electron microscopy

ToF-SIMS: ime-of-flight secondary ion mass spectrometry

NLPE: negative longitudinal piezoelectric effect

PVDF: polyvinylidene fluoride

PFM: piezoresponse force microscopy

Chapter 1

Introduction

The thesis mainly focuses on the ferroelectricity and piezoelectricity of a novel ferroelectric (FE), hafnia (HfO_2). Before introducing the topic, we will discuss the basics of ferroelectricity and piezoelectricity along with their technological applications in this chapter. We will also discuss the appearance of HfO_2 as ferroelectric and piezoelectric. Finally, the main initial objective of the thesis and how it evolved with the progress of our research will be described.

1.1 Ferroelectricity

Ferroelectricity is a property of an insulating crystal or dielectric that shows spontaneous polarization, which must be switchable by the application of a suitable electric field [1]. A ferroelectric has two or more distinct stable or metastable states of different nonzero polarization.

In all the known ferroelectrics, spontaneous polarization is developed by the atomic arrangements of the atoms inside the crystal. Note that only a crystal with a polar space group can present a non-zero polarization. The polar crystal structure can be obtained through symmetry-breaking from a high-symmetry nonpolar reference structure. Thus, we can calculate the magnitude of the polarization (P_s) using the Born effective charges ($\boldsymbol{Z}$), and the atomic displacements ($\boldsymbol{u}$) from the reference state as follows [2]:

$$\boldsymbol{P_s} = \frac{1}{\Omega} \sum \boldsymbol{Z} \cdot \boldsymbol{u} \tag{1.1}$$

where Ω is the volume of the unit-cell. In most ferroelectrics, there is a phase transition from high-symmetry paraelectric to low-symmetric ferroelectric phase with decreasing temperature.

Figure 1.1 (a) shows the paraelectric (PE) to FE phase transition with temperature in a perovskite. In $PbTiO_3$, which is a representative well-known ferroelectric compound, the PE to FE phase transition occurs at 760 K with the development of spontaneous polarization of 75 $\mu C/cm^2$ [1]. The FE distortion due to the movements of the atoms from high-symmetry PE (cubic-$Pm\bar{3}m$) to low-symmetry FE (tetragonal-$P4mm$) phase of $PbTiO_3$ is shown in Figures 1.1 (b) and (c). The symmetry-breaking relationship between the high-symmetry PE phase and low-symmetry FE phase can be described by the Landau theory.

In Landau's theory [3, 4], the PE to FE phase transition is characterized by an order parameter (polarization P), which is zero in the high-symmetry phase and becomes finite

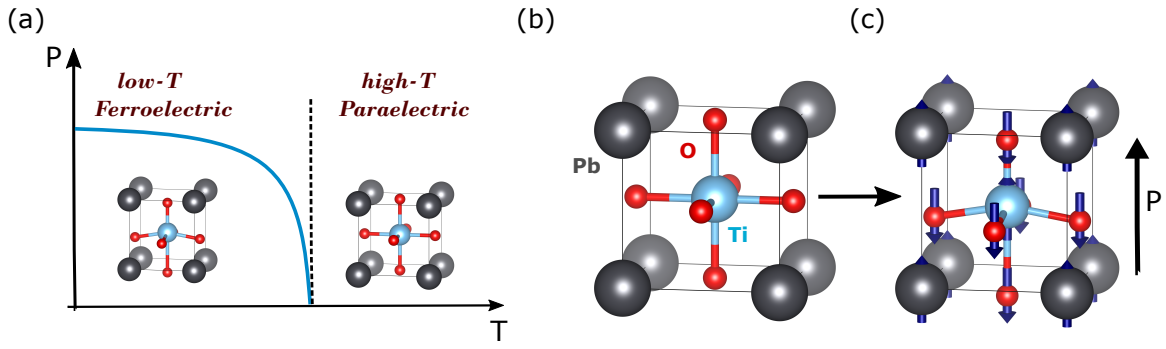

Figure 1.1: (a) Sketch of the ferroelectric (FE) to paraelectric (PE) phase transition in a perovskite. (b) Paraelectric cubic ($Pm\bar{3}m$) and (c) FE tetragonal phase ($P4mm$) of $PbTiO_3$. The atomic displacement in the FE phase with respect to the high-symmetry PE phase are shown by the arrows.The black arrow denotes the direction of polarization in $PbTiO_3$.

once the symmetry is lowered. We thus expand the free energy density $\mathcal{F}$ in the vicinity of the transition as a power series of the order parameter P as:

$$\mathcal{F}_P = \frac{1}{2}aP^2 + \frac{1}{4}bP^4 + \frac{1}{6}cP^6 - \mathcal{E}P \tag{1.2}$$

We choose the origin of energy of the unpolarized state to be zero.
In the Landau-Devonshire theory [3, 4], it is assumed that around the Curie point ($T \sim T_0$), only the coefficient a has a dependence with temperature, and the dependence is linear, $a = a_0(T - T_0)$. Thus, by substituting the value of a, Eq.1.2 becomes

$$\mathcal{F}_P = \frac{1}{2}a_0(T - T_0)P^2 + \frac{1}{4}bP^4 + \frac{1}{6}cP^6 - \mathcal{E}P \tag{1.3}$$

The equilibrium state can be found by minimizing the energy density with respect to P.

$$\frac{\partial \mathcal{F}_P}{\partial P} = 0 \tag{1.4}$$

Therefore,

$$\mathcal{E} = a_0(T - T_0)P + bP^3 + cP^5 \tag{1.5}$$

The dielectric susceptibility above transition temperature ($T > T_0$) can be obtained by differentiating Eq.1.5 with respect to $\mathcal{E}$, and then by setting $P = 0$ as follows:

$$\chi = \frac{\partial P}{\partial \mathcal{E}} = \frac{1}{a_0(T - T_0)} \tag{1.6}$$

and the dielectric stiffness will be

$$\kappa = \frac{1}{\chi} = a_0(T - T_0) \tag{1.7}$$

Typically, the coefficients a_0 and c are positive, whereas the sign of the b determines the type of the phase transition. [1].

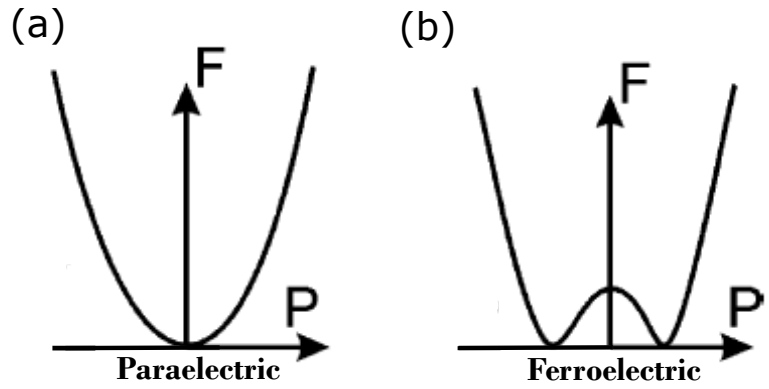

Figure 1.2: Free energy as a function of polarization in a (a) PE, and (b) FE state of material.

Second-order or continuous phase transition When b is positive, the free energy changes continuously with decreasing temperature. The second-order phase transition occurs at $T = T_0$. Figures 1.2 (a), (b) represent the free energy as a function of polarization in a paraelectric and ferroelectric state, respectively. In Figure 1.2 (b), the free energy has two minimum at $P = \pm P_0$. To the first approximation we assume $c = 0$, then the value of P_0 can be determined by setting $\mathcal{E} = 0$ in Eq.1.5.The value of P_0 will be:

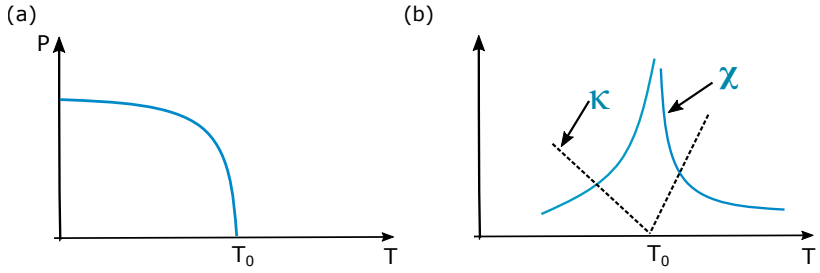

Figure 1.3: (a) Spontaneous polarization and (b) the dielectric susceptibility, dielectric stiffness as a function of temperature.

$$P_0 = [\frac{a_0}{b}(T_0 - T)]^{1/2} \tag{1.8}$$

The value of the dielectric susceptibility below the transition temperature ($T < T_0$) will be

$$\chi = \frac{1}{2a_0(T_0 - T)} \tag{1.9}$$

and the dielectric stiffness will be

$$\kappa = 2a_0(T_0 - T) \tag{1.10}$$

Therefore, κ vanishes at $T = T_0$, and the dielectric susceptibility diverges. Figure 1.3 (a) represents the polarization as a function of temperature. Figure 1.3 (b) shows the computed dielectric susceptibility and the dielectric stiffness at $P_0(T)$.

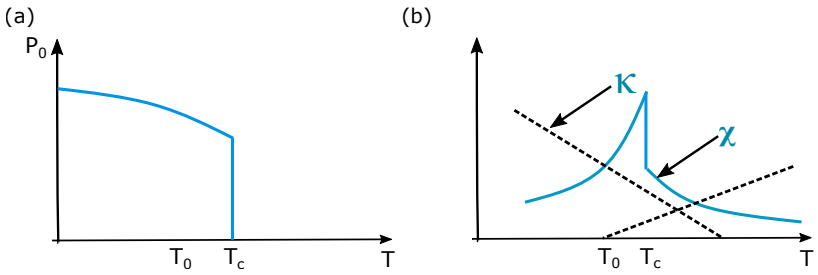

Figure 1.4: (a) Spontaneous polarization and (b) the dielectric susceptibility, dielectric stiffness as a function of temperature.

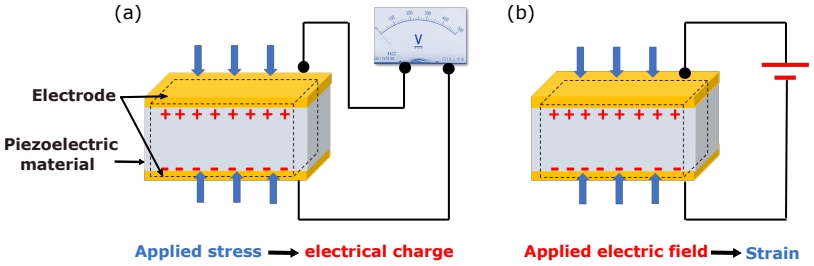

Figure 1.5: Schematic of (a) the direct piezoelectric effect and (b) the converse piezoelectric effect.

First order or discontinuous phase transition If the coefficient b in Eq.1.3 is negative, the free energy will have subsidiary minima with a finite value of P even at $T > T_0$. With decreasing the temperature, the energy of this minima will drop below that of the unpolarized state. This phenomenon occurs at $T = T_c$, known as Curie temperature. The Curie temperature T_c exceeds the tempertaure T_0. Importantly, the polarization drops to zero at T_c discontinuously. Figure 1.4(a) shows the polarization as a function of temperature. The dielectric stiffness does not vanish at T_0. The dielectric susceptibility has a finite jump as shown in Figure 1.4(b).

1.2 Piezoelectricity

Piezoelectricity is the accumulation of electric charge in the surfaces of a material with a non-centrosymmetric crystal structure in response to mechanical stress, or conversely, the generation of mechanical stress in the material in response to the electric field [5, 6]. The former is known as "the direct piezoelectric effect", and the latter is known as "the converse piezoelectric effect". Figures 1.5 (a) and (b) show the schematic of the direct and converse piezoelectric effect, respectively. The dielectric materials that exhibit this property are called piezoelectric materials. Among the 32 crystal classes, the 20 crystal classes show piezoelectricity. Ferroelectrics are a subgroup of piezoelectrics. Therefore all ferroelectrics are intrinsically piezoelectrics [6].

The piezoelectric strain coefficient ($d_{\alpha j}$) is defined as the change of polarization under mechanical stress, which reads

$$d_{\alpha j} = \frac{\partial P_\alpha}{\partial \sigma_j} \tag{1.11}$$

where α is the direction of the polarization P, and σ_j is the j^{th} component (in Voigt notation [7]) of mechanical stress σ. The piezoelectric stress coefficient is as follows:

$$e_{\alpha j} = \frac{\partial P_\alpha}{\partial \eta_j} \tag{1.12}$$

where η_j is the j^{th} component (in Voigt notation) of applied strain η. The relation between the the piezoelectric strain coefficient and piezoelectric stress coefficient is as follows

$$d_{\alpha j} = S_{jk} e_{\alpha k} \tag{1.13}$$

where S is the compliance tensor, which is inverse of the elastic tensor, and the summation runs over repeated indices.

Due to the tensorial nature of piezoelectricity, the electromechanical properties can be anisotropic. [5]. Thus, for the applications on sensors or actuators, it is important to identify the direction in which the piezoelectric effect is maximum.

1.3 Applications: Ferroelectrics & Piezoelectrics

In this section, we will discuss some representative applications of ferroelectrics and piezoelectrics.

1.3.1 Applications of Ferroelectrics

In the modern era of ferroelectricity, a variety of applications are available leveraging the bulk and thin film of ferroelectrics [8]. Particularly, the revolutionary applications of ferroelectrics are FE field-effect transistor (FE-FET) and FE random access memory (FE-RAM) [8, 9].

The principle of current conduction of an FE-FET is similar to that of the normal FET [10]. The typical FET is a three-terminal device that consists of a semiconductor channel with electrodes referred to as the drain and source at either end, as well as a control electrode known as the gate that is located relatively near to the channel [11]. The current flow happens in either a P-type or N-type semiconductor channel, known as P-channel and N-channel FETs, respectively. The conductance of the channel between source and drain is controlled by the application of potential on the gate [11]. In an FE-FET, the additional component is a ferroelectric insulator. Due to the spontaneous polarization of the ferroelectric, it can maintain the conductance of the channel even though the gate voltage is not applied. In addition, the polarization of the ferroelectric layer can be switched by providing a reverse gate voltage [10]. The reversible spontaneous polarization of ferroelectric is employed for the fast switching and low power operation in the binary logic devices.

Moreover, due to the ability of ferroelectrics to transit between two stable polarization states, these materials can be employed as an information storage medium. In FE-FET type RAM, a ferroelectric layer is directly incorporated into the transistor gate stack [12–14]. Figure 1.6 shows the basic structure of the FE-FET type RAM cell, which is also known as 1T-type memory. The ferroelectric memory offers non-volatility, high endurance, low power operation, due to which it becomes attractive for mobile applications [10, 14–16].

In this regard, it's worth noting that complementary metal-oxide-semiconductor (CMOS) technology is widely used in the manufacture of integrated circuits [17, 18]. Because of its

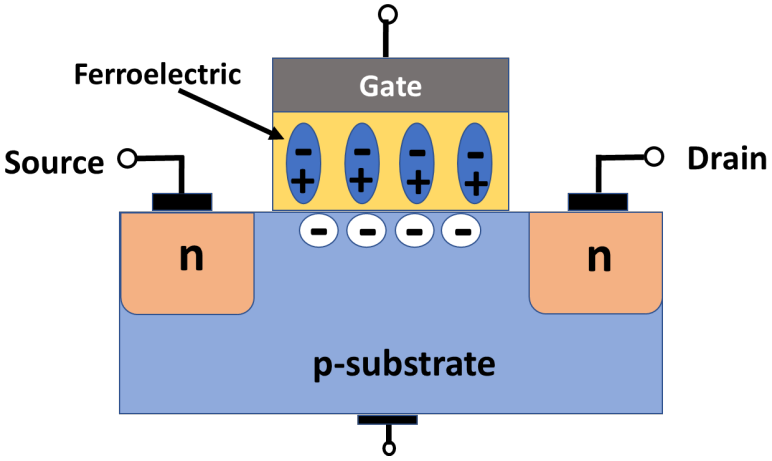

Figure 1.6: Schematic of the basic structure of an FE-FET type RAM cell adapted from Ref.[12]

multiple advantages, this technology is employed in microprocessors, microcontrollers, memory chips, and other digital logic circuits, batteries, and digital sensors. The key benefits of CMOS are low power consumption and noise immunity. Thus, all components of a microelectronic device ideally should be CMOS-compatible, which means they can be produced using the same silicon electronics manufacturing procedures.

Although the perovskites have very well-suited ferroelectric properties, they are readily CMOS-compatible, which is a disadvantage to be used in FE-RAM and microelectronic devices. Perovskite ferroelectrics underwent substantial development and are currently regarded as the front-up solution in ferroelectric memory fabrication to fulfill the requirement of CMOS integration [10, 15, 16]. Nonetheless, such perovskite systems need sophisticated integration strategies and face scaling limits on memory cells that have yet to be overcome. This leads to an imbalance between memory performance on one hand and manufacturing and R&D expenses on the other. Since then, ferroelectric memories has been limited to specialized markets.

However, the interest in FE-RAM has been renewed after the discovery of ferroelectricity in HfO_2-based materials [19]. Due to the CMOS compatibility of this material [20], it becomes a very promising candidate in the application of microelectronic devices. The possibility of growing high-quality HfO_2 thin films and excellent control in the film thickness using the atomic layer deposition (ALD) technique finally help to solve the scaling issue in the memory technology. The material is also well integrated into 3D structures, which helps to continue the FE-FET scaling and produce it in non-planar topologies, such as the FinFET, 3D array designs [12]. Thus, HfO_2-based ferroelectrics are projected to establish successful FE-FET devices, which could be a competitive idea for future memory applications.

1.3.2 Applications of Piezoelectrics

Piezoelectrics convert electric energy into mechanic energy or vice versa. The direct piezoelectric effect, where the mechanical energy is converted into electrical energy, has applications on sensors, automobile industries, medical technologies, energy harvesters [21]. The converse piezoelectric effect, where the electric energy is transformed into mechanic energy,

has applications on actuators, acoustic devices, noise cancellation, robotics, and piezoelectric motors [21]. The piezoelectric ceramics such as $BaTiO_3$ (BTO), $Pb(Zr,Ti)O_3$ (PZT), $PbTiO_3$ (PTO) are widely used for these applications.

The single crystal piezoelectrics such as quartz, $LiNbO_3$, $LiTaO_3$ are essential for the applications on frequency stabilized oscillators and surface acoustic devices [22]. Recently, single crystals of $Pb(Mg_{1/3}Nb_{2/3})O_3$ (PMN), $Pb(Zn_{1/3}Nb_{2/3})O_3$ (PZN) show promising behavior for applications in ultrasonic transducers, and electro-mechanical actuators [22]. Apart from that, due to the good piezoelectric properties, lightweight, and soft elasticity, the piezoelectric polymers like, e.g., polyvinylidene difluoride (PVDF), have applications on ultrasonic hydrophones, nanogenerators, and directional microphones [22, 23].

Nevertheless, the discovery of novel piezoelectrics is becoming increasingly crucial for finding lead-free materials to advance the new technologies. However, searching for a replacement of standard piezoelectric like PZT with a large piezoelectric response has been difficult. It has been found that the potassium sodium niobate (KNN) could be a potential candidate to replace PZT; but the material costs massive environmental damage in its early stage of the life cycle [21, 24].

Recently, AlN has gained tremendous attention due to its CMOS compatibility, excellent acoustic properties, and good piezoelectric properties, which are very important in the applications on micro-electro-mechanical systems (MEMS) devices [25–30].

In addition, thin films of ZnO have promising applications on acoustic and surface acoustic devices, MEMS devices, and microwaves [26, 31–34]. The synthesized functional ZnO nanostructures show applications on optoelectronics, nanosensors, and biomedical sciences [31].

Novel ferroelectric HfO_2 can be an important candidate as a lead-free piezoelectric. The thin films of HfO_2 can be easily grown with the desired properties, which is a great advantage from the application's point of view. Although the piezoelectric coefficient is very small in HfO_2 compared to PZT, it could compete with ZnO and AlN in the applications of acoustic devices, nanosensors, and MEMS technology.

1.4 The emergence of HfO_2

From the mid-90s, extensive research was focused on the scaling issues in microelectronic engineering. Additionally, the industry was starving for a viable "high-k" dielectric to substitute SiO_2 in the integrated gate and capacitor dielectrics [20]. In the last decade, HfO_2 was introduced by Intel as a dielectric layer for CMOS applications, generating massive development initiatives in the field of microelectronic semiconductor devices [20, 35]. At normal pressure, the material was known to exist in three distinct crystal phases: a monoclinic phase at room temperature, a tetragonal phase at 2050 K, and a cubic phase above 2803 K [19]. Interestingly, in 2011, Böscke et.al. claimed ferroelectricity in Si-doped HfO_2 [19]. The announcement of ferroelectricity in the material was highly surprising since the material had previously been employed as a paraelectric. Moreover, this material is the first binary oxide to exhibit a ferroelectric behavior [36].

Figure 1.7 (a) presents the structure of the ferroelectric phase with polarization pointing upward. The $P-E$ hysteresis loop taken from Ref.[16] is presented in Figure 1.7 (b).

The origin of ferroelectricity in HfO_2 has been attributed to the most widely recognized orthorhombic phase with spacegroup $Pca2_1$ [19]. However, the ferroelectric orthorhombic phase is a metastable phase of the system [37, 38]. Many research efforts had been made

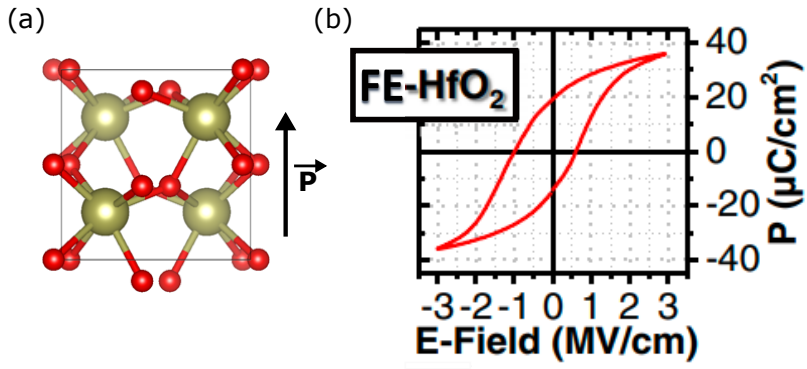

Figure 1.7: (a) The structure of ferroelectric phase of HfO_2 with polarization pointing upward. (b) P − E hysteresis loop in HfO_2-ZrO_2 solid solution. Figure (b) is taken from Ref.[16]

to stabilize this ferroelectric phase of HfO_2.

1.4.1 Technological importance of HfO_2

The development and industrial implementation of memory technologies had been suffering due to the lack of the proper choice and engineering of the ferroelectric material. The discovery of ferroelectricity in HfO_2 has greatly revived the interest in the field of next-generation high-density nonvolatile memories. Due to the CMOS compatibility, high scalability, and ease of processing technology, this material expands the material choice for ferroelectric memories as well as nanoscale ferroelectric devices [10, 12, 15, 16, 39–41].

Parameter	SBT [16, 42–44]	PZT [16, 44, 45]	HfO_2 [16, 46–48]
Film thickness (nm)	>25	>70	5-30
Annealing temperature (°C)	>750	>600	450-1000
P_r (μC/cm^2)	<10	20-40	1-40
E_c (kV/cm)	10-100	∼50	1000-2000
Dielectric constant	150-250	∼1300	∼30
ALD capability	limited	limited	mature
CMOS compatibility	poor	poor	stable

Table 1.1: The crucial parameters for the applications in microelectronic devices of ferroelectric HfO_2 compared to classic ferroelectric perovskites.

The most significant parameters to describe the ferroelectric behavior of any material are the coercive field E_c and the remanent polarization P_r. However, in the application, to determine the suitable ferroelectric for microelectronic engineering, additional features like CMOS compatibility, scalability, thermal budget requirement for processing, and thin-film technologies are equally significant and critical.

Table 1.1 shows the important parameters for the applications in microelectronic devices of HfO_2 in comparison to the traditionally used ferroelectrics. Due to the complexity and limitations in the thickness reduction of the usual perovskites, ferroelectric memories have faced several challenges. This issue can be overcome by considering ferroelectric HfO_2 as a suitable material choice since the ferroelectric characteristics are stable at lower film

thickness in ferroelectric HfO_2 [16, 49]. In addition, the easy integration in the CMOS environment makes HfO_2 an appropriate material choice for high-density ferroelectric devices.

Importantly, the value of the coercive field strength is very large in ferroelectric HfO_2 as compared to the other ferroelectrics (see Table 1.1). Due to the very large coercive field, the HfO_2-based devices need more power to operate. Hence, we partly loose the low-power feature of perovskite ferroelecrtics. Thus, the high coercive field of HfO_2 needs to be critically reviewed for reliability and low voltage operation.

Besides the memory applications, the CMOS compatibility, negative capacitance, and electro-mechanical response of HfO_2 have considerable promise in other applications [5, 16]. Due to the thickness scalability and well integrability in CMOS technology, HfO_2 could be a potential candidate in MEMS application. Apart from that, ferroelectric tunnel junctions and other resistive switching phenomena depending on polarization necessitate ferroelectrics like HfO_2[16].

1.4.2 Remaining Challenges

Although HfO_2 shows great advantages in terms of thickness scalability, CMOS compatibility, and mature deposition technique, the issues regarding wake-up effect, imprint, and insufficient endurance are still not solved [41].

Wake-up effect: Typically the woken-up state is needed to observe the FE behavior in HfO_2 thin films[50, 51]. The wake-up effect refers to the increment of the remanent polarization with an increasing number of switching electric-field cycles. The ferroelectric perovskites also exhibit this effect, but the number of electric field cycles to the woken-up state is one magnitude less than that of HfO_2 thin films, where the field cycling number is 10^3-10^5 cycles to get the maximum P_r [50, 52]. Many research work has been focused on the origin of this wake-up effect [13, 49–55] in HfO_2.

It has been reported that the asymmetric distribution of high oxygen vacancy concentration near the electrode can create an inhomogeneous internal electric field in the pristine material. These oxygen vacancies are redistributed into the bulk areas of ferroelectric-HfO_2-based films owing to the electric field cycling process, in which case the wake-up process will occur [52, 53].

Alternately, Lomenz et al. claimed that the wake-up effect occurs due to the field-cycling-induced phase transition [54]. They mentioned that the phase transition from tetragonal to ferroelectric-orthorhombic is responsible for this effect, which follows a decrease in dielectric constant and increases in remanent polarization with increasing the number of field cycles [13, 54, 55].

Park et al. reported that the annealing temperature has a significant effect on the wake-up phenomenon [49]. It has been found that the cycle numbers necessary to wake up $(Hf,Zr)O_2$ thin films drop as the annealing temperature rises, with a higher P_r in the pristine condition [49]. Such trend has also been reported in Si-doped HfO_2 and La-doped HfO_2 [56, 57].

In addition, the doping concentration and the electrode material are also important factors, which affect the degree of the wake-up effect [49, 58]. Although the wake-up effect is attributed to several factors mentioned above, further study is needed to better understand and control this phenomenon.

Insufficient Endurance: Apart from the wake-up effect, another critical issue of the ferroelectric HfO_2 is limited endurance, which means that the lifetime of the material is limited during field cycling. The best field cycling endurance recorded to date in ferroelectric-HfO_2-based thin films is 4×10^{10}, which is significantly lower than that in perovskite-based ferroelectrics (10^{15}) [41, 59]. The value of the E_c in HfO_2 films varies between 1-2 MV/cm [59–62] . Thus, to achieve the saturated $P-E$ curve, an electric field of 3 MV/cm or more is required. On the other hand, the breakdown strength of the HfO_2 films is around 3.5-5 MV/cm [59, 63], which leaves a narrow margin to secure the films after applying the allowed number of cycles before breakdown.

Due to the polycrystalline nature of the HfO_2 sample, nanoscale grain size has been observed [57, 64]. Because of the small grain size, the grain border area-to-volume ratio is high. Thus, the Oxygen vacancies tend to accumulate near the grain boundaries. The endurance of FE-HfO_2 can be enhanced by increasing the grain size, according to the literature [41]. However, the impact of grain size on endurance has yet to be thoroughly investigated.

The doping concentration also has an impact on the endurance of the HfO_2 film. It has been observed that the $H_{1-x}Zr_xO_2$ film with x=0.5 shows the largest value of P_r, but the smallest number of field cycles to a hard breakdown [41]. Nevertheless, the effect of doping concentration on endurance has not been clearly understood.

Based on the literature, it is possible to improve the endurance by lowering the oxygen vacancy [41] and annealing temperature [49, 54, 56]. Additionally, fabricating ferroelectric-HfO_2 films with the desired orientation or a high ferroelectric phase fraction could also help to increase the endurance [41, 59]. However, an extensive study in this regard is required.

Stability of ferroelectric phase: The ferroelectric phase of HfO_2 is believed to be metastable at ambient conditions [37, 38]. The nanoscale crystal grain size was previously found to be critical for the stability of hafnia's ferroelectric phase [65]. However, it results in a high density of unavoidable structural defects in HfO_2-based ferroelectrics, which obscured the intrinsic ferroelectricity of the material [65]. Additional mechanisms such as surface energy [66], local strain [67, 68], oxygen-vacancies [69, 70] have been suggested to enhance the stability of the ferroelectric phase. Moreover, according to the experimental reports, chemical dopants (Si, [19] La[57], Y [71], Zr [72], Al [73]) play an important role in stabilizing this phase. However, all the first-principles studies claimed that dopant alone can not stabilize the phase [68, 74–78]. Recently, the bulk crystal of ferroelectric Y-doped HfO_2 has been reported [79]. The group of Cheong has obtained transparent single crystals of up to 50 mm in length and up to 2 g in mass [79], whereas the previous experimental study reported the ferroelectric HfO_2 films with thicknesses of up to 1 μm [80]. However, the value of the remanent polarization in bulk-$HfO2_2$ is about 6 $\mu C/cm^2$, which is very low compared to what is observed in nanoscale Y-doped HfO_2 thin films (of about 24 $\mu C/cm^2$) [71]. This finding opens an additional research front to explore.

Thus, understanding and controlling the stability of the ferroelectric orthorhombic phase of HfO_2 is still a challenge. Moreover, finding the way to stabilize this phase at room temperature is an open question, which might also help to eliminate the lingering issues regarding wake-up and insufficient endurance.

Imprint: Besides the wake-up effect and limited endurance, the imprint is also a drawback in FE-HfO_2 films. An imprint of a ferroelectric is defined as a shift in the hysteresis

characteristics along the voltage axis and the loss of remanent polarization [41, 81]. By far, the issue regarding imprint is less studied than the ones above.

Imprint is a temperature-dependent phenomenon. It mainly occurs due to the stronger charge trapping at one of the interfaces between the ferroelectric and one of the two electrodes [81]. Therefore, the optimization of the interface structural qualities is essential to reduce or eliminate the impact of imprint[81, 82]. A more specific investigation related to temperature dependence is also needed.

Improving the piezoelectric properties: Due to the favorable elastic, dielectric, ferroelectric and piezoelectric properties, PZT remains the mainstream among the piezoelectric materials [21, 83]. In addition to PZT, PTO, and $PbNb_2O_6$ have also been used in the applications for their well-suited piezoelectric properties [83]. However, the lead content in these materials has a negative effect on the human body and eco system [21, 83]. Thus, searching lead-free piezoelectrics becomes increasingly important. In this context, HfO_2 could be an important candidate. Although the piezoelectric coefficient of this material is comparable with AlN and ZnO, it is very low compared to the lead-based piezoelectrics. Thus, to replace lead-based piezoelectrics, optimization of the piezoelectric properties of HfO_2 is required.

It has been reported in the literature that there is a field induced phase transition from tetragonal phase to the ferroelectric phase in HfO_2 [54]. Recently, M.Falkowski et al. have studied this field induced piezoelectric activity in HfO_2 [84]. They have reported that the piezoelectric coefficient in Si-doped HfO_2 increases one order of magnitude compared to its crytalline coefficient. Therefore, a more elaborate study in this regard by considering the defect states is needed. In addition, it is an open challenge to find the other possible ways to tune the piezoelectric coefficient of HfO_2 to make it suitable for the applications.

1.5 Objectives

HfO_2-based ferroelectric has been dubbed as "The ferroelectrics of the future" due to its capability of retaining ferroelectric properties in a few nanometers film-thickness and excellent CMOS-compatibility. However, the mechanisms of the ferroelectric phase formation in HfO_2 are still being explored. This thesis work is focused on the basic understanding of ferroelectricity and piezoelectricity in HfO_2.

Ever since the discovery of ferroelectricity in HfO_2, the semiconductor industry started investigating the potential of the material for applications in ferroelectric memory. On the other hand, the ferroelectric community has focused on understanding and controlling the ferroelectricity of the material. In comparison, the electro-mechanical response properties of HfO_2 have garnered little attention. The thesis work was originated with the aim of studying the electro-mechanical response properties of the material. However, our goal and activities have evolved with time, as reflected by the contents of this manuscript.

In the following, we will discuss the structure of the thesis.

In Chapter 2, we will describe the methodology used in this work.

In Chapter 3, we will discuss our results about the structural properties and relative energies of all the polymorphs of HfO_2 and ZrO_2 reported experimentally and theoretically to date. Since HfO_2 and ZrO_2 share very similar structural properties and polymorphs, we have included ZrO_2 too in this part. We have performed this piece of work to get familiar

with the materials properties and theoretical methods. Our results are compared with the previously reported values in order to make sure that we obtain reliable data.

Next, on the course of optimizing the electro-mechanical response of hafnia with dopants, we realized that some dopants have very strong preferences towards ordering inside the HfO_2 lattice, which left us curious to know the effect of the ordering of the dopants in stability of the ferroelectric phase of HfO_2. The obtained results from this study will be addressed in Chapter 4.

Next, we started focusing on the electro-mechanical response properties of HfO_2. While calculating the piezoelectric properties, we discovered that the material presents a negative longitudinal piezoelectric effect, which deviates from the behavior of the well-known perovskites ferroelectrics. At the very same time, this finding got published in the literature. However, in our opinion we still lacked a satisfying understanding of this negative piezoresponse. In chapter 5, we will discuss the atomistic underpinnings of this effect in pure HfO_2.

Chapter 6 presents our preliminary results on how the dopants affect the piezoelectric response of HfO_2.

Finally, in Chapter 7, we will summarize the main results and make some general remarks about this thesis work. In addition, we will provide an outlook of this work for the future.

Chapter 2

Methodology

We use first-principles Density Functional Theory (DFT) as our theoretical tool to perform all the calculations in this thesis. DFT is very popular due to its versatility in calculating various properties of a material. This method remains a mainstay in electronic structure calculations for maintaining a balance between accuracy and computational costs. Nowadays, a variety of DFT codes are available which can predict the structural, electronic, magnetic as well as thermal properties of a wide range of materials. Due to the recent development in computer technology and software, the calculations of more complex systems have become possible. In this thesis, we use DFT to calculate structural and electromechanical properties of HfO_2-based materials.

In the first part of this chapter, we discuss the formulation of the linear response properties, which includes the force-constant matrix, dielectric tensor, piezoelectric tensor of an insulating crystal. Then, in the second part, we will describe the framework of the DFT approaching the many-body problems. Finally, we will provide the technicalities to perform a successful DFT simulation. In the end, we will mention the additional methodological details which have been used in this work.

2.1 Linear-response formalism for electromechanical properties

In this section, we discuss the formalism of the response properties of a material provided by Vanderbilt and co-workers [85]. We consider a reference structure of an insulating crystal with cell volume Ω_0 which is in equilibrium at vanishing macroscopic electric field. Now, we expand the energy $E(\boldsymbol{u},\ \eta,\ \mathcal{E})$ as a function of atomic displacements u_m where m is a composite index representing atoms and displacement direction, homogeneous strain η_j where j is in Voigt notation ($j = 1...6$), and an applied electric field $\mathcal{E}_\alpha$ where α are the cartesian directions ($\alpha = x, y, z$) around the reference system as follows:

$$\begin{aligned} E(u,\mathcal{E},\eta) = E_0 + A_m u_m + A_\alpha \mathcal{E}_\alpha + A_j \eta_j + \frac{1}{2} B_{mn} u_m u_n + \\ \frac{1}{2} B_{\alpha\beta} \mathcal{E}_\alpha \mathcal{E}_\beta + \frac{1}{2} B_{jk} \eta_j \eta_k + B_{m\alpha} u_m \mathcal{E}_\alpha + B_{mj} u_m \eta_j \\ + B_{\alpha j} \mathcal{E}_\alpha \eta_j + \text{terms of higher order} \end{aligned} \tag{2.1}$$

where E_0 represents the energy density of the reference structure. In this equation, the first-order coefficients A_m, A_α and A_j are the forces (F_m=$-\Omega_0 A_m$); polarizations (P_α=$-A_\alpha$) and stresses ($\sigma_j = A_j$), respectively. Let us assume that the atomic coordinates and strains are fully relaxed in the reference system. Therefore, the coefficients A_m and A_j are zero. The elementary block-diagonal second-order coefficients B_{mn}, $B_{\alpha\beta}$, and B_{jk} in Eq. 2.1 correspond to force-constant matrix, dielectric susceptibility and elastic tensor, respectively, while the off-diagonal coefficients $B_{m\alpha}$, B_{mj}, and $B_{\alpha j}$ correspond to Born effective charges, force response internal strain tensor, and piezoelectric tensor, respectively.
With appropriate signs and cell-volume factors, the elementary second-derivative response-function tensors are defined as follows:

$$\Phi_{mn} = \Omega_0 \frac{\partial^2 E}{\partial u_m \partial u_n}\bigg|_{\mathcal{E},\eta} \tag{2.2}$$

where the Φ_{mn} defines the force-constant matrix.

$$\bar{\chi}_{\alpha\beta} = -\frac{\partial^2 E}{\partial \mathcal{E}_\alpha \partial \mathcal{E}_\beta}\bigg|_{u,\eta} \tag{2.3}$$

where the $\bar{\chi}_{\alpha\beta}$ is the purely-electronic or frozen-ion contribution of the dielectric susceptibility.

$$\bar{C}_{jk} = \frac{\partial^2 E}{\partial \eta_j \partial \eta_k}\bigg|_{u,\mathcal{E}} \tag{2.4}$$

where the $\bar{C}_{jk}$ defines the frozen-ion elastic tensor.

$$Z_{m\alpha} = -\Omega_0 \frac{\partial^2 E}{\partial u_m \partial \mathcal{E}_\alpha}\bigg|_{\eta} \tag{2.5}$$

where the $Z_{m\alpha}$ defines the Born effective charges.

$$\Lambda_{mj} = -\Omega_0 \frac{\partial^2 E}{\partial u_m \partial \eta_j}\bigg|_{\mathcal{E}} \tag{2.6}$$

where the Λ_{mj} defines the force-response internal strain tensor. and

$$\bar{e}_{\alpha j} = -\frac{\partial^2 E}{\partial \mathcal{E}_\alpha \partial \eta_j}\bigg|_{u} \tag{2.7}$$

where $\bar{e}_{\alpha j}$ defines the part of the piezoelectric tensor that accounts for the frozen-ion response. The quantities with the bar such as $\bar{\chi}_{\alpha\beta}$, $\bar{C}_{jk}$, and $\bar{e}_{\alpha j}$ are computed with fixed relative ionic coordinates.

Relaxed-ion tensors

To obtain the physical static response properties of the material, we must consider the relaxation of the ionic coordinates. We can define the corresponding relaxed-ion quantities by introducing the functional

$$\tilde{E}(\mathcal{E}, \eta) = min_u E(u, \mathcal{E}, \eta) \tag{2.8}$$

by setting $\partial E/\partial u_n = 0$ and assuming a stable reference system with zero net forces (A_m=0) in Eq. 2.1 we get,

$$0 = B_{nm} u_m + B_{n\alpha} \mathcal{E}_\alpha + B_{nj} \eta_j \tag{2.9}$$

Therefore,

$$u_m = -(B^{-1})_{mn}[B_{nj}\eta_j + B_{n\alpha}\mathcal{E}_\alpha] \tag{2.10}$$

Now, by substituting the value of u_m in Eq.2.1, we get

$$\begin{aligned}
\tilde{E}(\mathcal{E},\eta) &= E_0 + A_\alpha\mathcal{E}_\alpha + A_j\eta_j + \frac{1}{2}B_{mn}[(B^{-1})_{ml}(B_{l\alpha}\mathcal{E}_\alpha + B_{lj}\eta_j)] \\
&\quad [(B^{-1})_{nl}(B_{l\alpha}\mathcal{E}_\alpha + B_{lj}\eta_j)] + \frac{1}{2}B_{\alpha\beta}\mathcal{E}_\alpha\mathcal{E}_\beta + \frac{1}{2}B_{jk}\eta_j\eta_k \\
&\quad - B_{m\alpha}(B^{-1})_{ml}[B_{l\beta}\mathcal{E}_\beta + B_{lj}\eta_j)]\mathcal{E}_\alpha \\
&\quad - B_{mj}(B^{-1})_{ml}[B_{l\alpha}\mathcal{E}_\alpha + B_{lk}\eta_k]\eta_j + B_{\alpha j}\mathcal{E}_\alpha\eta_j + ... \\
&= E_0 + A_\alpha\mathcal{E}_\alpha + A_j\eta_j + \frac{1}{2}[B_{n\alpha}\mathcal{E}_\alpha + B_{nj}\eta_j] \\
&\quad [(B^{-1})_{nl}(B_{l\beta}\mathcal{E}_\beta + B_{lk}\eta_k)] + \frac{1}{2}B_{\alpha\beta}\mathcal{E}_\alpha\mathcal{E}_\beta + \frac{1}{2}B_{jk}\eta_j\eta_k \\
&\quad - B_{m\alpha}(B^{-1})_{ml}[B_{l\beta}\mathcal{E}_\beta + B_{lj}\eta_j)]\mathcal{E}_\alpha \\
&\quad - B_{mj}(B^{-1})_{ml}[B_{l\alpha}\mathcal{E}_\alpha + B_{lk}\eta_k]\eta_j + B_{\alpha j}\mathcal{E}_\alpha\eta_j + ... \\
&= E_0 + A_\alpha\mathcal{E}_\alpha + A_j\eta_j + \frac{1}{2}B_{n\alpha}(B^{-1})_{nl}B_{l\beta}\mathcal{E}_\alpha\mathcal{E}_\beta + \frac{1}{2}B_{n\alpha}(B^{-1})_{nl}B_{lk}\mathcal{E}_\alpha\eta_k \\
&\quad + \frac{1}{2}B_{nj}(B^{-1})_{nl}B_{lk}\eta_j\eta_k + \frac{1}{2}B_{nk}(B^{-1})_{nl}B_{l\alpha}\mathcal{E}_\alpha\eta_k \\
&\quad + \frac{1}{2}B_{\alpha\beta}\mathcal{E}_\alpha\mathcal{E}_\beta + \frac{1}{2}B_{jk}\eta_j\eta_k - B_{m\alpha}(B^{-1})_{ml}[B_{l\beta}\mathcal{E}_\beta + B_{lj}\eta_j)]\mathcal{E}_\alpha \\
&\quad - B_{mj}(B^{-1})_{ml}[B_{l\alpha}\mathcal{E}_\alpha + B_{lk}\eta_k]\eta_j + B_{\alpha j}\mathcal{E}_\alpha\eta_j + ...
\end{aligned} \tag{2.11}$$

The relaxed-ion tensors are defined as:

$$\chi_{\alpha\beta} = -\frac{\partial^2\tilde{E}}{\partial\mathcal{E}_\alpha\partial\mathcal{E}_\beta}\bigg|_\eta \tag{2.12}$$

$$C_{jk} = \frac{\partial^2\tilde{E}}{\partial\eta_j\partial\eta_k}\bigg|_\mathcal{E} \tag{2.13}$$

and

$$e_{\alpha j} = -\frac{\partial^2\tilde{E}}{\partial\mathcal{E}_\alpha\partial\eta_j}\bigg|_u \tag{2.14}$$

By performing the differentiation with respect to the electric field in the Eq.2.11 we get,

$$-\frac{\partial^2\tilde{E}}{\partial\mathcal{E}_\alpha\partial\mathcal{E}_\beta}\bigg|_\eta = -\frac{1}{2}B_{\alpha\beta} + \frac{1}{2}B_{m\alpha}(B^{-1})_{ml}B_{l\beta} \tag{2.15}$$

Thus, by inserting the appropriate sign and cell volume factor and by using Eq.(2.2-2.7), we find the relaxed ion dielectric susceptibility tensor

$$\chi_{\alpha\beta} = \bar{\chi}_{\alpha\beta} + \Omega_0^{-1}Z_{m\alpha}(\Phi^{-1})_{mn}Z_{n\beta} \tag{2.16}$$

Similarly, we obtain the relaxed ion elastic and piezoelectric tensors as follows:

$$C_{jk} = \bar{C}_{jk} - \Omega_0^{-1}\Lambda_{mj}(\Phi^{-1})_{mn}\Lambda_{nk} \tag{2.17}$$

$$e_{\alpha j} = \bar{e}_{\alpha j} + \Omega_0^{-1} Z_{m\alpha} (\Phi^{-1})_{mn} \Lambda_{nj} \tag{2.18}$$

$e_{\alpha j}$ in Eq. 2.18, is also known as the piezoelectric stress coefficient; whereas the piezoelectric strain coefficient ($d_{\alpha j}$) is defined as

$$d_{\alpha j} = \left. \frac{\partial P_\alpha}{\partial \sigma_j} \right|_{\mathcal{E}} \tag{2.19}$$

and typically this quantity $d_{\alpha j}$ is directly accessible in experiments. The relation between $d_{\alpha j}$ and $e_{\alpha j}$ is as follows:

$$d_{\alpha j} = S_{jk}^{(\mathcal{E})} e_{\alpha k} \tag{2.20}$$

where S_{jk}=C_{jk}^{-1} represents the compliance tensor.

To compute the response properties of any material, DFT along with density functional perturbation theory (DFPT) [86] have been proven to give a successful description for a wide range of materials. Using the finite-differences approach, we may directly compute several properties from DFT, such as effective charges, force-constant matrices, and elastic constants. However, the DFPT methods provide the desired response properties in a more automated way without multiple ground-state calculations. In this thesis, we use DFPT based methods to calculate the response properties of the material. The detailed implementation of DFPT within DFT is not discussed here. The interested reader can find the full description in references [86–90]. In the following sections, we will discuss the basic framework of the DFT and the technicalities to perform a DFT simulation.

2.2 DFT approaching many-body problems

In principle, one can obtain the properties of our system of interest by solving the non-relativistic time-independent Schrödinger equation, which is given by:

$$\hat{H}\psi[\{\boldsymbol{r_i}\}, \{\boldsymbol{R_I}\}] = E\psi[\{\boldsymbol{r_i}\}, \{\boldsymbol{R_I}\}] \tag{2.21}$$

where $\hat{H}$ is the many-body Hamiltonian, $\psi[\{\boldsymbol{r_i}\}, \{\boldsymbol{R_I}\}]$ is the many-body wavefunction and E is the energy of the system. The total Hamiltonian of such a system is:

$$\begin{aligned}
\hat{H} = & -\sum_{i=1}^{N} \frac{\hbar^2}{2m} \nabla_i^2 - \sum_{I=1}^{K} \frac{\hbar^2}{2M_I} \nabla_I^2 - \sum_{i}^{N} \sum_{I}^{K} \frac{Z_I}{\mid \boldsymbol{r_i} - \boldsymbol{R_I} \mid} + \sum_{i}^{N} \sum_{i \neq j}^{N} \frac{1}{\mid \boldsymbol{r_i} - \boldsymbol{r_j} \mid} \\
& + \sum_{I}^{K} \sum_{I \neq J}^{K} \frac{Z_I Z_J}{\mid \boldsymbol{R_I} - \boldsymbol{R_J} \mid} \\
& = \hat{T}_e + \hat{T}_n + \hat{V}_{ne} + \hat{V}_{ee} + \hat{V}_{nn}
\end{aligned} \tag{2.22}$$

where $\boldsymbol{r_i}$ is the position of the i^{th} electron, $\boldsymbol{R_I}$ is the position of the I^{th} nuclei, m is the mass of electrons, and M_I is the mass of the I^{th} nuclei. $\hat{T}_e$ and $\hat{T}_n$ are the kinetic energy operators yielding kinetic energy of the electrons and nuclei. $\hat{V}_{ne}$, $\hat{V}_{ee}$, and $\hat{V}_{nn}$ represent the Coulomb interaction between electron-nuclei, electron-electron and nuclei-nuclei respectively.

At the very beginning of quantum mechanics, Born and Oppenheimer made an approximation to the many-body Schödinger equation [91]. According to this approximation, we

assume that the electrons are moving in a system with static nuclei due to the heavier (order of $\sim 10^3$-10^5 times) mass of the nuclei compared to the electron, which helps to decouple the electronic and nuclear problems. Therefore, the many-electron Schrödinger equation becomes:

$$\left[-\sum_{i=1}^{N} \frac{\hbar^2}{2m} \nabla_i^2 - \sum_{i}^{N} \sum_{I}^{K} \frac{Z_I}{\mid \boldsymbol{r_i} - \boldsymbol{R_I} \mid} + \sum_{i}^{N} \sum_{i \neq j}^{N} \frac{1}{\mid \boldsymbol{r_i} - \boldsymbol{r_j} \mid} \right] \phi([\{r_i\}]) = E\phi([\{r_i\}]) \quad (2.23)$$

where $\phi[\{\boldsymbol{r_i}\}]$ is the many-electron wavefunction. The electronic hamiltonian is

$$\hat{H}_e = \hat{T}_e + \hat{V}_{ne} + \hat{V}_{ee} \quad (2.24)$$

Despite the fact that Eq. 2.23 is exact in the non-relativistic regime, it is impossible to solve it except for some trivial cases. The many-electron wavefunction is a function of $3N$ variables. So it is totally beyond the capability of today's computers to solve the many-body wavefunction for a system containing large number of electrons. Thus we need an approximation that can ease the problem of solving the many-body Schrödinger equation by retaining the important information about the system as much as possible.

In 1964 Hohenberg and Kohn proposed a theory called DFT, which eventually led to a revolution in quantitative modeling of the electronic-structures [92]. According to this theory, all the ground-state properties can be expressed as a function of the electronic density, where the electron density is a function of three variables i.e. three space coordinates.

Then the total energy functional can be written as:

$$E[\rho] = T_e[\rho] + \int \rho(\boldsymbol{r}) V_{ext}(\boldsymbol{r}) d\boldsymbol{r} + \frac{1}{2} \int \int \frac{\rho(\boldsymbol{r})\rho(\boldsymbol{r'})}{\mid \boldsymbol{r} - \boldsymbol{r'} \mid} d\boldsymbol{r} d\boldsymbol{r'} + E_{xc}[\rho] \quad (2.25)$$

where $\rho(\boldsymbol{r})$ is the electron density and the terms in the right-hand side of Eq. 2.25 represent the kinetic energy $T_e[\rho]$, the interaction energy coming from the external potential (nuclei-electron interaction energy), the Hartree energy (Coulomb interaction energy), and the exchange-correlation energy of the system. $E[\rho]$ can be minimized with respect to the variations in electron density to find the exact ground-state density and energy of the system.

Kohn and Sham assumed an ansatz that the ground-state density of the interacting system will be equal to that of the sum of fictitious non-interacting systems. This assumption leads to the single-particle Kohn-Sham (KS) equations for the non-interacting system.

$$[\hat{T}_e + \hat{V}_{ext} + \hat{V}_H + \hat{V}_{xc}] \phi_i^{\mathrm{KS}}(\boldsymbol{r_i}) = \epsilon_i^{\mathrm{KS}} \phi_i^{\mathrm{KS}}(\boldsymbol{r_i}) \quad (2.26)$$

where $\hat{V}_{ext}$ and $\hat{V}_H$ denote the external potential and the Hartree potential respectively. Therefore, the KS hamiltonian is

$$\hat{H}^{\mathrm{KS}} = [\hat{T}_e + \hat{V}_{ex} + \hat{V}_H + \hat{V}_{xc}] = [\hat{T}_e + \hat{V}_{\mathrm{eff}}] \quad (2.27)$$

where $\phi^{\mathrm{KS}}(\boldsymbol{r_i})$ is the KS orbitals and ϵ^{KS} is the eigenvalues of the $\hat{H}^{\mathrm{KS}}$. These KS equations can be solved self-consistently to obtain the eigenvalues and eigenfunctions as shown in figure 2.1.

Exchange-Correlation Functional

The exact form of the exchange-correlation (xc) term in the KS hamiltonian is not known. Therefore, the development of the approximations of E_{xc} has resulted in a new field of study. The basic approximations generally used to describe the E_{xc} terms are the Local Density Approximation (LDA) and Generalized Gradient Approximation (GGA).

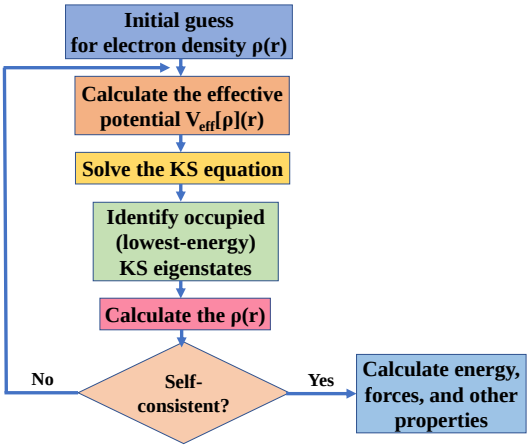

Figure 2.1: Flow chart of Self-consistent scheme in DFT calculation

Local Density Approximation (LDA)

This approximation [93] is based on the model of the homogeneous electron gas. LDA assumes that the charge density of a given system varies slowly so that a localized region behaves like a homogeneous electron gas. Therefore, E_{xc} depends only on the electron density at position $\boldsymbol{r}$. The expression of the xc-functional within LDA can be written as:

$$E_{xc}^{\mathrm{LDA}}[\rho(\boldsymbol{r})] = \int \rho(\boldsymbol{r})\varepsilon_{xc}^{\mathrm{homo}}(\rho(\boldsymbol{r}))d\boldsymbol{r} \tag{2.28}$$

Therefore, the exchange-correlation potential will be

$$\tilde{V}_{xc}(\boldsymbol{r}) = \frac{\delta E_{xc}[\rho(\boldsymbol{r}]}{\delta\rho(\boldsymbol{r})} = \frac{\partial[\rho(\boldsymbol{r})\varepsilon_{xc}^{\mathrm{homo}}(\rho(\boldsymbol{r}))]}{\partial\rho(\boldsymbol{r})} = \varepsilon_{xc}^{\mathrm{homo}}(\rho(\boldsymbol{r})) + \rho(\boldsymbol{r})\frac{\partial\varepsilon_{xc}^{\mathrm{homo}}(\rho(\boldsymbol{r}))}{\partial\rho(\boldsymbol{r})} \tag{2.29}$$

For the homogeneous electron gas, the analytical expression for the exchange term is

$$\tilde{V}_x[\rho(\boldsymbol{r})] = -\frac{3}{4}\left(\frac{3}{\pi}\right)^{1/3}\int \rho(\boldsymbol{r})^{4/3}d\boldsymbol{r} \tag{2.30}$$

However, there is no analytical expression for the correlation energy. The correlation energy can be obtained numerically from quantum Monte Carlo methods [93]. Finally, the $\tilde{V}_{xc}(\boldsymbol{r})$, the xc-potential is parametrised in terms of the xc-energy density of homogeneous electron gas, ε_{xc}^{homo}.

Generalised Gradient Approximation (GGA)

In GGA, a better approximation is made by capturing the local and semilocal information of any system. It tries to incorporate the effects of inhomogeneity by considering the gradient of the electron density. Therefore, the E_{xc} depends on the electron density and its gradient at a given point $\boldsymbol{r}$. The xc-functional in this approximation [94] can be written as:

$$E_{xc}^{\mathrm{GGA}}[\rho(\boldsymbol{r})] = \int \rho(\boldsymbol{r})\varepsilon_{xc}^{\mathrm{homo}}(\rho(\boldsymbol{r}), \Delta\rho(\boldsymbol{r}))d\boldsymbol{r} \tag{2.31}$$

There are many xc-functionals within GGA available in the literature. e.g. Perdew-Burke-Ernzerhof (PBE)[94], Perdew-Wang (PW91)[95], Becke-Lee-Yang-Par(BLYP)[96, 97]. Among them, the PBE version of the GGA is the most commonly used in solid-state calculations.

Although the GGA xc-functional maintains a balance between computational efficiency and accuracy, PBE overestimates the lattice constants by approximately 1%. Hence the other equilibrium properties such as bulk moduli, and spontaneous polarization are also off. Therefore, a better approximation is required for solids with slowly varying densities. Recently an efficient approach for the lattice properties has been developed by modifying the PBE functional. This PBE functional adapted for solids (PBE-sol) yields better lattice constants and lattice properties than PBE [98]. We employ the PBE-sol functional in all the calculations carried out in this thesis except in Chapter 3 where we use LDA and PBE functionals to reproduce the literature.

2.3 Technicalities of a typical DFT simulation

In this section, we will discuss about the main technicalities that are necessary to perform a DFT calculation.

2.3.1 Periodic supercells and K-point Sampling

In the previous section, we discussed how the many-body problem can be mapped into equivalent single-particle problems. Nevertheless, it is still not trivial how to deal with the crystals, which is consist of an infinite number of atoms arranged in a periodic manner. To work with such a system implies the calculations of an infinite number of wavefunctions associated with the infinite number of electrons.

This problem is surmounted by performing calculations on a periodic system and using Bloch's theorem to the electronic wavefunctions. Bloch's theorem states [99, 100] that *'the wavefunction of an electron $\phi_{j,\boldsymbol{k}}(\boldsymbol{r})$, within a periodic potential, can be written as the product of a lattice periodic part $u_{j\boldsymbol{k}}(\boldsymbol{r})$ and a wavelike part $e^{i\boldsymbol{k}\cdot\boldsymbol{r}}$'*.

$$\phi_{j,\boldsymbol{k}}(\boldsymbol{r}) = \mathrm{e}^{i\boldsymbol{k}\cdot\boldsymbol{r}} u_{j\boldsymbol{k}}(\boldsymbol{r}) \tag{2.32}$$

where $\boldsymbol{k}$ is the wave vector. The cell-periodic part can be expanded using a basis set consisting of a discrete set of plane waves whose wave vectors are reciprocal lattice vectors. Here, the cell-periodic part is expanded by using a particular basis set known as the plane-wave (PW) basis set as follows:

$$u_{j\boldsymbol{k}}(\boldsymbol{r}) = \sum_{G} C_{j,\boldsymbol{k}}(\boldsymbol{G}) exp[i\boldsymbol{G}\cdot\boldsymbol{r}] \tag{2.33}$$

Where $\boldsymbol{G}$ is the reciprocal lattice vector and $C_{j,\boldsymbol{k}}(\boldsymbol{G})$ is a coefficient for the plane waves.

The wave vector $\boldsymbol{k}$ is considered as a continuous variable in the limit of a crystal. All the possible eigenstates of the Hamiltonian are given by a set of k-points within the primitive cell of the reciprocal space called the Brillouin zone (BZ). Among the infinite number of electronic states, only a finite number of states are occupied at each k-point. Therefore, by using Bloch's theorem, the problem of computing an infinite number of electronic states has been converted in calculating a finite number of electronic states at an infinite number of k-points. Since the electronic wavefunctions are very similar for the k-points that are close together, the wavefunctions over a region of k-space can be represented by the wavefunctions at a single k-point. Thus the total number of terms to be summed over is converted into a BZ summation over a finite number of k-points called special k-points.

Next, the critical part is to sample a set of special k-points in the BZ, which must follow two criteria:

- select k-points as few as possible to reduce computational cost.
- it should be enough to represent the actual quantity adequately and accurately.

Here, we use Monkhorst Pack(MP) [101] to sample the k-points. It generates a grid of k-points which are evenly spaced throughout the BZ. Using this method, we can get accurate results for insulators and semiconductors by considering a relatively small number of k-points. However, a denser k-point grid is required in a metallic system to define the Fermi surface precisely. Therefore, the convergence of the k-point grid for a given property is important.

2.3.2 The Basis set

It is not easy to treat the KS orbitals mathematically. Therefore, a set of basis functions are required to expand the KS orbitals. Here, we consider the PW basis sets also mentioned above, which are nonlocal and span over the system.

The basis set of a electronic wave-function in a periodic potential can be written under the Bloch's theorem [99] as :

$$\phi_{j\boldsymbol{k}}(\boldsymbol{r}) = \sum_{\boldsymbol{G}} C_{j,k}(\boldsymbol{G}) exp[i(\boldsymbol{k}+\boldsymbol{G})\cdot\boldsymbol{r}] \tag{2.34}$$

By increasing the size of the PW basis set, systematic improvement of convergence and accuracy is possible.

In principle, to represent the expansion of the wavefunction precisely, we need an infinite number of PWs. However, the plane wave coefficients $\mathrm{C}_{j,\boldsymbol{k}}(\boldsymbol{G})$ with higher kinetic energy are less important. Therefore, it is possible to truncate the PW basis set by introducing a proper cut-off energy (E_{cut}). In practice, the introduction of a finite E_{cut} gives a finite plane wave basis-set, and the E_{cut} is defined as:

$$E_{\mathrm{cut}} \geqslant \frac{\hbar^2}{2m} |\ \boldsymbol{k}+\boldsymbol{G}\ |^2 \tag{2.35}$$

Thus only the PWs with kinetic energy smaller than E_{cut} are included in the calculations. The cut-off energy is system-dependent. Therefore it is important to check the convergence of E_{cut} to get accurate results.

2.3.3 The Pseudopotential

Most of the physical properties are controlled by the valence electrons to a greater extent than the core electrons of a system. The core electrons are strictly bounded with the nucleus in a deep potential well, whereas the valence electrons far from the nucleus are rather active in most of the circumstances. These valence electrons take part in forming bonds, being ionized, conducting electricity in metals, etc. To reduce the computational cost in describing the potential created by the core electrons and nuclei, we exploit the pseudopotential (PP) approach. Figure 2.2 illustrates the basic principle of the PP.

By introducing a proper core radius (r_{cut}), the core and the valence part are separated in the classic PP approach. At $r < r_{\mathrm{cut}}$ the core part remains frozen. The valence wave-functions at $r < r_{\mathrm{cut}}$ oscillate rapidly because of the strong effective potential of the core part. This oscillation of the wavefunction in the core region is replaced by the smooth and

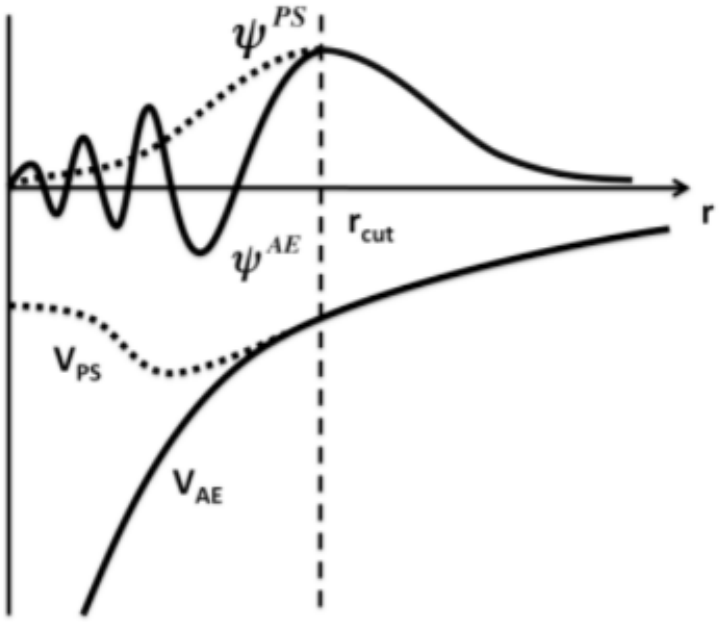

Figure 2.2: Schematics of the basic principle of the PP scheme. The solid line and the dashed line represent the all-electron (AE) potential and the PP and their corresponding wavefunctions, respectively. At r_{cut}, the PP and pseudo wavefunctions are identical to that of the AE potenial and its corresponding wavefunctions [100].

nodeless wavefunctions as shown in Figure 2.2. The pseudo wavefunctions and the corresponding potential for the valence part remain identical to the actual wavefunctions and potential outside the core region.

There are several approaches to determine the PP, namely norm-conserving PPs [102–104], ultrasoft-PP [105], projector-augmented wave (PAW) scheme [106], etc. The basic idea of the PP scheme explained above has been applied to the original PP method (norm-conserving PP). However, in addition to the primary principle, the concepts of constructing PP have evolved with time. In the PAW scheme, the efficiency of the PP and accuracy of the all-electron potential have been maintained. The valence part of the PAW is presented by the expansion of PWs and the core part is projected on a radial grid at the atom center. This PAW scheme allows good convergence with much smaller basis sets. In this thesis, we consider the PAW scheme proposed by Blöchl in the 90s [106]

2.3.4 Convergence study

DFT is a successful theory to characterize the properties of many materials. Yet, it needs some convergence study in choosing the energy cut-off for PW basis sets, density of the k-point mesh, and the number of valence electrons explicitly considered in the simulation.

As regards the last point, in this work we have adopted typical choices in the literature on hafnia and transition metal oxides treated with the PAW method. Thus, we consider the following electrons explicitly in the calculations; 2s and 2p for oxygen, 6s and 5d for Hf (we use 5s, 5p, 6s and 6d for Hf in Chapter 5 & 6), 4s, 4p, 5s, and 4d for Zr, 3s and 3p for Si, 5d, 6s, and 6p for Pb, 3p, 4s, and 3d for Ti, 3d, 4s, and 4p for Ge. All our

results seemed perfectly reliable and consistent with previous theoretical calculations and experimental information; thus, we did not explore other choices.

As regards the cut-off for the PW basis set, the more plane waves that are incorporated in a specific calculation, the better the wavefunctions are represented. Similarly, the density of the k-point mesh largely controls the BZ integration, which has an important role in getting accurate results. However, the higher the density of the k-point grid and the value of E_{cut}, the higher the computational cost. Finding an optimum density of the k-point grid and E_{cut} within a specific tolerance is a significant part of any DFT calculations. In principle, the convergence of E_{cut} and k-point grid needs to be checked for the properties of interest of a given system (e.g. lattice parameter, dielectric constant, elastic constant).

Here we consider the usual ferroelectric phase (orthorhombic-$Pca2_1$) of HfO_2 to perform the convergence study. The structural and electromechanical properties of the ferroelectric phase in this material are of special interest in this thesis work. Therefore we study the convergence of lattice parameters and the dielectric tensor to determine the optimized value of E_{cut} and k-point grid.

All the calculations are carried out within the DFT framework as implemented in the Vienna ab initio Simulation Package (VASP) [107, 108]. We perform a structural relaxation of the ferroelectric structure of the material, where we allow the system to relax until the residual forces fall below 0.01 eV/Å and residual stresses fall below 0.1 GPa. Here we show the convergence of the properties mentioned above using LDA, PBE, and PBE-sol xc-functional. Figures 2.3 (a), (b), and (c) show the lattice parameters of the ferroelectric phase of HfO_2 for different choices of E_{cut} and k-point grid. Figures 2.3 (d,e,f), show the corresponding relative error for each functional. We calculate the relative error by considering the value corresponding to the highest considered E_{cut} and k-point grid as reference.

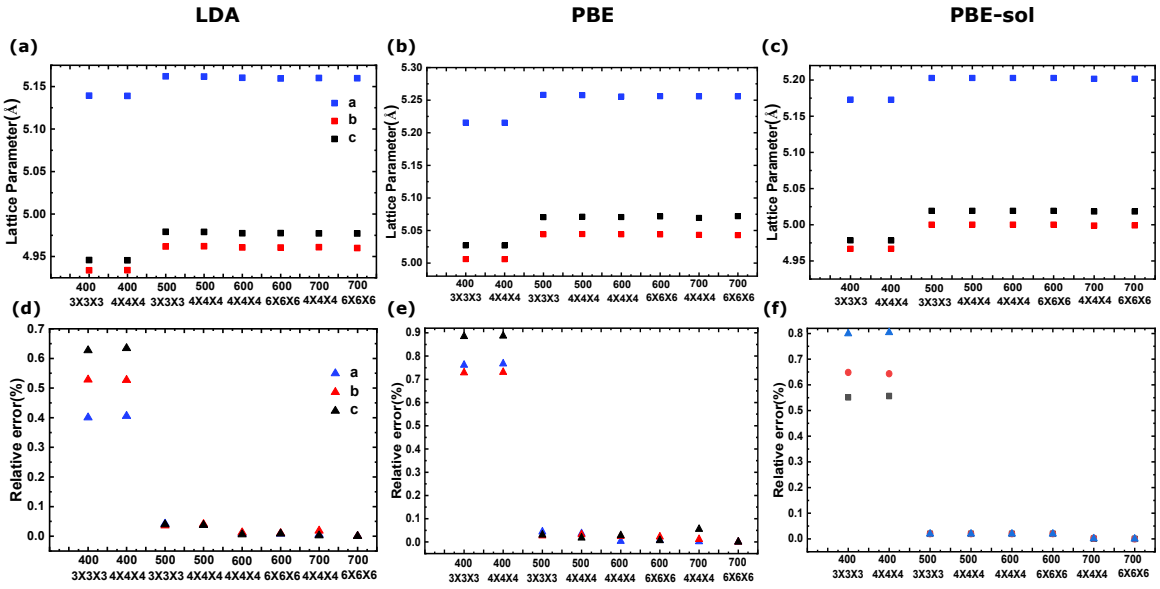

Figure 2.3: Convergence in E_{cut} and k-point grid of lattice parameters of the ferroelectric phase by using three different xc-functionals (a) LDA (b) PBE and (c) PBE-sol. In the second row, we show the relative error as a function of E_{cut} and k-point grid with respect to the highest E_{cut} and k-point grid considered. We show the results for three xc-functionals (d) LDA) (e) PBE and (f) PBE-sol.

From Figure 2.3, we find that E_{cut} = 500 eV and 3×3×3 k-point grid is giving well-converged results with less than 0.1% error for the lattice parameters irrespective of the xc-functional. The value of the lattice parameters of the ferroelectric phase using this E_{cut} and k-point grid are tabulated in Table 2.1. The calculated lattice parameters are in reasonable agreement with previous literature for all the xc-functionals as shown in Table 2.1.

Lattice Parameter	LDA		PBE		PBE-sol	
	This work	Ref. [109]	This work	Ref. [110]	This work	Ref. [111]
a	4.96	5.02	5.04	5.01	5.00	5.00
b	5.16	5.22	5.26	5.24	5.20	5.21
c	4.98	5.04	5.07	5.05	5.02	5.02

Table 2.1: Computed lattice parameters of the ferroelectric phase of HfO_2 in Å using LDA, PBE and PBE-sol xc-functionals with E_{cut} = 500 eV and 3×3×3 k-point grid . The values of the lattice parameters are in well agreement with the literature.

Next, we check the convergence of the dielectric tensor. Figures 2.4 (a), (b), and (c) show the three non-zero diagonal components of the dielectric tensor as a function of E_{cut} and k-point grid for the three xc-functionals. Similarly, the relative errors are calculated and presented in Figures 2.4 (d), (e), and (f) . In this case, we also observe that E_{cut} = 500 eV and 3×3×3 k-point grid is showing good convergence in dielectric tensor with less than 1 % error for all the three xc-functionals. Therefore, 500 eV cut-off and 3×3×3 k-point grid yield well converged structural and response properties of HfO_2. We also check the convergence of the lattice parameter and dielectric tensor in ZrO_2 (HfO_2 and ZrO_2 present very similar physical and chemical-bonding features.). We find the same optimized values of E_{cut} and k-point grid in ZrO_2.

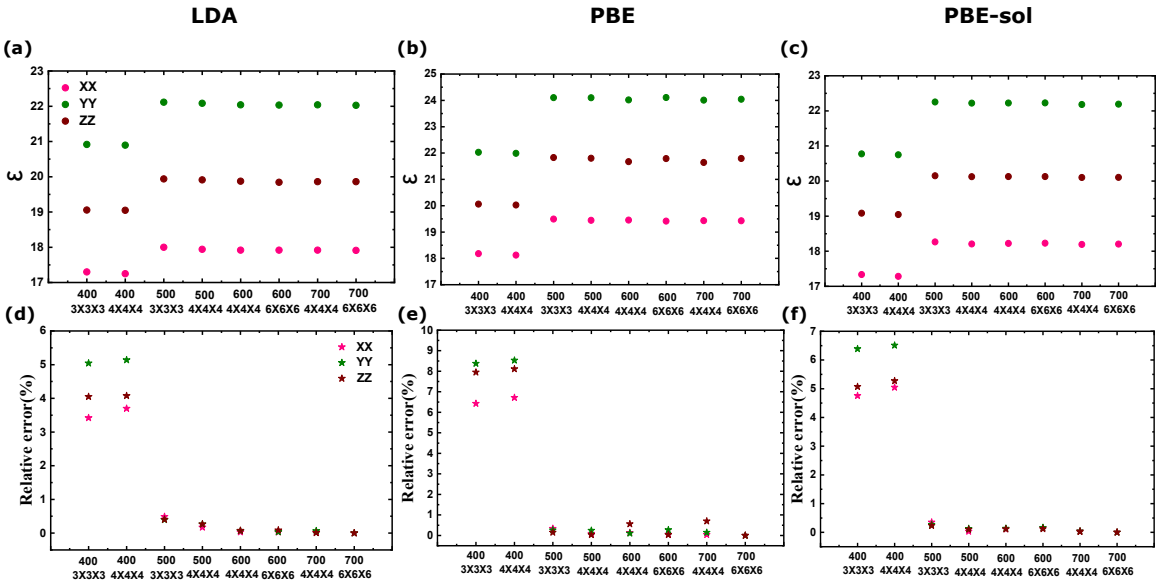

Figure 2.4: Convergence of E_{cut} and k-point grid in dielectric tensor of the ferroelectric phase of HfO_2 by using three different exchange-correlation functionals (a) LDA (b) PBE and (c) PBE-sol. In the second row, we show the relative error as a function of E_{cut} and k-point grid with respect to the highest E_{cut} and k-point grid considered. We show the results for three exchange-correlation functionals (d) LDA) (e) PBE and (f) PBE-sol.

It is worth noting here that the choice of the k-point grid depends on the size of the unit cell. If two structures have similar unit-cell parameter, the same k-point mesh can be used. However, for structures with different cell size, equivalent k-point sampling is needed. The structure with a larger unit-cell has a smaller BZ associated to it. Therefore, to sample the smaller BZ, the k-point mesh should be chosen as a subset of the k-point mesh in the larger BZ.

In order to ensure a tight convergence, we consider $E_{\text{cut}} = 600$ eV for all the calculations of HfO_2 and ZrO_2 present in this thesis. We adapt the k-point grid according to the size of the unit-cell of each polymorph. A 4×4×4 k-point grid has been used for the ferroelectric phase of HfO_2 and ZrO_2.

2.4 Additional methodological details

2.4.1 Calculation of polarization

To calculate the polarization of the material, we use the Berry's phase theory [2] as implemented in VASP. The polarization is multivalued for a bulk solid. Depending upon the choice of the unit cell of the periodic solid, we can get different values of polarization. The collection of polarization values are called polarization lattice. The polarization value increases if we consider the ferroelectric distortion of a lattice from its paraelectric phase. The polarization values along the distortion from paraelectric to the ferroelectric state forms a branch. Different branches are separated by a "quantum of polarization", which corresponds to transferring a unit charge from one unit-cell to the next. The difference in polarization within the same branch between the final polarized and initial unpolarized state is the spontaneous polarization of a ferroelectric system. The critical part for obtaining the correct value of the spontaneous polarization is to make sure one stays in the same branch.

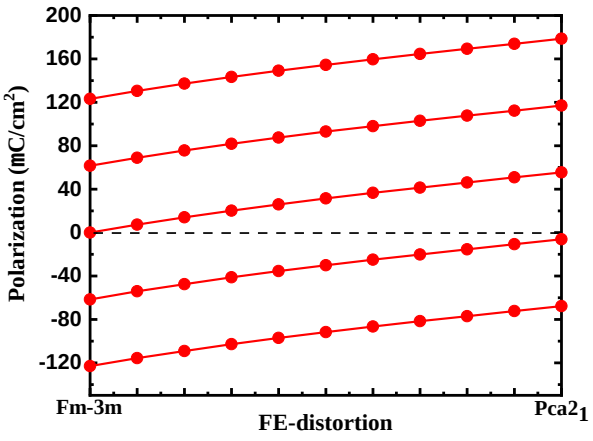

Figure 2.5: Calculated polarization as a function of the ferroelectric distortion from the high-symmetric cubic state (labeled by space group $Fm\bar{3}m$) to low-symmetric ferroelectric state (labeled by space group $Pca2_1$) of HfO_2.

To get the correct value of the spontaneous polarization of the ferroelectric phase of HfO_2, we consider the cubic phase with space group $Fm\bar{3}m$ as the high-symmetry para-

electric state and calculate the polarization for several structures along the deformation path from high-symmetry cubic phase to low-symmetry ferroelectric phase with space group $Pca2_1$. Figure 2.5 shows the values of the polarization along the deformation path. Note that the polarization value for the high-symmetry paraelectric structure, labeled with '$Fm\bar{3}m$', can be taken to be 0 μC/cm^2. Therefore it is clear from the evolution of the polarization with the distortion along that branch that the correct value of the spontaneous polarization of the ferroelectric state, labeled by '$Pca2_1$' is 55.43μC/cm^2 which is in good agreement with previously reported values[112].

Chapter 3

Preliminary first-principles study of HfO_2 and ZrO_2

In this chapter, we present some preliminary results of the structural and response properties of HfO_2 and related material ZrO_2 using the first-principles DFT. To gain confidence in producing reliable data, we compare our obtained values with the literature. This chapter also reflects our understanding of calculating the response properties of these materials using the DFPT-method.

Here we discuss the structural details of the polymorphs of HfO_2 and ZrO_2 reported experimentally and theoretically. Additionally, we show the result of a comparative study of structural and response properties in both the materials with the literature.

3.1 Polymorphs in HfO_2 and ZrO_2

HfO_2 and ZrO_2 are known as 'twin oxides' because they exhibit very similar structural and chemical properties. They are rich in polymorphism. All the reported polymorphs of these materials are discussed below.

The important nonpolar phases:

Figure 3.1 shows the important nonpolar phases of HfO_2 which have been experimentally and theoretically found in the literature. These nonpolar crystal phases are very similar in ZrO_2; hence they are not shown here. The high symmetric cubic phase with space group $Fm\bar{3}m$ (c-phase) appears at very high temperature (around 2800 K in HfO_2 [113–116] and at 2300 K in ZrO_2 [117, 118]) in both materials. All the Hf and O atoms are symmetrically equivalent in this phase. In the c-phase, the Hf atoms bond with eight nearest neighbor O atoms reflecting the compact packing in the phase. All the Hf−O bond distances are equal to 2.17 Å.

Further, with decreasing temperature, there is a phase transition from cubic to tetragonal phase (t-phase) with space group $P4_2/nmc$ around 2000 K in HfO_2 [113–116] and 1300 K in ZrO_2 [118, 119]. Compared to the high symmetric c-phase, the position of the O atoms has been displaced in the plane in the t-phase. Here, the coordination number of the Hf atoms is similar to that of the c-phase.

At ambient conditions, HfO_2 and ZrO_2 have the monoclinic baddeleyite-like structure with space group $P2_1/c$ (m-phase) as their ground state (GS)[115, 120, 121]. All the Hf

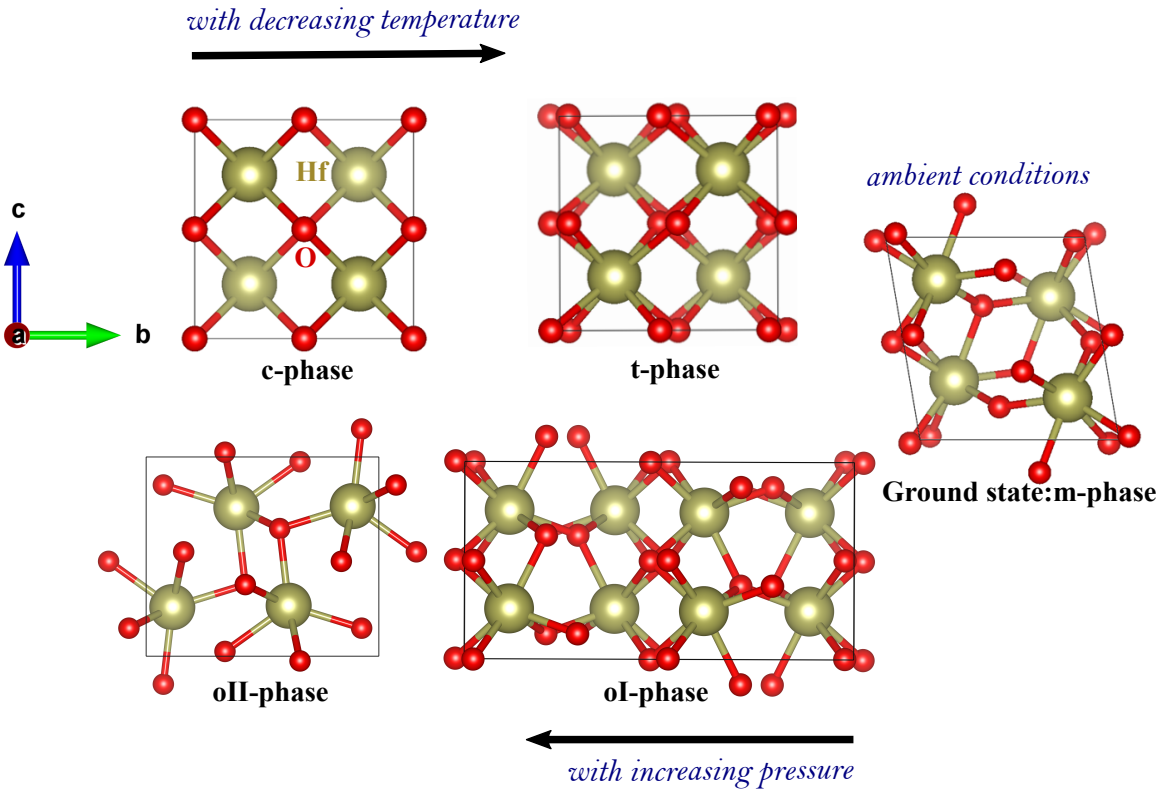

Figure 3.1: Structural view of the m-phase, t-phase, c-phase, oI-phase and oII-phase. t-phase and c-phase appear at high temperature; oI and oII phase appear in high pressure regime.

atoms in the unit cell of the m-phase are symmetrically equivalent, but there are two types of symmetrically inequivalent O atoms. The coordination of Hf atoms reduces to seven in this phase. As a result, unlike in the c-phase and t-phase, where an O atom is shared by four nearest neighbor Hf atoms, here it is shared by three.

Additionally, with increasing pressure, the m-phase sequentially transforms into the orthorhombic-*Pbca* (oI-phase) and then into the orthorhombic-*Pnma* (oII-phase) crystal phase in both materials [122, 123] as shown in figure 3.1. In comparison to the other three phases stated above, the unit-cell of the oI-phase gets doubled in the plane. The distortion in this phase due to the movements of the O atoms can be clearly understood with respect to the t-phase. Some of the O atoms are moving up in a part of the cell and moving down in another part of the cell resulting in an antipolar displacement. The coordination number of Hf has been reduced to seven from t-phase to oI-phase. In HfO_2, the oI-phase is found to be stable between 4-14.5 GPa below 1250-1400°C; whereas in ZrO_2 it can be found between 3-11 GPa [115, 116, 118, 123, 124].

Furthermore, the oII-phase appears above 14.5 GPa, and is stable up to 21 GPa and 1800°C [123] in HfO_2 and in the pressure range of 9-15 GPa in ZrO_2 [115, 118]. The coordination of Hf atoms is also seven here.

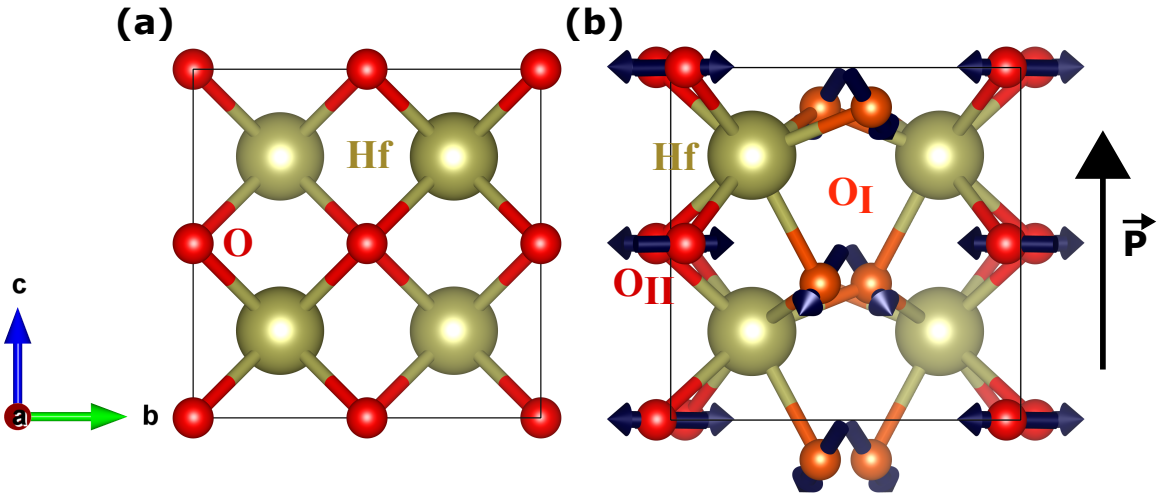

Figure 3.2: Structure of the (a) paraelectric c-phase and (b) FE-phase of HfO_2. In the c-phase, all Hf and O atoms are symmetrically equivalent. In the FE-phase all Hf atoms are symmetrically equivalent but there are two types of symmetrically inequivalent O atoms-named as O_I (in light orange) and O_{II} (in red colour). The arrows denote the movement of the O_I and O_{II} atoms from the high symmetric position in the paraelectric phase to low symmetric FE phase. The black arrow denotes the direction of the polarization.

The usual Ferroelectric phase

The origin of ferroelectricity in HfO_2 has been attributed to the formation of the orthorhombic phase with $Pca2_1$ space group (FE-phase) by Böske et al. in 2011 [19]. Figure 3.2 illustrates the ferroelectric distortion of the FE-phase from the paraelectric c-phase. In the high symmetric c-phase all the Hf atoms are equivalent among them by symmetry, and so are all the O atoms among them (4 Hf and 8 O atoms). However, in the unit-cell (4 Hf and 8 O atoms) of the FE-phase, all the Hf atoms are symmetrically equivalent, but there are two types of symmetry inequivalent O atoms, O_I and O_{II}. The polar distortion involves the downward movement of the O_I sublattice as compared to its high symmetric position in the c-phase. This movement of the O_I sublattice is shown by the arrow in figure 3.2 (b), resulting in a finite spontaneous polarization pointing upwards. The O_{II} atoms move in-plane from paraelectric to ferroelectric phase but do not contribute to the development of the polarization of the materials.

After the discovery of ferroelectricity in HfO_2, J. Muller et al. found a polarization hysteresis loop in 7.5-9.5 mm thick $Hf_{0.5}Zr_{0.5}O_2$ films integrated into TiN-based metal-insulator-metal capacitors in 2011 [125]. In another study in 2012, J. Muller et al. performed a composition and temperature-dependent ferroelectric phase transition considering the whole mixing range of HfO_2-ZrO_2 thin films [72]. The ferroelectricity in the mixed oxides has also been attributed to the same FE-phase. The FE-phase in pure ZrO_2 is confirmed by B.T.Lin et al. through high-resolution transmission electron microscopy in 2016 [126]. The same explanation holds for the ferroelectric distortion of the FE-phase in ZrO_2 as it does for HfO_2.

Theoretically predicted new polymorphs

Apart from the phases mentioned above, Huan et al. proposed a few more crystal phases of HfO_2 by performing a structural search using the minima hopping method in 2014 [38]. This structural search led to one new nonpolar phase and four new polar phases of HfO_2: nonpolar monoclinic with space group $P2_1/m$ (mI-phase) and polar monoclinic Pm (mII-phase), monoclinic Cc (mIII-phase), triclinic $P1$ (tric-phase), and orthorhombic $Pmn2_1$(oIII-phase) phases. The phonons and band structure calculations reported by the author show the dynamical stability of all the phases at zero temperature and pressure up to 30 GPa except the mI-phase, which is stable below 15 GPa .

The primitive cell of the nonpolar mI-phase contains six atoms. The coordination number of the Hf atoms is seven in this phase. Above 15 GPa, this phase collapses to the t-phase following the unstable phonon modes.

Next, the author reported that the total energy of the nonpolar mII-phase, mIII-phase, and tric-phase is unfavorable by roughly 250 meV/atom compared to the GS phase. The unit-cell of the polar mII-phase contains twelve atoms. The coordination of all the Hf atoms is not the same in this phase. Hf atoms are bonded with nine, seven, or five O atoms. The mIII-phase presents a large monoclinic angle of 123°; the coordination of Hf atoms is reduced to seven and six. In contrast, the tric-phase shows a large Hf coordination number compared to the high symmetric phase. The coordination of Hf atoms is nine and eight in this phase.

Interestingly, it has been found by Huan et al. that the newly predicted oIII-phase and FE-phase are very close in energy and compete with the other equilibrium phases. All the Hf atoms are bonded with seven O atoms in this phase. Recently, Y. Qi et al. proposed that wake-up cyclings are not required to produce a steady P−E hysteresis loop in the (111)-oriented oIII-phase[110], which is unavoidable in the usual FE-phase. This indicates that further investigation of this newly predicted ferroelectric phase could improve the performances of the HfO_2-based films in memory applications.

In 2017 S. Barabash predicted a few more crystal phases of HfO_2 [127]. In this study, six new crystal phases of HfO_2 have been found, namely: orthorhombic-$Pbcn$ (oIV-phase), tetragonal-$P4_2/mnm$ (tI-phase), tetragonal-$P4/nbm$ (tII-phase), cubic-$P\bar{4}3m$ (cI-phase), cubic-$Pa\bar{3}$ (cII-phase) and rhombohedral-$R3$ (RI-phase) phases. Among them, only the oIV-phase, tI-phase, and RI-phase are dynamically stable at 0 K and may potentially be observed under suitable experimental conditions [127].

The unit-cells of the oIV-phase and tI-phase consist of 12 atoms; the Hf atoms are coordinated with six nearest neighbor O atoms. In both phases, the O atoms involve an antipolar displacement in the unit-cell resulting in the nonpolar systems. In the unit-cell of the polar RI-phase, there are 32 atoms; the Hf atoms form three parallel layers perpendicular to the c-axis. The Hf coordination number is eight here.

S. Barabash reported that the tII-phase, cI-phase, and cII-phases are dynamically unstable at 0 K. Additional relaxation triggered by the unstable phonon modes is relatively small for tII-phase and cI-phase, indicating that it can possibly be stabilized at a finite temperature. However, the cII-phase appears very high in energy compared to the ground state of HfO_2, indicating the low probability to be found in the experiment.

In 2018, Y. Wei et al. performed a structural search by using a genetic algorithm approach for pure HfO_2 and ZrO_2 to identify their experimentally found rhombohedral phase in $Hf_{0.5}Zr_{0.5}O_2$ thin films [128]. The authors discovered two rhombohedral phases with $R3$ (RI-phase) and $R3m$ (RII-phase) symmetry and polarizations of 0.1 C/cm^2 and

41 C/cm^2, respectively in HfO_2. The Hf atoms are bonded with eight nearest neighbor O atoms in these two phases. All the Hf−O bond lengths are 2.18 Å in the RI-phase, whereas two different types of Hf−O bond distances are present in the RII-phase. Among eight nearest neighbor Hf−O bonds, four bonds are equal to 2.12 Å, and the other four are equal to 2.24 Å in RII-phase. Interestingly, Y. Wei et al. experimentally showed that the RII-phase also does not require any wake-up cycling to show the ferroelectric behavior, which may lead to potential applications in next-generation memory devices [128].

Furthermore, the RII-phase has also been found theoretically in ZrO_2 by Y. Wei et al. [128]. Recently, Silva et al. have grown the epitaxially strained rhombohedral thin films in ZrO_2. In collaboration with them, we identified the $R3m$ symmetry of the film [129] by performing the first-principles calculation. The structural details of the RII-phase in ZrO_2 are very similar to that of HfO_2 discussed above.

3.2 Relative stabilities of the polymorphs in HfO_2 and ZrO_2

The preliminary calculations of the structural properties of the polymorphs of HfO_2 and ZrO_2 are shown in this section. Here, we compare our obtained total energy values by performing the structural relaxation calculations of all the discussed polymorphs of HfO_2 and ZrO_2 with previously reported values. The primary goal of this study is to make sure that our DFT approach allows us to reproduce the data in the literature.

Table 3.1 shows the lattice parameters, unit-cell volume, and relative energies of the polymorphs compared to the GS m-phase of HfO_2. The relative energies are calculated as follows:

$$\Delta E_X = E_X - E_{GS} \tag{3.1}$$

where E_X is the energy of any particular polymorph X and E_{GS} is the ground state energy (energy of the m-phase). The values of the energy are given in per formula unit.

Here, we use LDA and GGA-PBE xc-functional to compute the lattice parameters, unit-cell volumes, and the relative energies of all the polymorphs mentioned above. Table 3.1 shows an excellent agreement with the previous literature for GGA-PBE functional in all the polymorphs of HfO_2. The present results are also in a satisfactory agreement with Ref.[109] at the LDA level. However, we find slight disagreement in the LDA results with Ref.[121], which may come from the use of different pseudo-potentials, E_{cut} and k-point grids.

Similarly, Table 3.2 presents the computed lattice parameters, unit-cell volumes, and relative energies of all the polymorphs in the case of ZrO_2. Our results for ZrO_2 are also in good agreement at the LDA level with Ref.[109]. However, we notice that the values of ΔE obtained by J.E. Jaffe et al. using LDA and GGA-PBE are low compared to the present results and the other literature [121]. The difference in pseudo-potentials, as well as the selection of E_{cut} and k-points, could be the reason for this discrepancy.

Figures 3.3 (a) and (b) show the relative energy (ΔE) obtained from the GGA-PBE calculations of all the polymorphs in HfO_2 and ZrO_2 respectively. It is also interesting to note that the common polymorphs in both materials follow the same ordering. Among all the polymorphs, m-phase [120], c-phase[132], t-phase [120, 133], oI-phase [115, 122], oII-phase [115, 122], FE-phase[19, 126], and RII-phase[128, 129] phase have been experimentally observed. We notice that the relative energies of all the experimentally observed polymorphs are below 250 meV/f.u. except for the oII-phase, which appears at very high pressure.

Phases	LDA						GGA-PBE					
	V	a	b	c	ΔE (This work)	ΔE (Literature)	V	a	b	c	ΔE (This work)	ΔE (Literature)
m	33.05	5.04	5.12	5.13	0	0	34.93	5.14	5.19	5.24	0	0
t	31.37	4.98	4.98	5.05	107	92[a], 99[b]	33.41	5.06	5.06	5.20	170	170[c]
c	30.83	4.98	4.98	4.98	147	137[a], 152[b]	32.47	5.06	5.06	5.06	249	250[c]
oI	31.71	9.87	5.16	4.98	30	24[a], 29[b]	31.41	10.04	5.24	5.08	68	65[c]
oII	28.19	5.46	3.24	6.38	173	167[a]	29.89	5.54	3.32	6.50	393	394[c]
FE	31.86	5.16	4.96	4.98	51	62[a]	33.57	5.25	5.04	5.07	91	83[c]
oIII	31.97	3.36	5.06	3.76	107		33.62	3.42	5.16	3.81	142	143[c]
oIV	35.22	5.63	5.14	4.86	201		37.21	5.78	5.25	4.91	71	71[c]
cI	32.93	5.09	5.09	5.09	526		34.62	5.17	5.17	5.17	472	472[c]
cII	31.17	4.99	4.99	4.99	118		32.98	5.09	5.09	5.09	198	199[c]
tric	28.65	3.17	5.56	6.68	764		30.24	3.23	5.66	6.81	966	>800[c]
tI	36.25	5.73	5.73	4.78	258		38.09	5.83	5.83	4.87	97	97[c]
tII	31.21	5.00	4.98	5.00	116		33.05	5.11	5.07	5.11	193	193[c]
mI	32.07	5.14	3.47	3.62	136		35.06	5.43	3.46	3.86	79	80[c]
mII	30.22	5.43	3.24	6.92	705		32.54	5.49	3.35	7.14	802	>800[c]
mIII	32.00	7.10	7.16	6.03	226		33.92	7.26	7.30	6.09	254	∼250[c]
RI	31.94	7.04	7.04	8.93	182		33.76	7.17	7.17	9.09	218	216[c], 221[d]
RII	31.18	7.07	7.07	8.65	206		32.95	7.20	7.20	8.81	200[c]	209[d]

Table 3.1: Computed lattice parameters in Å, unit-cell volume in Å^3/f.u., and energy difference ΔE (This work) in meV/f.u. with respect to the GS m-phase of the HfO_2 polymorphs. ΔE (Literature) refers the same energy difference available in the literature.
[a] Ref.[109], [b] Ref.[121], [c] Ref.[127], and [d] Ref.[110].

Phases	LDA						GGA-PBE					
	V	a	b	c	ΔE (This work)	ΔE (Literature)	V	a	b	c	ΔE (This work)	ΔE (Literature)
m	34.19	5.09	5.18	5.25	0	0	36.05	5.19	5.25	5.37	0	0
t	32.41	5.03	5.03	5.11	51	49[a], 38[b]	34.61	5.12	5.12	5.27	110	109[b]
c	31.84	5.03	5.03	5.03	92	96[a], 67[b]	32.47	5.06	5.06	5.06	249	171[b]
oI	32.77	9.98	5.22	5.03	27	26[a], 14[b]	34.49	10.15	5.30	5.13	67	49[b]
oII	29.19	5.52	3.29	6.43	123		30.92	5.60	3.37	6.54	344	262[b]
FE	32.95	5.22	5.02	5.03	40	37[a], 39.7[c]	34.79	5.32	5.10	5.13	72	72[c]
oIII	33.04	3.43	5.13	3.75	80	80.2[d]	34.80	3.50	5.25	3.79	120	-
RII	32.21	7.14	7.14	8.75	62		34.04	7.27	7.27	8.91	154	-

Table 3.2: Computed lattice parameters in Å, unit-cell volume in Å^3/f.u., and energy difference ΔE (This work) in meV/f.u. with respect to the GS m-phase of the ZrO_2 polymorphs. ΔE (Literature) refers the same energy difference available in the literature.
[a] Ref.[109], [b] Ref.[121], [c] Ref.[130], and [d] Ref.[131].

Therefore, it seems safe to assume that beyond this threshold, the polymorphs are not experimentally relevant. For this reason, we do not consider them for this thesis work.

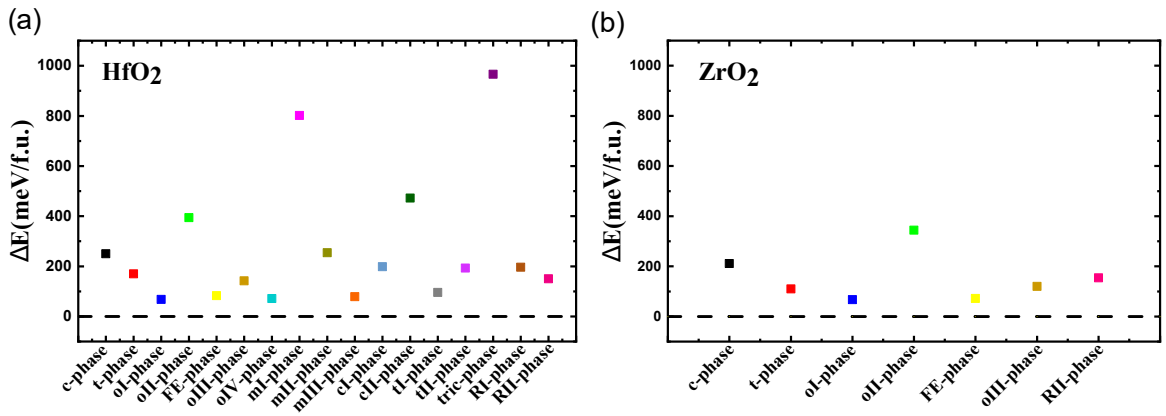

Figure 3.3: Relative energy of the reported polymorphs of (a) HfO_2 and (b) ZrO_2 using GGA-PBE xc-functional. The relative energy has been calculated by taking the GS m-phase as a reference structure. The dashed line at 0 in the y axis denotes the energy of the GS m-phase.

3.3 Dielectric Tensor

In this section, we report the calculated dielectric tensor (ϵ) of the m-phase, t-phase, and c-phase of HfO_2 and ZrO_2 to get familiar with the DFPT-method as implemented in VASP code. Here, we use LDA xc-functional to compare the present values with the literature

Phase	HfO_2		ZrO_2	
	This work	Previous work [134]	Present	Previous [135]
m	$\begin{bmatrix} 13.9 & 0.0 & 0.8 \\ 0.0 & 12.1 & 0.0 \\ 0.8 & 0.0 & 9.3 \end{bmatrix}$	$\begin{bmatrix} 13.1 & 0.0 & 1.8 \\ 0.0 & 10.8 & 0.0 \\ 1.8 & 0.0 & 7.5 \end{bmatrix}$	$\begin{bmatrix} 16.3 & 0.0 & 0.9 \\ 0.0 & 14.5 & 0.0 \\ 0.9 & 0.0 & 10.9 \end{bmatrix}$	$\begin{bmatrix} 16.7 & 0.0 & 0.9 \\ 0.0 & 15.6 & 0.0 \\ 0.9 & 0.0 & 11.7 \end{bmatrix}$
t	$\begin{bmatrix} 40.9 & 0.0 & 0.0 \\ 0.0 & 40.9 & 0.0 \\ 0.0 & 0.0 & 13.7 \end{bmatrix}$	$\begin{bmatrix} 92.3 & 0.0 & 0.0 \\ 0.0 & 92.3 & 0.0 \\ 0.0 & 0.0 & 10.7 \end{bmatrix}$	$\begin{bmatrix} 42.1 & 0.0 & 0.0 \\ 0.0 & 42.1 & 0.0 \\ 0.0 & 0.0 & 14.9 \end{bmatrix}$	$\begin{bmatrix} 41.6 & 0.0 & 0.0 \\ 0.0 & 41.6 & 0.0 \\ 0.0 & 0.0 & 14.9 \end{bmatrix}$
c	$\begin{bmatrix} 24.5 & 0.0 & 0.0 \\ 0.0 & 24.5 & 0.0 \\ 0.0 & 0.0 & 24.5 \end{bmatrix}$	$\begin{bmatrix} 23.9 & 0.0 & 0.0 \\ 0.0 & 23.9 & 0.0 \\ 0.0 & 0.0 & 23.9 \end{bmatrix}$	$\begin{bmatrix} 30.2 & 0.0 & 0.0 \\ 0.0 & 30.2 & 0.0 \\ 0.0 & 0.0 & 30.2 \end{bmatrix}$	$\begin{bmatrix} 31.8 & 0.0 & 0.0 \\ 0.0 & 31.8 & 0.0 \\ 0.0 & 0.0 & 31.8 \end{bmatrix}$

Table 3.3: Computed lattice part of the dielectric tensor (ϵ^{latt}) of m-phase, t-phase and c-phase of HfO_2 and ZrO_2. All the values are calculated using LDA.

since there is no published data (full tensor) available for the PBE and PBE-sol functionals.

Table 3.3 represents the computed lattice part of the ϵ tensor (ϵ^{latt}) for the m-phase, t-phase, and c-phase. We find that the values of ϵ^{latt} change dramatically with the crystal phases in both HfO_2 and ZrO_2. Additionally, ϵ^{latt} is always higher in ZrO_2 irrespective of the crystal phases.

Next, we observe that our results are in reasonably good agreement with the reported values in the literature [135, 136] except for the t-phase of HfO_2. The $\epsilon^{latt}_{XX} = \epsilon^{latt}_{YY}$ component of the dielectric tensor of the t-phase in the Ref. [136] is more than twice the present value. However, our result matches reasonably well in the case of ZrO_2. We also find that the value of the ϵ^{latt}_{XX} of the t-phase of HfO_2 reported by D.Fischer et al. is 25-40 [137] and by G.-M.

Rignanese et al. is 32.8 [138], which are reasonably close to our value. We also check that the experimental value of the dielectric constant for a polycrystalline HfO_2 sample is 22-25, and for ZrO_2 is 17-18 [139]. Therefore, the obtained values in the present study seem to be in reasonably good agreement with other reported values[137–139]. Nevertheless, we have been intrigued to know the reason behind the substantial discrepancy in ϵ^{latt}_{XX} component in t-phase of HfO_2 with Ref. [136].

To understand the reason behind the disagreement in the ϵ^{latt}_{XX} component in the t-phase with Ref. [136], we pay attention to the reported structural parameters (lattice-parameters, unit-cell volume) of the systems. We observe that the given unit-cell volume in Ref. [136] is around 2.5% larger than the present value. This difference in the unit-cell volume between the current study and then that of Ref. [136] indicates a difference in strain between the two systems.

Therefore, we decide to study how the three components of the ϵ tensor vary with the hydrostatic strain in the t-phase of HfO_2. We consider hydrostatic strain to the volume of

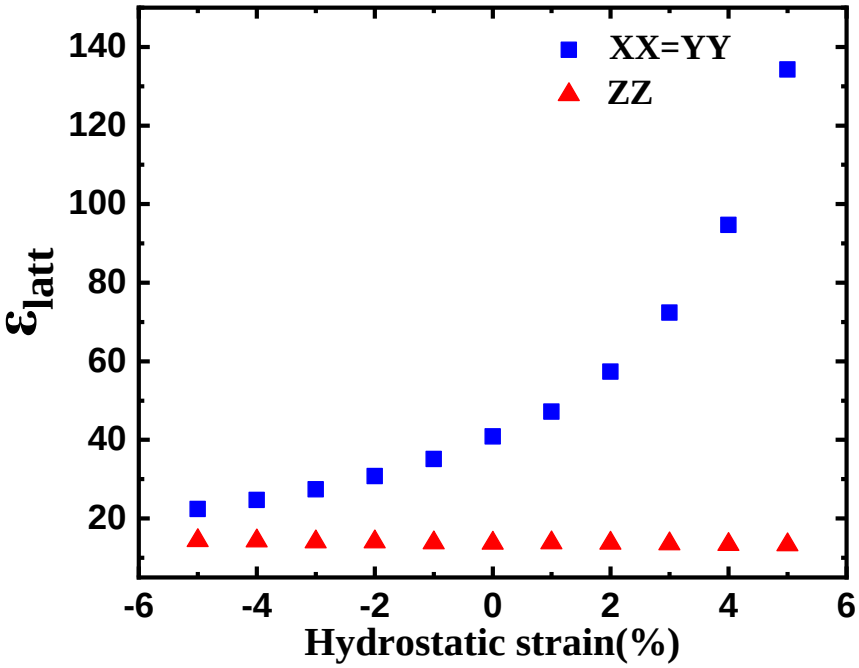

Figure 3.4: Computed lattice part of the dielectric tensor of (ϵ^{latt}) the t-phase as a function of hydrostatic strain.

the tetragonal unit-cell up to ±5% with the step size of 1%, and relax the atomic positions within the strained unit-cell. The dielectric tensor at each strain value is then computed.

Figure 3.4 shows the variation of the dielectric tensor as a function of strain. We find that the ϵ^{latt}_{ZZ} component of the dielectric tensor is nearly constant throughout the strain range, but the ϵ^{latt}_{XX} component varies significantly with the strain values. ϵ^{latt}_{XX} increases rapidly with increasing the hydrostatic strain indicating the occurrence of a soft mode along this direction in the t-phase. This indicates that a polar instability develops in-plane

in this phase. Note that the usual orthorhombic ferroelectric phase (FE-phase) develops a polarization perpendicular to the tetragonal axis, suggesting the potential connection to the t-phase−FE-phase transition.

We find that our calculated value of the ϵ_{XX}^{latt} is around 70 at 2.5% strain, which is relatively close to the reported values in the Ref. [136]. Although we could not get the actual value of ϵ_{XX}^{latt} reported in Ref.[136], the application of strain seems to partly explain the disagreement with the present study. We think that the use of the different pseudopotential, different E_{cut} and k-point grid or distinct methods may also make a difference in the result.

3.4 Summary and Conclusions

In this chapter, we show the preliminary results of the structural and response properties of HfO_2 and ZrO_2. We discuss all the polymorphs of HfO_2 and ZrO_2 that have been experimentally and theoretically reported. Additionally, we describe the polar distortion of the FE-phase, resulting in a spontaneous polarization in both materials. We calculate the total energy of each polymorph using LDA and GGA-PBE and compare them with the previously reported values. Overall, we find that our results are in good agreement with the literature. We get the expected total energy ordering of the crystal phases as reported in the literature.

To learn the DFPT-method as implemented in the VASP code, we reproduce the dielectric tensor of a few phases of the materials present in the literature. We believe that this study indeed helps us to get confidence in producing reliable data.

In the rest of this thesis, we only work with HfO_2. For our purposes, we ignore the high energy lying polymorphs of HfO_2. In the following chapters, we work with the GS m-phase, FE-phase, and t-phase of HfO_2.

Chapter 4

Impact of the dopant ordering in stability of ferroelectric HfO_2

In this chapter, we will discuss the stability issue of the usual ferroelectric phase (FE-phase) of HfO_2. In addition, based on a theoretical prediction, we will discuss a strategy to stabilize the FE-phase. Finally, we will provide some insights into practical implications.

4.1 Background & Motivation

In the past decade, extensive research has been carried out to understand the origin of the ferroelectricity in HfO_2. The ferroelectric behavior in this material is caused by the formation of the metastable noncentrosymmetric orthorhombic phase (FE-phase). Several strategies have been tried to stabilize the FE-phase.

Surprisingly, unlike perovskites, the ferroelectricity in HfO_2 becomes robust with decreasing the film thickness or the size of the grains [140]. This suggests that surface energy may play a vital role in stabilizing the polar phase. R.Materlik et al. calculated the Gibbs/Helmholtz free energy with varying stress and film strain to explain the existence of the ferroelectric phase in nanoscale thin films. The authors found that the energies are unlikely to become minimal in $Hf_{0.5}Zr_{0.5}O_2$ thin films under technologically relevant conditions [109]. They also predicted a surface energy model in which the grain size of undoped HfO_2 and epitaxial $Hf_{0.5}Zr_{0.5}O_2$ must be around 4 nm and less than 5 nm, respectively. However, the experimental observations in HfO_2-ZrO_2 solid-solutions thin films by M.H.Park et al contradict the theoretical surface energy model proposed by Materlik et al [66].

Moreover, the role of the local strain [67, 68], oxygen vacancies [69, 70], grain size [66] in the stability of FE-phase have also been discussed in the literature. Y. Zhou et al. have shown that the bulk oxygen vacancies promote the ferroelectric phase transition by reducing the energy difference between m-phase and FE-phase[69]. E.D.Gimley et al. demonstrated the complex structure near the phase boundaries, suggesting a probable continuous transition between m-phase and FE-phase in the region of the boundary walls [141].

Interestingly, it is experimentally known that the chemical doping with Si [19], Al [73], Y [142], Zr [72] and La [57], Mg [143], Ca [143] facilitate the formation of the FE-phase using various deposition techniques including metal-organic-chemical vapor deposition (MOCVD), sputtering, chemical solution deposition (CSD), pulsed laser deposition (PLD) and atomic layer deposition (ALD). This suggests that the $Hf_{1-x}A_xO_2$ compound might undergo a paraelectric to ferroelectric phase transition for a suitable dopant A as

x increases, which would be very similar to the morphotropic phase boundary that many perovskites exhibit [144]. For example: $Sr_{1-x}Ba_xTiO_3$ shows a paraelectric to ferroelectric phase transition with increasing Ba content. Among all the dopants, the HfO_2-ZrO_2 solid solutions are most intensively studied, where the ferroelectricity exists in a wide composition range. In contrast, the Y-doped HfO_2 system shows a very narrow compositional window, and high-temperature thermal treatment is needed to obtain the ferroelectricity [143]. Such morphotropic tansitions are usually revealed by first-principles calculations. However, the existing DFT studies predicted that doping alone is not enough to make the FE-phase the most stable phase [74–78, 145].

In this study, using first-principles methods, we decided to reexamine this fact by considering the chemical dopants as an external tuning factor. Surprisingly, in our preliminary simulations, we observe that some dopants have a strong preference to adopt specific arrangements. However, with the exception of Ref.[77] and Ref.[75], most of the DFT studies assumed that the dopant located randomly inside the HfO_2 lattice, which we here prove to be inappropriate. Thus, what are the preferred spatial arrangements of the dopants inside the HfO_2 lattice? Does that affect the stabilization of the FE-phase of HfO_2?

4.2 Computational Approach

For the sake of simplicity, we consider two tetravalent dopants Si and Zr, which are extensively studied experimentally and theoretically. Due to the same valency of the dopants as of the Hf atoms, we can replace the Hf atom with the dopant without inducing any charge states or oxygen vacancies inside the lattice.

In the following, we focus on the usual ferroelectric phase (FE-phase), the GS m-phase, and another nonpolar t-phase. This t-phase has been discussed in the literature as a bridge state, which leads to the stabilization of the FE-phase [38, 146]. We will discuss the relevance of this t-phase in the following section .

In this study, we work with a 48-atom cell with $a' = \sqrt{2}a$, $b' = \sqrt{2}b$, $c' = 2c$, where a', b', and c' are the lattice vectors of the simulation cell, and a, b, and c are lattice vectors of the primitive unit-cell of HfO_2 lattice. Our simulation cell contains 16 $Hf_{1-x}A_xO_2$ formula units. This cell is compatible with a compositional step Δx=0.0625 (6.25%). We study the doping concentration ranging from Δx=0.0625 (6.25%) to Δx=0.5 (50%).

In the unit-cell, wherever we have more than one dopant, we consider a representative number of arrangements of the dopants. Figure 4.1 shows the different spatial arrangements of the dopants at different concentrations, which includes the cases: dopants forming layers in different crystallographic planes, forming quasispherical aggregates, intercalating between Hf atoms, etc. At x=6.25%, there is only one case to consider, which is an isolated dopant. We study 4 different arrangements for 12.5%, 12 for 25%, 17 for 31.25%, 16 for 37.5%, 12 for 43.75%, and 12 for 50% doping concentration for the three polymorphs.

We realize that the size of the cell is not compatible with considering different dopant arrangements at low doping concentration (at x=6.25%). Thus we also consider an elongated supercell of 192-atoms with $a' = \sqrt{2}a$, $b' = \sqrt{2}b$, $c' = 8c$, where a', b', and c' are the lattice vectors of the simulation cell, and a, b, and c are lattice vectors of the primitive unit-cell of HfO_2 lattice. At this concentration, we only consider some particular dopant arrangements, which are previously identified as the most energetically favorable in high doping concentration levels. Figure 4.2 depicts the special dopant arrangements considered in the 192-atoms supercell. Figures 4.2(a) and (b) represent the cases where the dopants

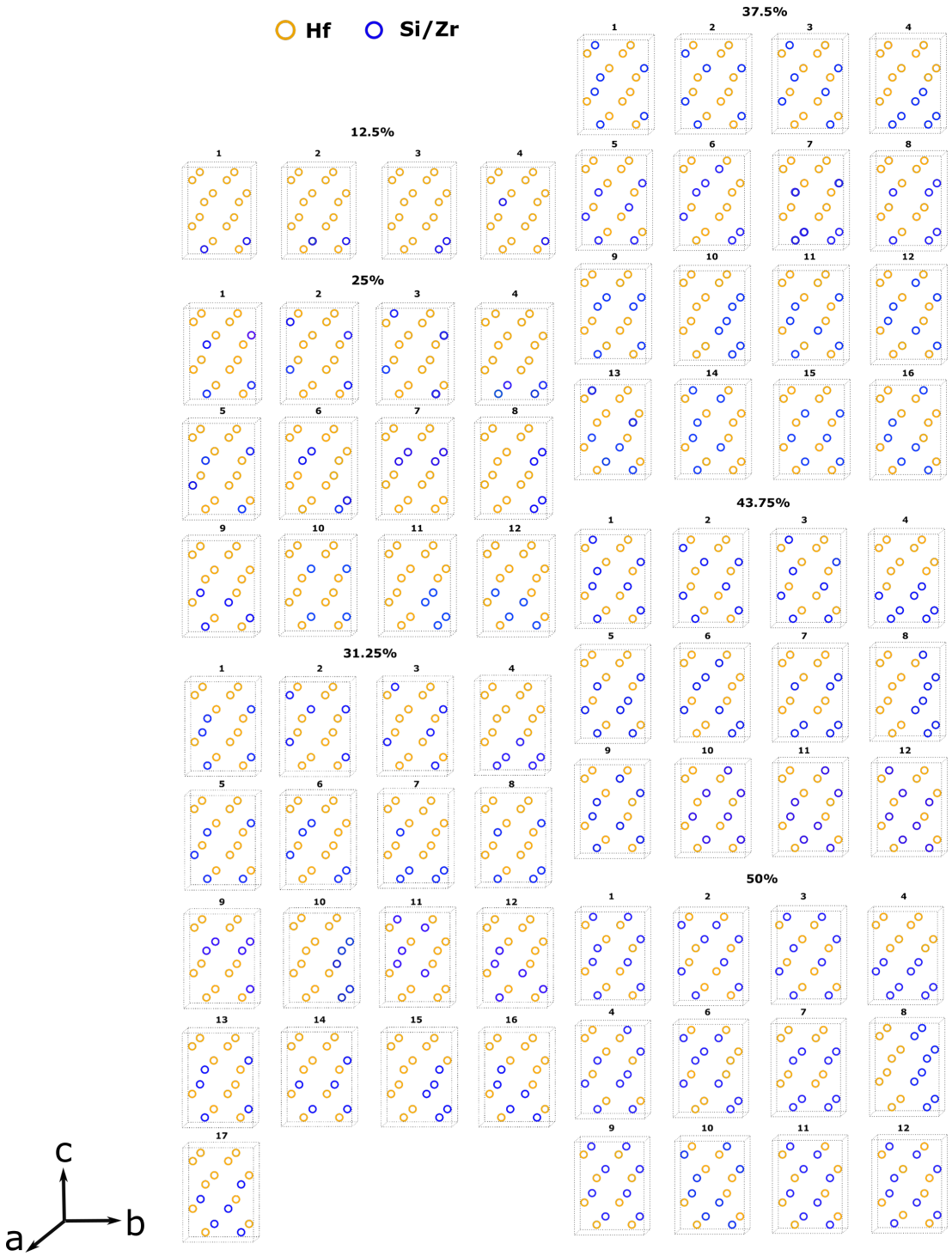

Figure 4.1: Dopant arrangements considered in our 48-atom cell at each doping concentration. We sketch only the cations (Hf, Si, Zr) for the clarity.

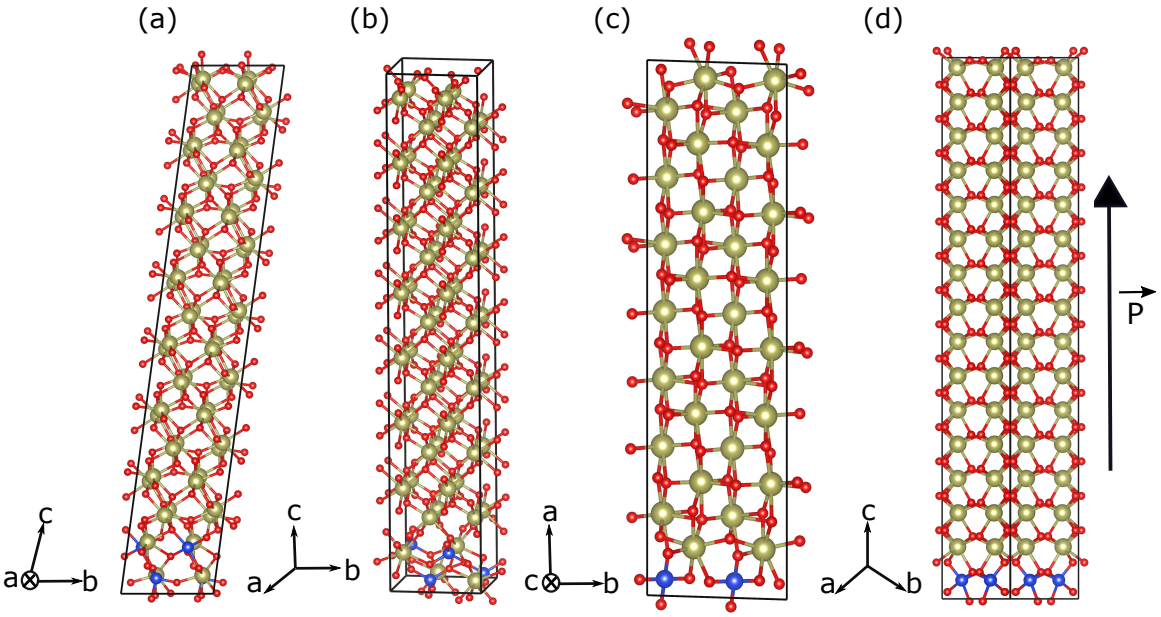

Figure 4.2: Schematic of 192-atom supercell of the considered cases at low doping concentration. (a) m-phase with a region of intercalated Hf atoms and dopants, (b) t-phase with a region of intercalated Hf atoms and dopants, (c) t-phase with a layer of dopants perpendicular to the a-axis, and (d) FE-phase with a dopant layer perpendicular to c-axis.

are intercalated between Hf atoms in the m-phase and t-phase, respectively, whereas the Figures 4.2(c) and (d) present the configurations where dopant layers are oriented in a particular crystallographic direction for t-phase and FE-phase, respectively.

4.3 Results

We performed a structural relaxation and calculated the total energy of all the considered configurations at all concentrations for all the polymorphs. Then we calculate the formation energies of each compound following the equation below:

$$E_{\text{for}}(x) = E(x) - (1-x)E_{\text{HfO}_2} - xE_{\text{AO}_2} \tag{4.1}$$

where $E(x)$ is the energy of the $\text{Hf}_{1-x}\text{A}_x\text{O}_2$ compound for a given configuration, E_{HfO_2} is the energy of HfO_2 in it's ground state, and E_{AO_2} is the ground state energy of pure AO_2. For HfO_2 and ZrO_2, we use the m-phase [127, 147] and for SiO_2, we use the $I\bar{4}2d$ structure reported in Ref.[148] as a ground state.

Si-doped & Zr-doped HfO_2: We discuss our obtained results gradually following the discoveries based on our simulations. Initially, we focused on the GS m-phase and FE-phase using the 48-atom cell. Figures 4.3 (a) and (b) show the formation energy of all the considered configurations of $\text{Hf}_{1-x}\text{Si}_x\text{O}_2$ and $\text{Hf}_{1-x}\text{Zr}_x\text{O}_2$ systems, respectively. The results using the 48-atom cell are shown by the open red symbol for the m-phase and the open blue symbol for FE-phase. In Figure 4.3, we use different symbols for different dopant arrangements: the triangles represent the configurations when dopants form a full layer, the square represents the Hf/dopant intercalation, and the circle denotes the other cases.

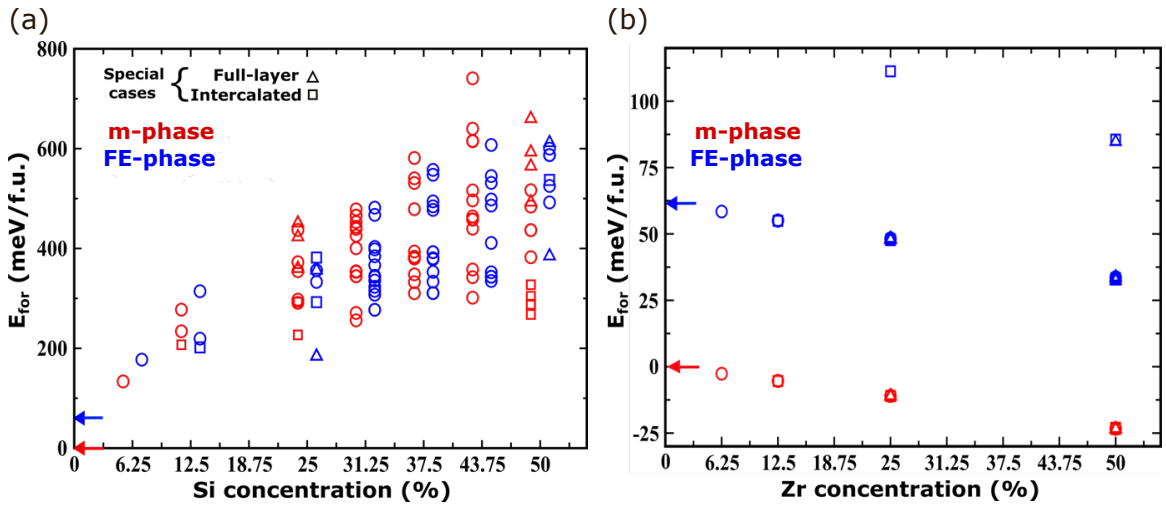

Figure 4.3: Formation energies of different polymorphs in various dopant configurations are shown for (a) Si doped and (b) Zr doped systems. The different polymorphs are marked in different colours. Triangles are used to denote the structures forming a full layer, squares correspond to the perfect dopant/Hf intercalation, and the circles are used to represent other cases. The colored arrows placed at x=0 represent the energies of m-phase (red), FE-phase (blue) as computed for the pure HfO_2 considering the m-phase as the zero of energy. In (a), the values for the m-phase and FE-phase are slightly shifted horizontally for better visibilty at each doping configuration.

At first sight, we notice a marked difference between the behavior of the two systems. The formation energy difference between the least stable and the most stable configurations are huge (up to 400 meV/formula unit (f.u.)) in the case of $Hf_{1-x}Si_xO_2$. Contrastingly, the $Hf_{1-x}Zr_xO_2$ shows much weaker tendency towards ordering. The difference between the most stable and least stable configurations is a maximum of ∼62 meV/f.u. for the Zr-doped system.

Next, we also observe that the formation energy for Si doping is always positive, implying that $Hf_{1-x}Si_xO_2$ mixtures are metastable. This means that at equilibrium, the system will minimize its free energy by phase separation. Contrastingly, the formation energy of the m-phase of $Hf_{1-x}Zr_xO_2$ is always negative throughout the doping concentration range, indicating the thermodynamic drive towards forming the HfO_2-ZrO_2 solid solutions.

Interestingly, it is worth noting that the structures of m-phase and FE-phase occupy the same energy level and compete among themselves in the case of Si doping. On the other hand, for Zr doping, all the configurations of the m-phase win over the FE-phase in the whole concentration range. From this inspection we conclude that the Si-doped system is more interesting than the Zr-doped system.

Si-doped HfO_2: Let us discuss the results of the $Hf_{1-x}Si_xO_2$ system progressively. Figure 4.4 presents the results for the Si-doped system. At this point, we realized that some of the structural relaxations yield a different solution. By inspecting the structures carefully, we find that the new solution belongs to the t-phase of HfO_2 represented by the open green symbols in Figure 4.4. It is noticeable in Figure 4.4 that the t-phase becomes very stable, even showing the lowest formation energy for a specific dopant configuration at 50% Si concentration. Having discovered that the t-phase can be very stable upon Si

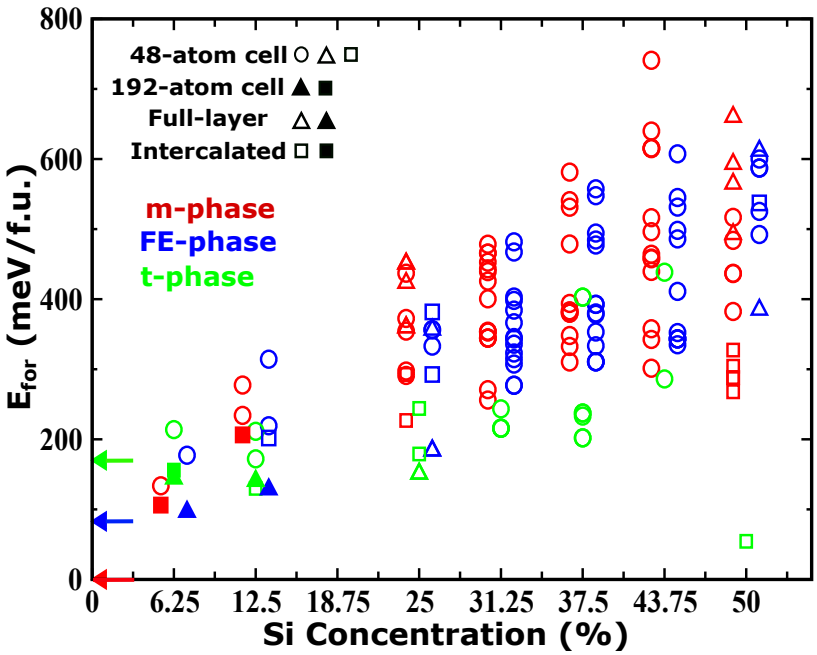

Figure 4.4: Formation energies of Si-doped HfO_2 as a function of Si concentration. The different polymorphs are marked in different colours.Triangles are used to denote the structures forming a full layer, squares correspond to the perfect dopant/Hf intercalation, and the circles are used to represent other cases, as mentioned in Figure 4.3. All the filled symbols represent the calculations with a 192-atom supercell. The colored arrows placed at x=0 represent the energies of m-phase (red), FE-phase (blue), and t-phase (green) as computed for the pure HfO_2 considering the m-phase as the zero of energy. The values for the m-phase and FE-phase are slightly shifted horizontally for better visibilty at each doping configuration.

doping, we consider this phase and run simulations for all the dopant arrangements previously considered for the m-phase and FE-phase. Our results indicate that the t-phase starts to dominate with increasing the Si concentrations. In 2018, M.Falkowski et al. have also reported a similar stabilization of the t-phase[77].

Most interestingly, we find that the FE-phase dominates over the GS m-phase for Si concentrations of 12.5-25% in some particular dopant arrangements. Figures 4.5 (a) and (b) represent the structures becoming more stable in the FE-phase, and in the t-phase. In Figure 4.5 (a), the dopants form a layer perpendicular to the c-axis, and this particular dopant arrangement yields the lowest energy solution at 25% doping concentrations for the FE-phase. On the other hand, in Figure 4.5(b), the Si atoms are intercalated between the Hf atoms, and is typically the case for the stable t-phase at 50%. Further, a group of lowest energy structures of m-phase is also characterized by the intercalation of Si and Hf atoms like that of figure 4.5 (b). In addition, some of the stable solutions of the t-phase form a dopant layer perpendicular to the a-axis. Yet, the intercalation or layering alone does not assure the low formation energy of a given structure as the data shows in Figure 4.4.

Chemical environment of the atoms: We have carefully studied the chemical environment of the atoms inside the lattice to understand the traits that result in the most stable

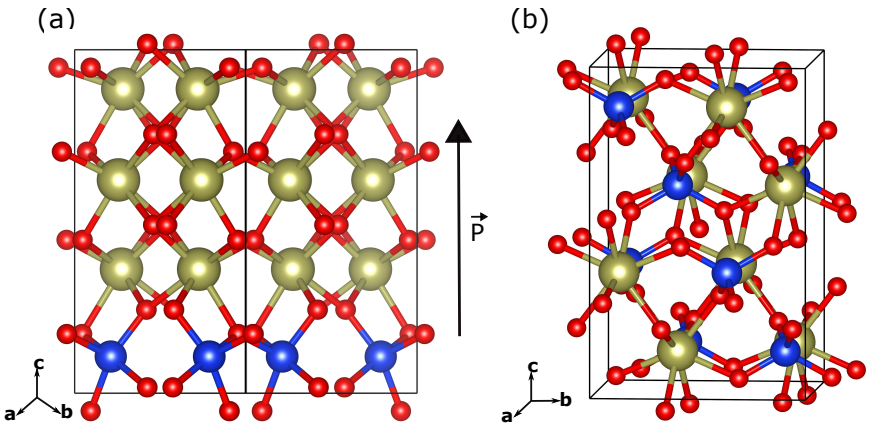

Figure 4.5: Representative low energy structures in 48-atom cell of the $Hf_{1-x}Si_xO_2$ system. (a) the most stable configuration obtained for the FE-phase at 25% Si concentration, (b) most stable atomic arrangement obtained for the t-phase at 50% Si concentration.

and least stable arrangements.

	Covalent radii		Ionic radii
Hf	1.87	Hf^{4+}	0.7
Si	1.11	Si^{4+}	0.4

Table 4.1: Covalent and ionic radii (of coordination IV) of Hf and Si in Å. The values of the covalent radii and ionic radii have been taken from Ref.[149] and Ref.[150] respectively.

Table 4.1 presents the values of the covalent radii of Hf and Si, and ionic radii of Hf^{4+} and Si^{4+}. Note that the Hf−O coordination number is seven in the m-phase, the FE-phase, and eight in the t-phase. But the size difference of the atoms in Table 4.1 implies that, as compared to Hf, Si dopants will choose relatively low oxygen coordination numbers. Figure 4.6 displays the chemical environment of Si and O atoms in the low and high lying energy configurations. Indeed, in Figures 4.6 (a),(b) and (c) we find lower Si−O coordination in the $Hf_{1-x}Si_xO_2$ lattice.

We observe that some of the most stable structures exhibit SiO_4 groups, which look nearly like tetrahedra (see in Figure 4.6(a)). All the Si−O bond lengths are equal here. This typical Si−O coordination has been found in the case of the lowest energy t-phase. Another important Si−O coordination involves SiO_5 groups forming square-based pyramids (see Figure 4.6(b)). The SiO_5 groups can be found in all the low-lying structures of the m-phase and FE-phase. Next, we also find the SiO_6 groups forming quasioctahedral as shown in Figure 4.6(c). This type of Si coordination has been found in the high-lying configurations of m-phase and FE-phase.

Additionally, we pay attention to the chemical environment of O atoms in all the structures. We see that the O atom is bound to one Si and two Hf atoms, as shown in Figure 4.1(d) in all the low-lying structures, whereas the high-lying structures show the O atoms are coordinated with two Si and one Hf as those in Figure 4.6(e). We also notice complex O coordination like that of Figure 4.6(f) displayed by the even less stable configurations. Therefore, our findings imply that the lowest-energy states are those in which the chemical-bond topology permits the dopants to form the most stable bonding complexes,

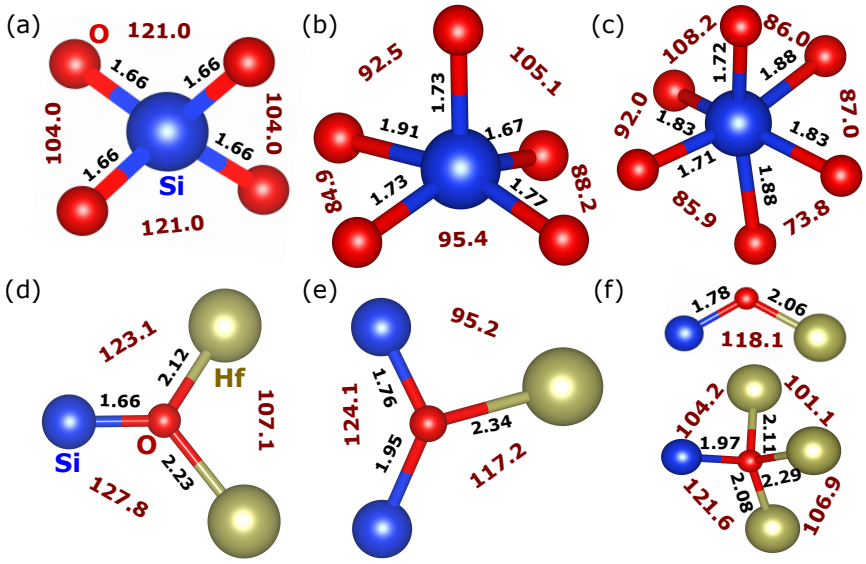

Figure 4.6: Chemical environments of (a-c) Si and (d-f) O atoms in relaxed structures. The bond lengths and the bond angles are indicated in Å and in degrees, respectively.

such as those shown in Figures 4.6 (a), (b), and (d).

Effect of dopant arrangements at low concentration: Having found that the ordering of the dopant affects the stability of the phase we were curious to see the effect in the limit of low doping concentration. We realize that our 48-atom cell is not compatible with considering the different orderings of the dopants at 6.25% concentration. Therefore we use the supercell of 192-atom as discussed in the previous section (see Figure 4.2). At this level, we consider only the previously identified most energetically favorable doping arrangements (i.e., the intercalation between the Hf/Si atoms and a dopant layer perpendicular to the different crystallographic axis.). The formation energies of these newly considered structures are shown by the filled symbol in Figure 4.4.

Excitingly, the results with the supercell indicate that the FE-phase with a full Si layer perpendicular to the c-axis dominates over the m-phase and t-phase for 6.25% doping concentration, which means the FE-phase can be thermodynamically stable GS of HfO_2 at low Si concentration. With increasing Si concentration, at 12.5%, the layered FE-phase and intercalated t-phase show almost the same energy, and the t-phase starts to dominate for the further increment of Si concentrations.

It is worth noting here that the difference of formation energies between the m-phase and FE-phase for the isolated dopant at 6.25% doping concentration, presented by the open circle in Figure 4.4 reflects the energy difference of the same phases in the undoped system (denoted by the colored arrows at x=0 in Figure 4.4). Nevertheless, the energy has been reduced once the dopants are allowed to accommodate themselves in their preferred manner inside the lattice in the case of FE-phase and t-phase. In contrast, this energy reduction is comparatively less for the m-phase. Due to this different behavior, the FE-phase dominates over the m-phase.

Finally, it seems that the main findings of this study are related to the size and chemical environment of the dopants and the way of accommodating them inside the lattice of FE-phase and t-phase. Based on such prediction, we ran simulations for another small

tetravalent dopant, Ge. Figure 4.7 presents the preliminary results for the Ge-doped system. Indeed, we find that Ge too shows a strong tendency towards ordering. At lower concentrations, the m-phase dominates over the FE-phase. However, it stabilizes the FE-phase with a full Ge layer perpendicular to the c-axis similar to that of Figure 4.2(d) at 25% doping concentration.

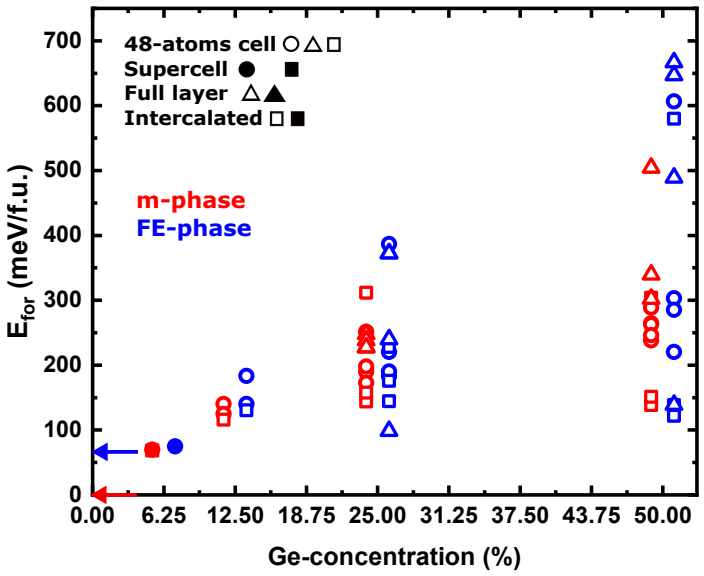

Figure 4.7: Formation energies of Ge-doped HfO_2 as a function of Ge concentration. The formation energies are calculated considering the tetragonal structure with space group $P4_2/nmc$ as a ground state of GeO_2. The different polymorphs are marked in different colours. Triangles are used to denote the structures forming a full layer, squares correspond to the perfect dopant/Hf intercalation, and the circles are used to represent other cases, as mentioned in Figure 4.3. All the filled symbols represent the calculations with the 192-atom supercell. The values for the m-phase and FE-phase are slightly shifted horizontally for better visibilty at each doping configuration.

In contrast, we see that the Zr has much weaker tendency towards ordering, and the m-phase prevails throughout the doping concentration range. The other big tetravalent dopants Ti, Sn, and Pb also follow the same trend according to our preliminary calculations. Therefore, it is clear that the effect of dopant ordering in the stabilization of FE-phase of HfO_2 does not work for the big dopants like Zr.

System	Dopant Ordering	Si-concentration	Polarization
HfO_2		0	55
$Hf_{0.9375}Si_{0.0625}O_2$	layered	6.25	53
$Hf_{0.75}Si_{0.25}O_2$	layered	25	44

Table 4.2: Calculated polariztaion of $Hf_{1-x}Si_xO_2$ at different concentrations including the pure HfO_2 using the Berry's phase theory as discussed in Chapter 2. The values of the polarization are in $\mu C/cm^2$. The polarization is calculated for the doped systems where dopants form a layer perpendicular to the direction of the polarization.

Polarization of the Si-doped sytem At this state, one may be curious about the value of the polarization of the doped systems compared to the pure FE-phase of HfO_2. Table 4.2 presents the calculated polarization for pure HfO_2, which is in agreement with the literature [38, 61, 147], and for the most stable structures at 6.25% and 25% Si concentrations. The values indicate that the Si dopants do not significantly harm the polarization of the materials.

4.4 Discussion, practical implications

It is worth discussing the practical implications of our theoretical predictions in this section. Our findings suggest that one can grow a sample in the FE-phase by depositing a thin layer

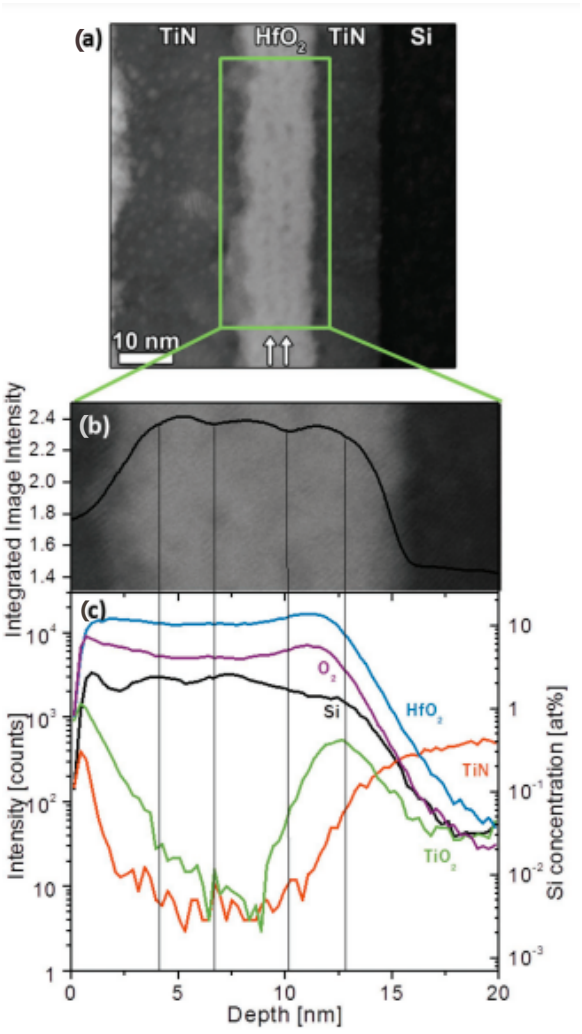

Figure 4.8: This image is taken from Ref. [56]. a) STEM image of a 10 nm thick Si:HfO_2 sample with 24:1 ALD cycle ratio showing evidence of SiO_2 interlayers within HfO_2 b) integrated line profile of the STEM intensity in comparison to c) ToF-SIMS results of TiN/Si:HfO_2/TiN capacitor structure. The black lines indicate similar positioning of the SiO_2 interlayers.

of SiO_2 during the growth of HfO_2 films, which will add $\backsim$6-12% of Si content. Since the FE-phase is the thermodynamic ground state, the need of the wake-up step (the application of alternate electric fields, typically along the out-of-plane direction) to observe the FE hysteresis loop, which is very common in HfO_2 thin films [50, 51], would be largely reduced in the obtained films. According to our prediction, the direction of the polarization lies along the growth direction in the most stable configuration, which is ideal for maximizing the remnant polarization of the films.

Interestingly, most of the FE films of HfO_2 are grown using the ALD technique, where the dopant ratio is achieved by performing a dopant oxide ALD cycle after a certain number of HfO_2 cycles [60]. After that, the obtained films go through a thermal treatment to induce crystallization. In this step, the dopants may diffuse in the films. However, the resulting samples present a modulation in dopant concentration along the growth direction, which indicates the presence of dopant layers [56, 151]. Figure 4.8 shows the scanning transmission electron microscopy (STEM) and Time-of-flight secondary ion mass spectrometry (ToF-SIMS) measurements performed by C.Richter et al. [56] to characterize the chemical composition in a 10 nm Si:HfO_2 dielectric. This figure has been taken from Ref.[56]. Figure 4.8 (a) presents a STEM image with discontinuous areas of darker contrast running across the center of the 10 nm Si:HfO_2 dielectric. Further, the integrated line profile of the STEM intensity in Figure 4.8 (b) displays two dips around the film's center, indicating dopant layering. Even after the crystallization anneal (at 1000°C for 1 s), the ToF-SIMS measurements demonstrate the presence of a periodic change in the Si concentration inside the HfO_2 layers. Hence, the ALD samples are adequately preconditioned to yield the FE-phase when they are subjected to the wake-up treatment—that is, the application of alternating electric fields along the out-of-plane direction. Thus, our theoretical predictions are consistent with the experimental evidence when the actual films are successfully grown. Further, it also suggests that the techniques with control of epitaxial growth, such as PLD, could follow the proposed preparation strategy in obtaining even better FE films.

Nevertheless, one has to bear in mind that the practical situation is far from the ideal crystals of doped HfO_2 considered in our simulations. In general, the ALD films are composed of randomly oriented grains. Therefore, a perfect alignment between the dopant layers and specific crystallographic axis is possible only in a fraction of grains [112]. Similarly, there are also complexities involved in the wake-up treatment [69, 152, 153]. Thus, using our predictions as a fail-safe technique for obtaining perfect samples of FE hafnia would be naive. However, we believe that our findings provide a new sight to explore in the direction of dopant ordering.

4.5 Conclusion

In this chapter, the stability issue of the FE-phase of HfO_2 has been discussed. We have considered the chemical dopants as an external factor to tune the stability of this phase of the material. In this study, we have found that some dopants have a very strong preference towards ordering inside the lattice: a fact which is largely ignored by most of the DFT studies. Most interestingly, this ordering of the dopants results in the stabilization of the FE-phase of HfO_2. We have predicted that the FE-phase with a full Si layer along the direction of the polarization constitutes the thermodynamically stable GS of the material. In contrast, Zr-like big dopants are not prone to ordering. Thus, the m-phase always prevails throughout the considered concentration range in $Hf_{1-x}Zr_xO_2$ system.

Notwithstanding our predictions are based on an ideal situation, we believe that this study would definitely bring some insights into how doping affects HfO_2, and how the ordering of the dopants stabilizes the FE-phase of the material.

Note that this study could be extended for other low-lying metastable phases of polymorphic HfO_2. Other dopants could also be considered. Furthermore, advanced DFT approaches for structure discovery might be used to discover even more stable dopant orderings. Such research, which may influence the expected relative stability of doped HfO_2 polymorphs, is worthwhile to pursue in the future.

Chapter 5

Piezoelectricity in HfO_2

In this chapter, we will discuss the piezoelectric response properties of HfO_2. In order to understand the response properties of the material in a better way, we will provide a detailed theoretical comparison with conventional piezoelectric $PbTiO_3$.

5.1 Background & Motivation

HfO_2 may become a promising candidate for applications as a piezoelectric due to its mature processing technology and CMOS compatibility compared to the perovskite oxides. However, the electro-mechanical response properties of the material have received little attention. Very recently, it has been predicted by first-principles that hafnia exhibits a negative longitudinal piezoelectric effect (NLPE) [154, 155], which means upon application of a compressive strain along the polar axis, the polarization will be enhanced.

Nevertheless, a positive longitudinal piezoelectric effect has been found in the experimental literature [19, 156, 157]. Thus, this creates a conflict with the existing first-principles studies. In addition, there is a lack of satisfying understanding of the atomistic reason behind this NLPE displayed by HfO_2.

In this study, we present a first-principles prediction of the piezoelectric properties of HfO_2. Our first-principles calculations confirm the NLPE found by J.Liu et al. [154, 155]. Here we consider a paradigmatic piezoelectric $PbTiO_3$ to perform a comparative study to understand the atomistic underpinnings leading to an opposite behavior in the case of HfO_2.

5.2 Results and Discussion

In this section, we present the results of our first-principles calculations of response properties of HfO_2 and $PbTiO_3$. We discuss our results for HfO_2 and $PbTiO_3$ in parallel to highlight the peculiarities in HfO_2.

5.2.1 Ferroelectricity in $PbTiO_3$ and HfO_2

The ferroelectricity in $PbTiO_3$ is caused by the cubic ($Pm\bar{3}m$) to tetragonal ($P4mm$) phase transition. Figure 5.1 (a) and (b) show the paraelectric cubic phase and the ferroelectric tetragonal phase of $PbTiO_3$, respectively. There are 5 atoms in the unit cell of cubic and tetragonal phases of the material. The tetragonal phase presents two symmetrically inequivalent O atoms, namely O_I and O_{II}. The spontaneous polarization is related to the

upward movement of the cations with respect to the O atoms as indicated by the arrows in Figure 5.1 (b). In this compound, the Pb and Ti cations are coordinated with 12 and 6 nearest neighbor O atoms in the cubic phase. However, the ferroelectric distortion results in a reduction in the coordination number of the cations. The Pb and Ti cations pass from being 12-fold and 6-fold coordinated in the paraelectric phase to 8-fold and 5-fold coordinated in the ferroelectric phase. All the Ti−O bond distances are equal to 1.96 Å in the cubic phase. However, the central Ti atom forms the shortest and strongest bond with one of the O atoms belonging to the type I family with a bond length of 1.77 Å as marked in Figure 5.1(b).

Here, we recapitulate the development of ferroelectricity in HfO_2 through the formation of an orthorhombic phase with space group $Pca2_1$ (FE-phase). The spontaneous polarization in the FE-phase can be understood by comparing the high symmetry cubic paraelectric structure with space group $Fm\bar{3}m$ (c-phase). Figure 5.1 (c) and (d) show the paraelectric

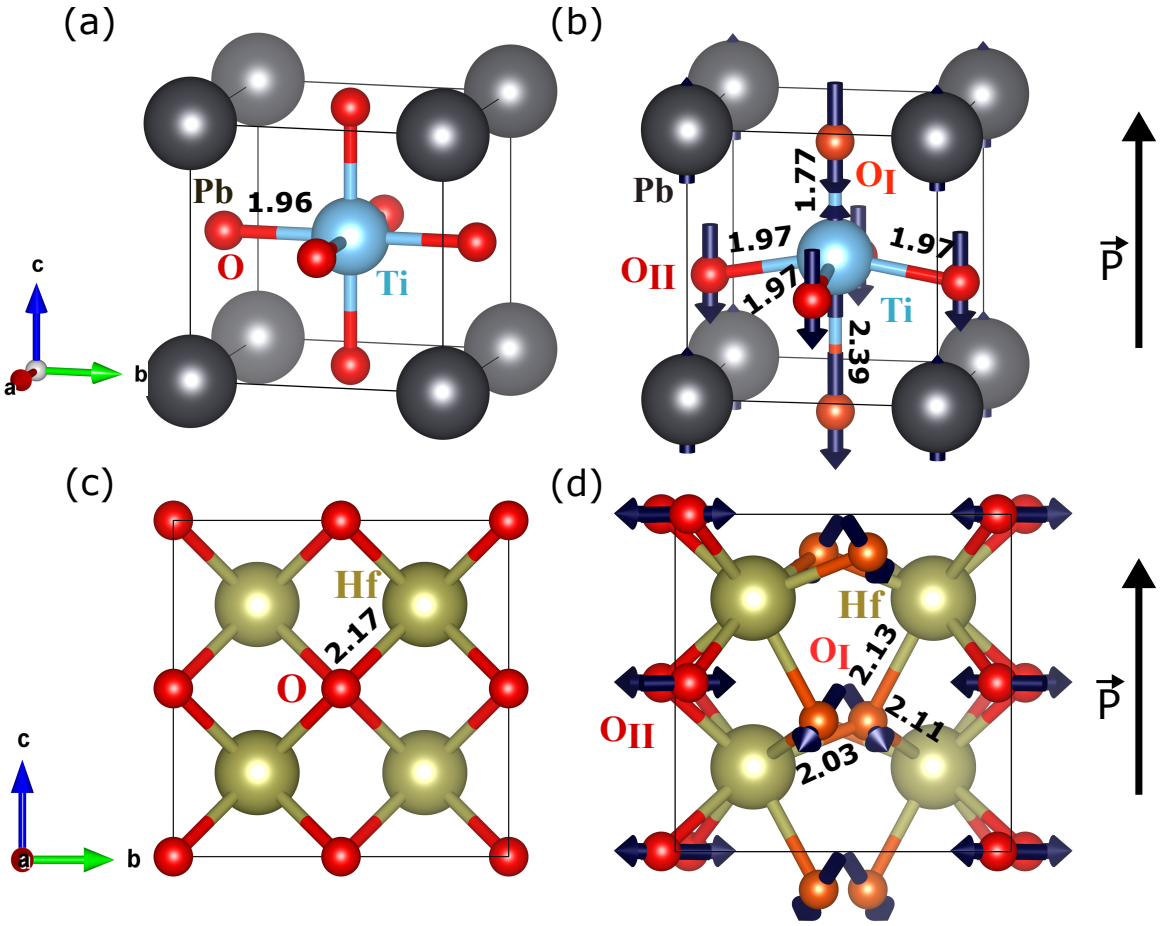

Figure 5.1: The structures of the (a) paraelectric cubic ($Pm\bar{3}m$)and (b) ferroelectric tetragonal phase ($P4mm$) of $PbTiO_3$, and (c) paraelectric c-phase ($Fm\bar{3}m$) and (d) FE-phase ($Pca2_1$) of HfO_2. The black arrows represent the direction of the polarization in both materials. The distortions from paraelectric to ferroelectric states are shown by the blue arrows. The ferroelectric state of $PbTiO_3$ (tetragonal phase) and HfO_2 (FE-phase) present two symmetry inequivalent O atoms labeled by O_I (shown in orange) and O_{II} (shown in red). The relevant bond distances marked in the figure are in Å.

c-phase and the FE-phase, respectively. As mentioned in Chapter 3, all the Hf and O atoms are symmetrically equivalent in the c-phase. In contrast, the Hf atoms are symmetrically equivalent in FE-phase, but it features two symmetry inequivalent O atoms labeled by O_I (shown in orange color in Figure 5.1(d)) and O_{II} (shown in red color in Figure 5.1(d)). The upward spontaneous polarization is caused by the downward movement of O_I sublattice in the FE-phase with respect to the high symmetry c-phase, as shown by the blue arrows pointing downward in Figure 5.1 (d). The displacements of the O_{II} atoms do not contribute to the development of the polarization. Note that the Hf cations pass from being 8-fold coordinated in the paraelectric phase to 7-fold in the ferroelectric phase. All the Hf−O bond lengths are equal to 2.17 Å in c-phase, whereas the Hf−O_I bonds become shorter to 2.13 Å, 2.11 Å, and 2.03 Å in the FE-phase as also marked in Figure 5.1 (d).

We will discuss the response properties of HfO_2 and $PbTiO_3$ in parallel in the following sections.

5.2.2 First-principles prediction of piezoelectric response in $PbTiO_3$ & HfO_2

The piezoelectric tensor $e_{\alpha j}$ is defined as :

$$e_{\alpha j} = \frac{\partial P_\alpha}{\partial \eta_j} \tag{5.1}$$

where P_α is the component of the polarization along direction α, and η_j is the strain labeled with Voigt notation (j=1...6). It is important to mention that we work with the FE-phase with positive polarization in both $PbTiO_3$ and HfO_2. As discussed in Chapter 2, the piezoelectric tensor $e_{\alpha j}$ is decomposed into a frozen-ion contribution ($\bar{e}_{\alpha j}$) and a lattice-mediated part (defined as $e_{\alpha j} - \bar{e}_{\alpha j}$). We decompose these two contributions for the sake of the analysis.

System	Index	$\bar{e}$	e^{latt}	e	d
$PbTiO_3$	31	0.23	1.39	1.62	−39
	33	−0.30	5.25	4.95	208
	15	0.03	4.55	4.58	78
HfO_2	31	−0.37	−0.94	−1.31	−1.71
	32	−0.34	−0.99	−1.33	−1.77
	33	0.62	−2.06	−1.44	−2.51
	15	−0.28	0.08	−0.20	−2.03
	24	−0.20	0.84	0.64	6.74

Table 5.1: Computed piezoelectric tensors for $PbTiO_3$ and HfO_2. We present the frozen-ion ($\bar{\mathbf{e}}$), lattice-mediated part ($\mathbf{e^{latt}}$) , total ($\mathbf{e}$) direct piezoelectric tensor (in C m^{-2}), as well as the total converse piezoelectric tensor $\mathbf{d}$ (in pm V^{-1}). All indices are in voigt notation.

Table 5.1 shows the computed values for $\boldsymbol{e}$, $\bar{\boldsymbol{e}}$, and $\boldsymbol{d}$ tensor of $PbTiO_3$ and HfO_2 using DFPT. The relation between the $\boldsymbol{d}$ tensor and $\boldsymbol{e}$ tensor (also discussed in Chapter 2) is as follows:

$$d_{\alpha j} = \frac{\partial P_\alpha}{\partial \sigma_j} = S_{jk} e_{\alpha k} \tag{5.2}$$

System	Index	$\bar{C}$	C	$\bar{S}$	S
$PbTiO_3$	11	288.3	251.3	4.62	6.93
	12	122.5	103.2	−1.41	0.19
	13	118.5	74.5	−1.35	−10.24
	33	281.7	51.8	4.69	48.72
	44	85.7	58.6	11.66	17.05
	66	100.2	100.2	9.98	9.98
HfO_2	11	465.3	413.6	2.65	2.99
	12	181.3	162.3	−0.78	−0.99
	13	151.7	123.4	−0.61	−0.60
	22	485.0	407.8	2.59	3.08
	23	165.6	132.8	−0.69	−0.73
	33	445.7	394.6	2.71	2.97
	44	127.0	94.4	7.87	10.59
	55	116.7	98.0	8.56	10.20
	66	169.3	140.4	5.90	7.12

Table 5.2: Computed elastic and compliance tensors of the ferroelectric state of $PbTiO_3$ and HfO_2.The **C** tensor is in GPa and **S** tensor is in TPa^{-1}. We show the frozen-ion and total elastic and compliance tensor.

where σ_j is the stress labeled in Voigt notation, and S is the inverse of the elastic tensor (C^{-1}), known as the compliance tensor. Note that the d tensor is of particular relevance because of its easy accessibility in the experiments and applications.

Let us focus on the "33" entries in both systems. The value of e_{33} is positive in $PbTiO_3$, indicating that a positive strain of the unit-cell along the direction of polarization will yield an enhancement of polarization. In contrast, the value of the e_{33} is negative in HfO_2. We recall that the unperturbed state has $P_3 > 0$, and $P_1 = P_2 = 0$. Therefore, the negative value of e_{33} suggests that upon an application of a positive strain along the polar direction, the polarization will be reduced compared to its unperturbed state.

Interestingly, we observe that the lattice-mediated part is larger than the frozen-ion part in both systems, and they have opposite signs. Thus, it is clear that the lattice-mediated part is controlling the sign of the e_{33}.

We notice that the $e_{\alpha j}$ and $d_{\alpha j}$ coefficients are larger in magnitude in $PbTiO_3$ than in HfO_2. Interestingly, the difference becomes much larger for the $d_{\alpha j}$ coefficients: for example we find a d_{33} of 208 pm V^{-1} for $PbTiO_3$ and -2.51 pm V^{-1} in the case of HfO_2. This massive d_{33} response of $PbTiO_3$ is in agreement with previous experimental [158] and theoretical [159] literature. We find that the main reason behind the giant response is the softness of the compound along the polar direction. Table 5.2 presents the values of the elastic tensor of $PbTiO_3$ and HfO_2. The values of $C_{33} = 51.8$ GPa and $S_{33} = 48.72$ TPa^{-1} for $PbTiO_3$, which is much softer than HfO_2 with $C_{33} = 394.6$ GPa and $S_{33} = 2.97$ TPa^{-1}, explaining the large d_{33}.

In addition, it is also interesting to note that the transverse components of the $\boldsymbol{e}$ tensor, i.e., e_{31} and e_{32}, are also negative for HfO_2, which indicates an overall contraction upon an application of electric field $\boldsymbol{\mathcal{E}}$ along the direction of $\boldsymbol{P}$. Auxetic materials exhibit a negative Poisson's ratio, which is characterized by a lateral expansion in the direction perpendicular to the applied expansive stress or vice versa. J.Liu et al. introduced HfO_2 as an"electric

auxetic" material where the material will expand or contract in all directions in response to an electric field [155].

5.3 Origin of NLPE

Having found the negative piezoresponse of HfO_2, it is of fundamental interest to investigate the origin of this phenomenon. The DFPT calculations allow us to track down the constituents of the lattice-mediated part of the $\boldsymbol{e}$ tensor. As presented in Chapter 2, we write the piezoelectric tensor as

$$e_{\alpha j} = \bar{e}_{\alpha j} + \Omega_0^{-1} Z_{m\alpha} (\Phi^{-1})_{mn} \Lambda_{nj} \,, \tag{5.3}$$

where the second part in the right-hand side of this equation presents the lattice-mediated part of the $\boldsymbol{e}$ tensor. The lattice-mediated part depends on the unit-cell volume Ω of the unperturbed system, the Born effective charges $\boldsymbol{Z}$, the force-constant matrix $\boldsymbol{\Phi}$, and the force response internal strain tensor $\boldsymbol{\Lambda}$.

$PbTiO_3$	Pb	$\begin{bmatrix} 3.76 & 0 & 0 \\ 0 & 3.76 & 0 \\ 0 & 0 & 3.46 \end{bmatrix}$
	Ti	$\begin{bmatrix} 6.20 & 0 & 0 \\ 0 & 6.20 & 0 \\ 0 & 0 & 5.24 \end{bmatrix}$
	O_I	$\begin{bmatrix} -2.13 & 0 & 0 \\ 0 & -2.13 & 0 \\ 0 & 0 & -4.43 \end{bmatrix}$
	O_{II}	$\begin{bmatrix} -5.18 & 0 & 0 \\ 0 & -2.64 & 0 \\ 0 & 0 & -2.14 \end{bmatrix}$
HfO_2	Hf	$\begin{bmatrix} 5.17 & -0.01 & 0.04 \\ -0.36 & 5.46 & 0.15 \\ -0.04 & 0.23 & 4.99 \end{bmatrix}$
	O_I	$\begin{bmatrix} -2.50 & -0.96 & 0.31 \\ -0.76 & -2.94 & -0.68 \\ 0.32 & -0.63 & -2.48 \end{bmatrix}$
	O_{II}	$\begin{bmatrix} -2.68 & -0.15 & 0.25 \\ -0.09 & -2.51 & 0.16 \\ 0.29 & 0.12 & -2.50 \end{bmatrix}$

Table 5.3: Computed Born effective charges of $PbTiO_3$ and HfO_2 (in units of electronic charge).

Table 5.3 shows the computed Born effective charge tensors for $PbTiO_3$ and HfO_2. By inspecting the values of the Born effective charges in both materials, we do not identify any noteworthy feature. HfO_2 shows the expected sign and charge values exceeding the nominal charges of $+4$ for Hf and -2 for O atoms. This characteristic indicates a mixed ionic-covalent character of the chemical bonds in the material, which is typical for other ferroelectrics like in $PbTiO_3$. Due to low symmetry, HfO_2 presents small non-zero off-diagonal components. However, that does not affect the negative sign of e_{33}.

We also note that there is nothing peculiar in the force-constant matrices $\mathbf{\Phi}$ of both materials. They are positively defined tensors representing the ferroelectric phase as a stable equilibrium state. Thus, the force-constant matrices are not relevant for the present discussion.

$PbTiO_3$	Pb	0	0	0	0	3.34	0
		0	0	0	3.15	0	0
		6.89	6.89	5.01	0	0	0
	Ti	0	0	0	0	−0.51	0
		0	0	0	0.50	0	0
		−3.18	−3.18	30.76	0	0	0
	O_I	0	0	0	0	−0.44	0
		0	0	0	−0.69	0	0
		−5.19	−5.19	−34.26	0	0	0
	O_{II}	0	0	0	0	−2.94	0
		0	0	0	−0.12	0	0
		−2.04	3.55	−0.81	0	0	0
HfO_2	Hf	−4.02	0.00	−2.29	8.39	0.83	0.79
		−1.04	11.52	−1.40	4.50	3.58	5.87
		−1.87	1.45	−4.07	−2.83	−2.61	3.42
	O_I	2.06	−0.63	1.09	−5.87	−3.29	0.91
		−1.97	−1.75	−1.43	−2.77	−4.60	−2.34
		−1.61	0.42	3.22	1.36	0.29	−4.53
	O_{II}	−5.87	1.10	−1.07	4.67	2.46	0.06
		0.79	7.87	0.54	−1.71	4.10	0.52
		3.46	1.86	0.85	1.27	−1.36	5.44

Table 5.4: Computed force-response internal-strain tensor (Λ) (eV/Angstrom) for the symmetry inequivalent atoms in $PbTiO_3$ and HfO_2. The 3 rows correspond to the 3 spatial direction x, y, and z; the 3 columns correspond to the 6 strain indices, which are in Voigt notation. We mark the entries in bold controlling the e_{33} as discussed in the text.

Table 5.4 shows the computed force-response internal strain tensors of $PbTiO_3$ and HfO_2. As mentioned in Chapter 2, the $\mathbf{\Lambda}$ tensor quantifies atomic forces resulting from strain. Here we focus on the "33" entries for each of the atoms in both systems, where it quantifies force along direction 3 caused by a positive strain ($\eta_3 > 0$). Note that the strain-induced forces are positive for the cations and negative for the two symmetry-inequivalent

O atoms in $PbTiO_3$. This suggests that the cations will move up, and the O atoms will move down upon a vertical stretching in this material. This movement of the atoms will result in an enhancement of polarization, since the unperturbed state has $P_3 > 0$; hence the e_{33} is positive.

Contrastingly, the value of the Λ_{33} is negative for Hf and positive for two symmetrically inequivalent O atoms, which means that, upon a vertical stretching, the Hf atoms will tend to move down while the O atoms will tend to move up inside the lattice. As a result, this strain-induced movement will yield a reduction of polarization, since the unperturbed state has $P_3 > 0$. Therefore, we get the negative sign of e_{33}. The key to understanding the sign of the e_{33} is thus in the Λ tensor.

5.4 Physical insight

The above discussion provides an explanation of the NLPE in HfO_2 from a numerical point of view. However, a physical understanding is still missing.

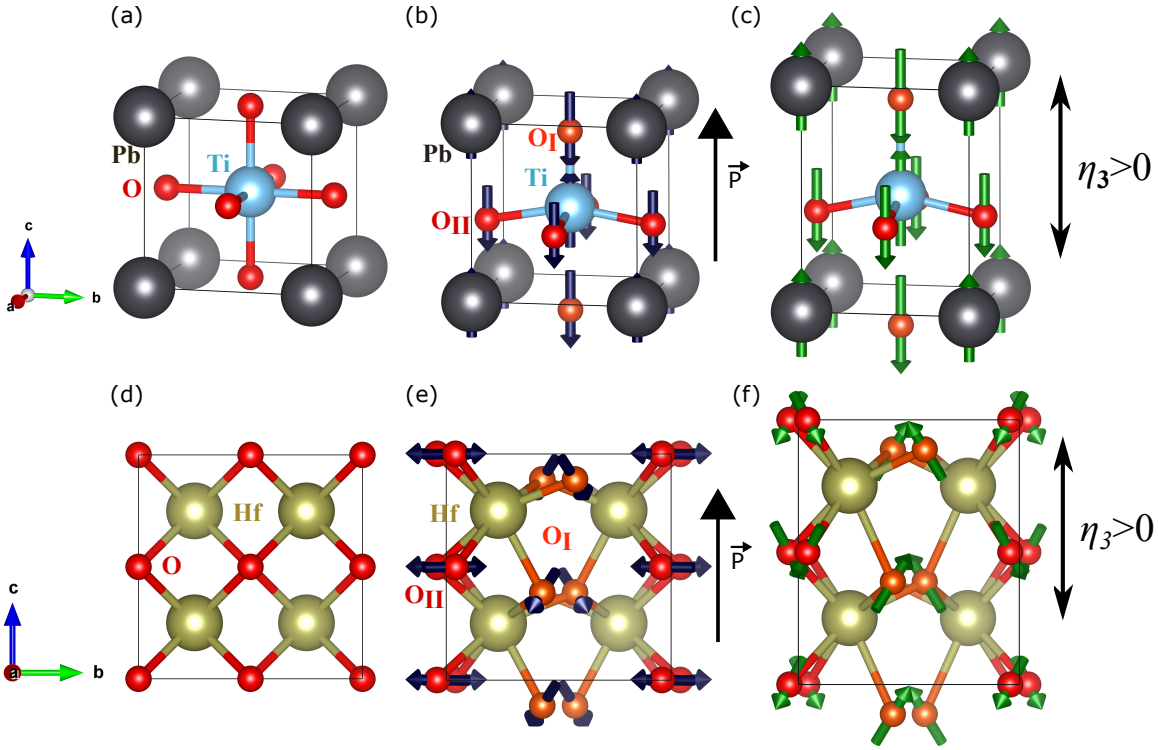

Figure 5.2: (a) Cubic phase ($Pm\bar{3}m$), and (b) tetragonal phase ($P4mm$) of $PbTiO_3$ similar like in Figure 5.1. In panel c, the tetragonal phase is subjected to a vertical strain $\eta_3 > 0$. In the sketch the strain is exaggerated for better visibility. The green arrows in panel c represent how the atoms react in response of the strain. Panels d,e,f are analogous to the top panel, but represents the (d) paraelectric, (e) ferroelectric phase of HfO_2, and (f) the response of the atoms in an application of the vertical tensile strain.

In the following sections first we discuss the behavior of $PbTiO_3$ and then of HfO_2.

$PbTiO_3$

We start by explaining the bonding mechanism in $PbTiO_3$, which will allow us to understand the piezoelectric response of the material. As discussed above, the ferroelectric distortion from a paraelectric cubic state yields a ferroelectric tetragonal structure where the cations tend to move up with respect to the O atoms in $PbTiO_3$ as shown in Figure 5.2 (a) and (b). Now, imagine we apply a positive strain ($\eta_3 > 0$) to the ferroelectric state along the polar direction as shown in Figure 5.2 (c). We assume that as a response, the atoms will rearrange themselves inside the lattice and try to maintain the suitable bond lengths of the dominating bonds. Let us focus on the central Ti atom. From a paraelectric to a ferroelectric phase transition, the central Ti atom forms the strongest and shortest bond with the type I O atoms (O_I) marked in orange color in Figure 5.2 (b). Therefore, as a response to the applied positive strain, the Ti atom tends to move up, and O_I atom tends to move down to preserve the strongest bond between them as shown by the green arrows in Figure 5.2 (c), which is indeed reflected by the values of Λ_{33}. Similarly, we can explain the movement of Pb and O_{II} atoms as a response of $\eta_3 > 0$. This movement of the atoms results in an enhancement of polarization. Thus we get a positive sign of e_{33}.

HfO_2

To identify the strongest Hf−O bond is not easy in HfO_2 because of its complex chemical bond environments. However, we find an interesting picture that may allow us to better understand our results.

Again we focus on the ferroelectric distortion of FE-phase from a paraelectric c-phase as shown in Figure 5.2 (d) and (e), which involve downward displacement of the O_I sublattice. (The movement of the O_{II} atoms does not contribute to the development of the polarization.) Further, if we stretch the cell along the polar direction as shown in Figure 5.2 (f), the O_I atoms tends to move up.

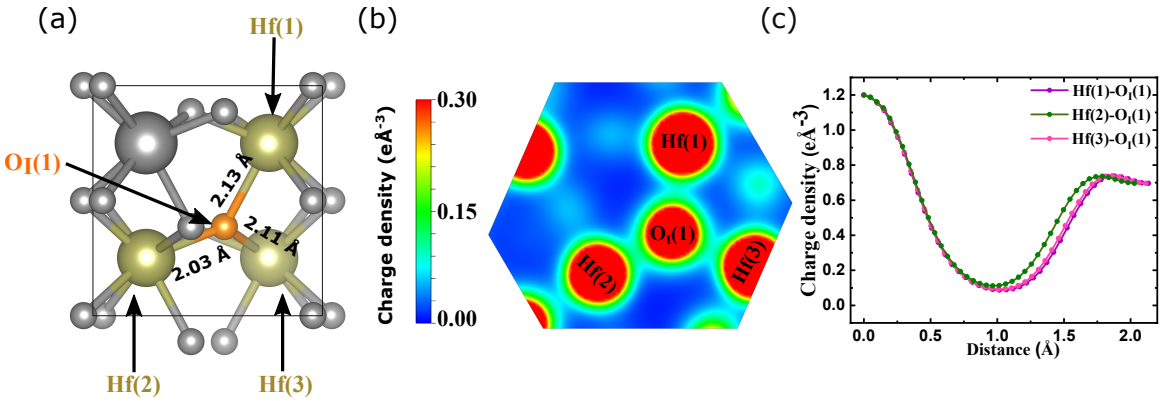

Figure 5.3: Sketch of the ferroelectric state of HfO_2 where one representative O_I atoms and its three nearest neighbour Hf atoms are marked. All the three Hf−O_I(1) bond distances are mentioned. The computed electronic charge density of unstrained HfO_2 are ahown in panels (b) and (c). Panel (b) shows the contour plot within a plane containing highlighted O_I atom and its three nearest neighbor Hf atoms ((as shown in panel (a)). Panel (c) shows the line profile of the charge density along the bond lengths connecting O_I(1) atom with three nearest Hf atoms.

To understand the movement of the atoms as a response to the applied strain, we focus on the atomic environment of the O_I atom highlighted in Figure 5.3 (a). We use a number in parenthesis to refer the individual atoms, which belong to a particular sub-lattice in this Figure 5.3 (a). The $O_I(1)$ atom has three nearest neighboring Hf atoms. As mentioned above, we notice that the Hf$-O_I$ bonds in the FE-state get shorter compared to its cubic phase. The Hf(1)$-O_I(1)$, Hf(2)$-O_I(1)$, and Hf(3)$-O_I(1)$ bond distances are 2.13 Å, 2.03 Å, and 2.11 Å, respectively as also indicated in Figure 5.3 (a).

Additionally, Figures 5.3 (b) and (c) present the computed equilibrium charge density, which suggests that the $O_I(1)$ has similar strong bonds with all the three nearest neighbor Hf atoms. However, we can make a critical observation by inspecting the atomic environment of the $O_I(1)$ atom and how the strain along the polar direction affects the position of the $O_I(1)$ ion. Since all the bonds are similarly strong, the bond that is affected the most due to the applied perturbation can be expected to dominate the response to the applied positive strain. It is noted that only the Hf(1)$-O_I(1)$ bond is aligned with the polar axis. Therefore, this bond will be most affected by vertical stretching. On the other hand, the other two bonds Hf(2)$-O_I(1)$ and Hf(3)$-O_I(1)$ lie mostly in the horizontal plane as shown in Figure 5.3 (a), and will be less affected by the stretching along the vertical direction. Thus, the $O_I(1)$ atom will tend to move up to maintain the bond distance with Hf(1) under application of $\eta_3 > 0$. This is exactly what we see in Figure 5.2 (f) as well as in the $\mathbf{\Lambda}$ tensor. Interestingly, this upward movement of $O_I(1)$ (Figure 5.2 (f)) opposes the downward shift of the same ion when the polar phase condenses (Figure 5.2 (e)). As a result, we get a reduction of polarization, which yields a negative e_{33}.

The difference between $PbTiO_3$ and HfO_2 is represented schematically in Figure 5.2. In $PbTiO_3$, the reaction of the atoms adds on to the spontaneous polarization, whereas the ionic reaction of the atoms in HfO_2 goes against the distortion responsible for spontaneous polarization as illustrated in Figures 5.2 (c), (d) and (e), (f), respectively. In the end, the chemical environment of the $O_I(1)$ atoms inside the HfO_2 lattice controls the NLPE.

5.5 Prediction of a tunable longitudinal piezoelectric coefficient in HfO_2

Based on the explanation above, we make a hypothesis: by controlling the preferred bond lengths of piezoelectrically active $O_I(1)$ atoms, we may affect the magnitude of the e_{33}. Therefore, e_{33} would be more negative if we decrease the bond length of Hf(1)$-O_I(1)$, whereas it will be less negative if we increase the bond length of Hf(1)$-O_I(1)$. In the latter case, the response will thus be controlled by the stronger in-plane lying Hf(2)$-O_I(1)$ and Hf(3)$-O_I(1)$ bonds.

To test our hypothesis, we decided to apply in-plane epitaxial strain to the unit-cell of the FE-phase of HfO_2, and allow the out of plane lattice parameter to relax. This approach could give us the desired control of the Hf(1)$-O_I(1)$ bond length. We first performed a structural relaxation by applying the isotropic epitaxial strain in the plane perpendicular to the polar direction on the FE-phase of HfO_2. In this simulation the magnitude of the in-plane lattice parameters are fixed to $a = a_0(1 + \eta_{\text{epi}})$ and $b = b_0(1 + \eta_{\text{epi}})$, where a_0 and b_0 are the lattice constants of the unperturbed state, and the angle is fixed to 90 °. We allow the out of plane lattice parameter to relax. The schematic of our simulation cell under epitaxial strain (η_{epi}) is shown in Figure 5.4.

We find that the FE-phase is a stable structure in a wide range of epitaxial strains.

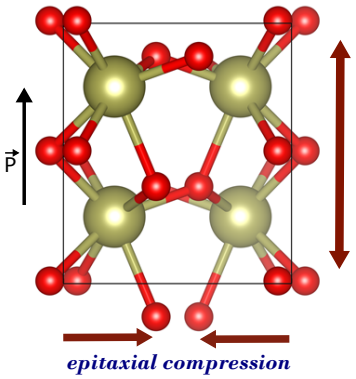

Figure 5.4: Schematic of the applied epitaxial compression to the FE-phase of HfO_2. The strain is applied to the in-plane lattice parameter. The in-plane lattice parameters are fixed at the strain value, while the out of plane lattice parameter is allowed to relax. The epitaxial expansion is also applied in a similar manner.

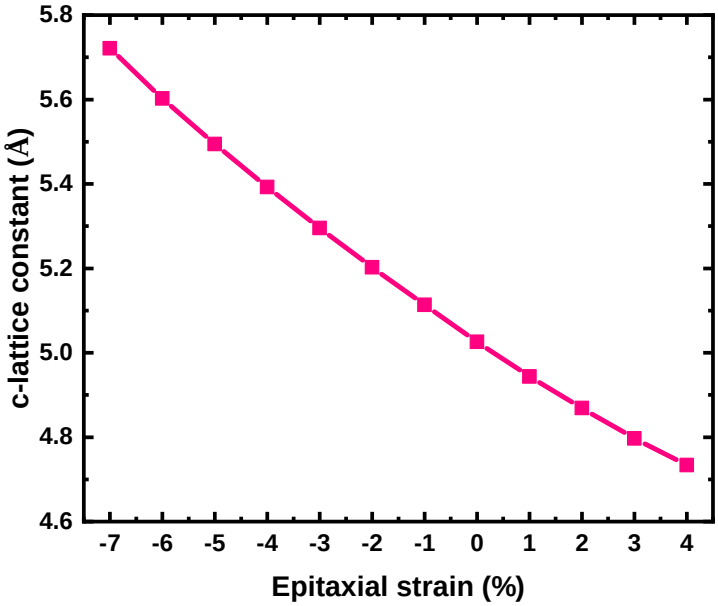

Figure 5.5: Evolution of c lattice parameter as a function of epitaxial strain.

Beyond -7% on the negative side and $+4\%$ on the positive side, this phase becomes unstable and transforms into other structures, which are not relevant here. Figure 5.5 shows the η_{epi} dependence of the c lattice parameter, which grows with increasing compressive strain in the plane.

We monitored the bond lengths of the $O_I(1)$ atom with its three nearest neighboring Hf atoms as marked in the Figure 5.3(a). Figure 5.6 shows the evolutions of these three bond lengths as a function of η_{epi}, which follows the expected behavior. The vertically aligned $Hf(1)-O_I(1)$ bond length is increased with increasing compressive strain ($\eta_{epi} < 0$), which follows the same trend as c lattice parameter, as shown in Figure 5.5. On the other hand,

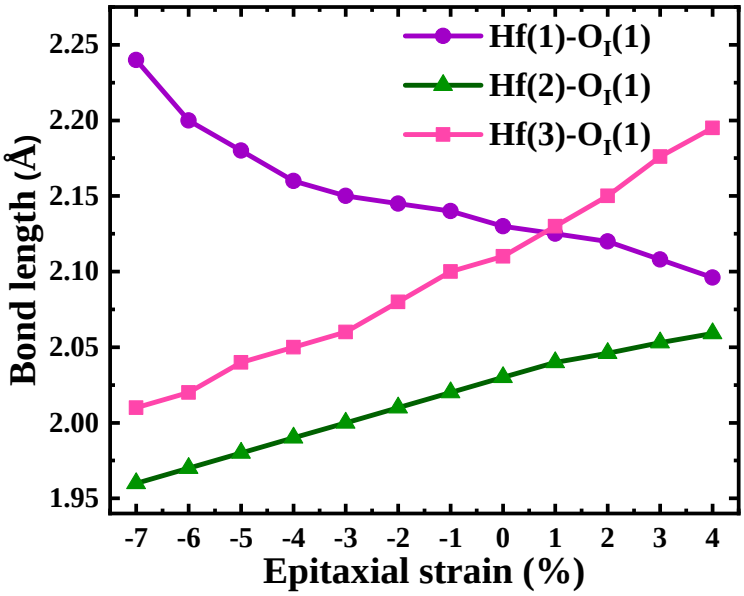

Figure 5.6: Hf(1)−O_I, Hf(1)−O_I, and Hf(1)−O_I bond distances as defined in Figure 5.3 (a) are computed as a function of epitaxial strain.

the Hf(2)− O_I(1) and Hf(3)− O_I(1) bonds, which are largely parallel to the plane get shrunk upon in-plane compression.

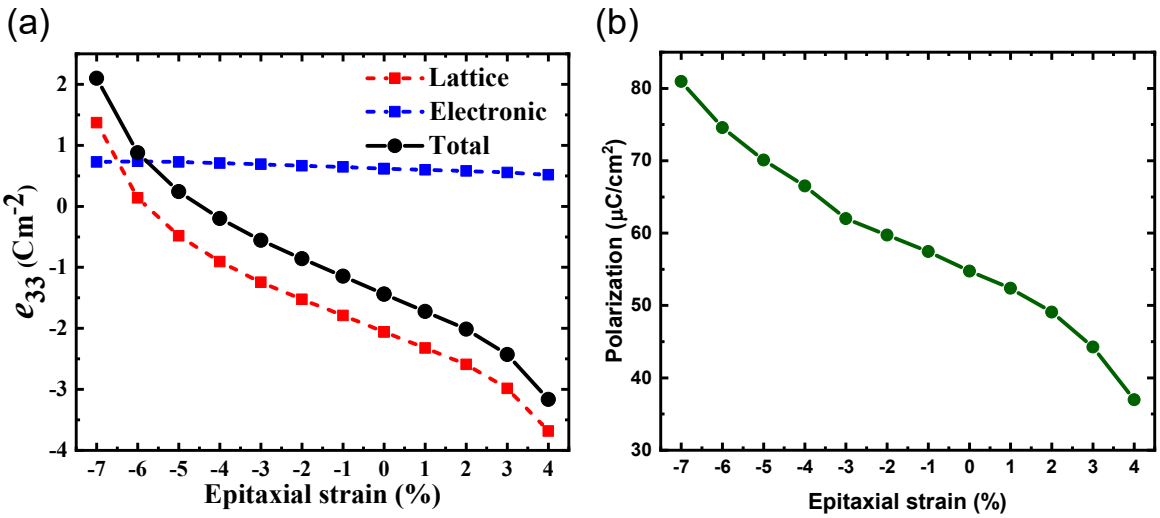

Figure 5.7: (a) Computed longitudinal piezoelectric coefficient (e_{33}) of FE-phase of HfO_2 as a function of epitaxial strain. The total response (black) is decomposed into frozen-ion (blue), and lattice-mediated (red) part. (b) Computed polarization at each strain values as a function epitaxial strain.

Figure 5.7 (a) presents the epitaxial strain dependence on the e_{33} obtained from DFPT calculations. Note that the frozen-ion contribution of the e_{33} is nearly constant throughout

the strain range. In contrast, the lattice-mediated part of the e_{33} changes massively. Thus the total response also changes with strain as shown in Figure 5.7 (a). It reaches its most negative response value at the largest tensile strain here considered, whereas it becomes positive as we apply compressive strain of about -5%.

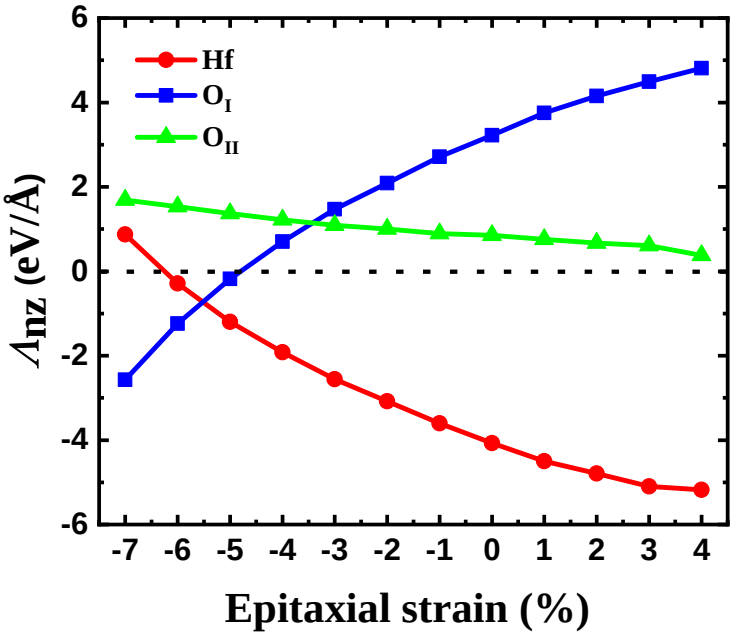

Figure 5.8: The $\mathbf{\Lambda}$ component, as a function of epitaxial strain. The shown component of $\mathbf{\Lambda}$ quantifies the forces acting on the Hf, O_I and O_{II} atoms along the third (vertical) direction as a consequence of an applied strain η_3>0.

Figure 5.7 (b) presents the computed polarization for the structure at each strain values. It is important to note that the sign change of e_{33} occurs despite the fact that all the considered structures in the whole range of η_{epi} have $P_3 > 0$. The polarization grows beyond 70 μC/cm^2 for an epitaxial compression of -5%, exactly where the e_{33} becomes positive. This evolution of the polarization is consistent with the structural distortions as shown by the enhancement of the Hf(1)$-$ O_I(1) bond distance in Figure 5.6. Thus, the material remains in the same polar state but e_{33} changes sign. This is the first time that we see such an interesting effect in a ferroelectric.

Having found this surprising behavior of e_{33} as a function of η_{epi}, we decide to track down the reason behind the sign changes. Let us monitor the $\mathbf{\Lambda}$ tensor in this case as we have done for the $\eta_{epi} = 0\%$ case.

Figure 5.8 presents the Λ_{nz} component for Hf, O_I and O_{II} atoms as a function of η_{epi}. Interestingly, we find that the response is mainly driven by the movement of Hf and O_I atoms, whereas the response associated to O_{II} anions is largely independent of the epitaxial strain. The sign change of e_{33} is consistent with the evolution of the Λ_{nz} component as a function η_{epi}, where we see the direction of the displacements of O_I atoms is reversed at -5% compression.

Finally, we can verify whether these findings are consistent with our physical explanation of the sign change of e_{33}. To understand the physical picture behind the sign change, we

consider two limiting cases with $\eta_{epi} = -7\%$ and $\eta_{epi} = +4\%$. Figure 5.9 displays the computed charge density for the limiting cases with $\eta_{epi} = -7\%$ (panel a and b) and $\eta_{epi} = +4\%$ (panel c and d). Figures 5.9 (b) and (d) display the line profile of the charge density connecting the highlighted O_I atom in Figure 5.3(a) ($O_I(1)$) with its all three nearest neighbor Hf atoms.

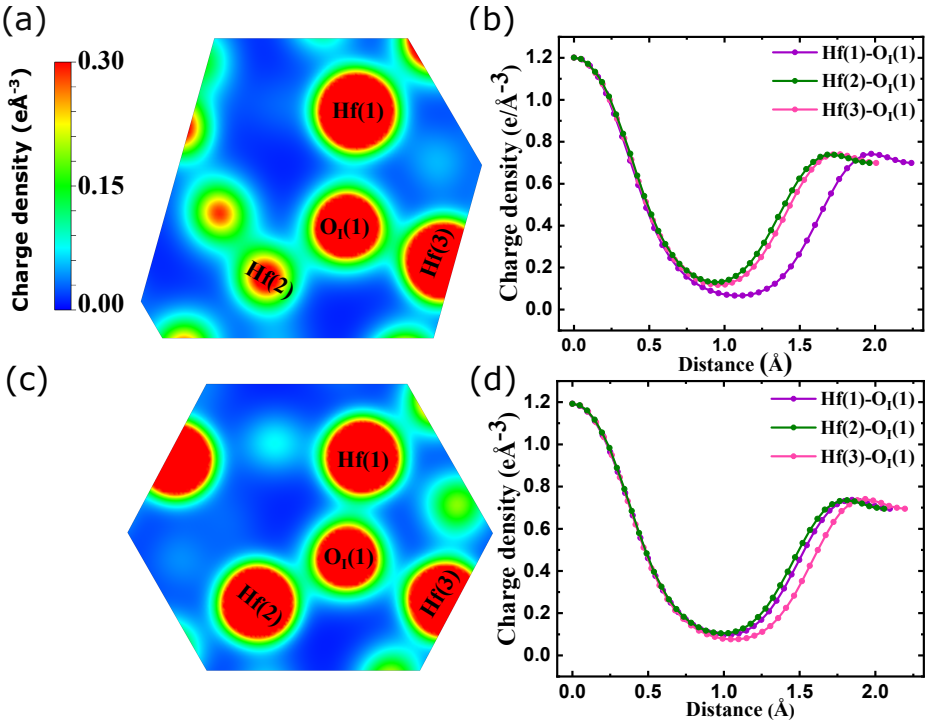

Figure 5.9: Computed electronic charge density of epitaxially strained HfO_2 at η_{epi}=−7% (panels a and b), and at η_{epi}=+4% (panels c and d). Panels (a) and (c) show a contour plot within a plane containing the highlighted O_I atom and its three nearest neighbor Hf atoms as shown in Figure 5.3 (a). Panels (b) and (d) show the line profile of the charge density along the bond lengths connecting $O_I(1)$ atom with three nearest Hf atoms.

First, we focus on the −7% compressed case. Due to strong in-plane compression, the vertical lying Hf(1)− $O_I(1)$ bond becomes very weak, which is also consistent with the large Hf(1)− $O_I(1)$ bond length in Figure 5.6. In this state, the response will be controlled by the stronger nearly-in-plane Hf(2)−$O_I(1)$ and Hf(3)− $O_I(1)$ bonds. The charge density plots in Figure 5.9 (a) and (b) are also consistent with our expectations. It clearly shows that the two in-plane Hf(2)−$O_I(1)$ and Hf(3)−$O_I(1)$ bonds are stronger than the Hf(1)−$O_I(1)$ bond. Therefore, we expect that, as a result of a vertical stretching, the O_I anions will move downwards, while Hf(2) and Hf(3) will move upwards to preserve the suitable bond lengths between them. This exactly follows the way O_I atoms move while condensing the ferroelectric distortions from a c-phase to FE-phase. Hence, it yields a positive value of e_{33}.

Next, in the case of +4% strained system, we see that the Hf(1)−$O_I(1)$ and Hf(2)−$O_I(1)$ links are stronger than the Hf(3)−$O_I(1)$ bond. Like the unstrained case, the vertical lying Hf(1)−$O_I(1)$ bond will be more affected by the vertical stretching than the Hf(2)−$O_I(1)$ bond in this case. Therefore, the $O_I(1)$ anion will move up to maintain the bond length with Hf(1). The only difference with the unstrained case is that the vertical bond is expected to become more dominant, which results in a stronger negative e_{33}.

Hence, we confirm that the longitudinal piezoelectric coefficient of HfO_2 is tunable and can even be reversed by controlling the chemical environment of the piezoelectrically active O_I atoms. We achieve this control by applying epitaxial strain. The sign of e_{33} is determined by the peculiar environment of the said atoms and the tendency to maintain their preferable bond lengths with nearest neighboring Hf atoms. Thus, we achieve the key to control the magnitude as well as the sign of e_{33}.

5.6 Connection with Experiments

In this section we compare our theoretical result of the longitudinal piezoelectric coefficient of HfO_2 with the experiment. In this context, one has to consider a vital feature of most of the samples of HfO_2, which is they are polycrystalline. The typically measured piezoelectric response in a polycrystalline film corresponds to an effective average. The randomly oriented grains are poled to display a polarization with a positive P_3 component. Thus the estimated effective $d_{33,\text{eff}}$ will be as follows [160, 161]:

$$\begin{aligned} d_{33,\text{eff}} &= \big\langle \cos\theta \left[(d_{15}+d_{31})(\sin^2\theta\sin^2\varphi) + (d_{24}+d_{32})(\sin^2\theta\cos^2\varphi) + d_{33}\cos^2\theta \right] \big\rangle \\ &= (d_{15}+d_{31})\langle\cos\theta\sin^2\theta\rangle\langle\sin^2\varphi\rangle + (d_{24}+d_{32})\langle\cos\theta\sin^2\theta\rangle\langle\cos^2\varphi\rangle + d_{33}\langle\cos^3\theta\rangle \\ &= \frac{1}{3\pi}(d_{15}+d_{31}+d_{24}+d_{32}) + \frac{4}{3\pi}d_{33} \end{aligned} \tag{5.4}$$

where $\langle ... \rangle$ represents an average over the Euler angles φ and θ. The Euler angles span over all possible orientations with $P_3 > 0$ (i.e. $0 < \theta < \pi/2$ and $0 < \varphi < 2\pi$). Interestingly, our obtained value of $d_{33,\text{eff}}$ is -0.94 pm V^{-1}, which indicates that even for the polycrystalline HfO_2 samples we expect to measure the negative longitudinal piezoelectric response. Therefore, we predict that the value of d_{33} of HfO_2 can be between -2.5 pm V^{-1} (single-crystal limit) and -0.94 pm V^{-1} (untextured, fully-poled polycrystalline limit).

The previous experimental studies claim the presence of a positive longitudinal piezoresponse in the HfO_2 sample, which include 10 nm Si-doped HfO_2 [162], 70 nm Y-doped HfO_2 [157], and 1 μm thick La-doped HfO_2[156]. However, there is one experimental result available in the literature [163] which points to a negative piezoresponse [164].

Recently, the group of Alexei Gruverman has reported negative d_{33} in a 20 nm thick La-doped HfO_2 sample. They use the materials with well-known piezoelectric properties to compare with: $PbZr_{1-x}Ti_xO_3$ (PZT) (with x=0.6) characterized by a positive piezoelectric coefficient [165, 166], and polyvinylidene fluoride (PVDF) [167, 168] characterized by a negative piezoelectric coefficient. Figure 5.10 displays the dynamical measurements of longitudinal piezoelectric coefficient using piezoresponse force microscopy (PFM) for (a) PZT, (b) PVDF, and (c) La:HfO_2. In Figure 5.10 (a), the clockwise rotation of the PFM loop in case of PZT indicates the positive sign of $d_{33,\text{eff}}$. Contrastingly, in Figure 5.10 (b), the PFM loop rotates anti-clockwise in the case of PVDF, suggesting the negative sign of $d_{33,\text{eff}}$.

Interestingly, under the same conditions, the PFM phase loop measured in 20 nm thick La-HfO_2 samples demonstrate an anti-clockwise rotation similar to PVDF films and opposite to PZT, as shown in Figure 5.10 (c). This behavior of La:HfO_2 clearly suggests the negative sign of $d_{33,\text{eff}}$. Their measured value of $d_{33,\text{eff}}$ is between -2 pm V^{-1} and -5 pm V^{-1}, which is in reasonably good agreement with our theoretical values between -0.9 pm V^{-1} (in the

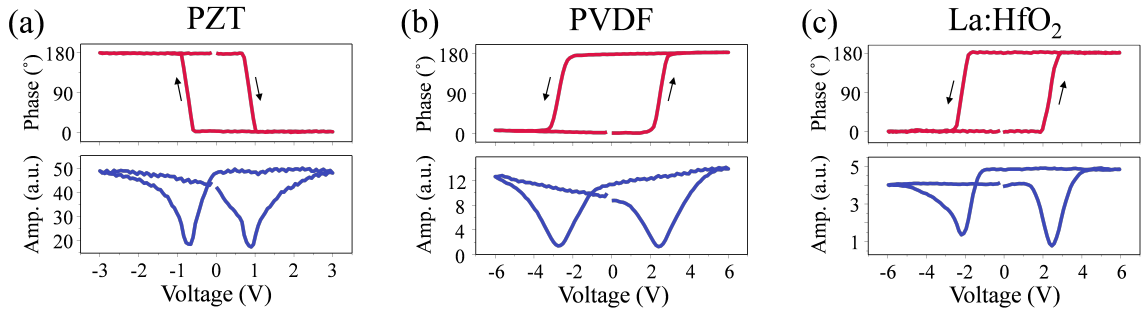

Figure 5.10: The results of dynamic measurements of piezoelectricity using piezoresponse force microscopy (PFM). Measured (top panel) PFM phase, and (bottom-panel) corresponding amplitude of (a) PZT, (b) PVDF, and (c) HfO_2.

polycrystalline limit) and -2.5 pm V^{-1} (for the single-crystal). The detailed information about the sample preparation and measurement techniques of this experimental study can be found in Ref.[164].

Hence, we have evidence of a positive longitudinal piezoresponse in the 10 nm Si-doped HfO_2 [162], 70 nm Y-doped HfO_2 [157], and 1 μm thick La-doped HfO_2[156] samples, whereas recent experimental study performed by the group of Alexei Gruverman has reported negative longitudinal piezoresponse in 20 nm thick La-HfO_2 samples. Thus, it seems that the piezoelectric properties of HfO_2 are sample dependent. A rigorous and systematic characterization is required to discover the factors driving the piezoresponse, as well as its sign.

5.7 Summary & Conclusions

In this chapter, we have provided a simple and conceivable explanation of the NLPE in HfO_2. We have performed a comparative study by taking $PbTiO_3$ as a reference with well-studied piezoelectric properties. We have shown that when the material is subjected to a vertical stretching along its polar direction, the O_I anions responsible for the development of the polarization move to preserve the suitable distance of the relevant Hf$-O_I$ bond. This movements of the O_I anions result in a reduction of polarization when the material is expanded along the polar axis, yielding an NLPE.

Based on this observation, we have identified a strategy to tune the longitudinal piezoresponse of HfO_2. By applying the epitaxial strain, we have achieved the controls of the chemical environment of the piezoelectrically active O_I atoms, which enhanced or reduced the magnitude of the e_{33}. Interestingly, by using this control knob, we could even reverse the sign of e_{33}. We admit that this strategy may not be applicable in practice since it involves a large compressive strain. However, the physical picture of our findings is clear. More importantly, to our best knowledge, such behavior had never been observed in any ferroelectrics where the sign of the e_{33} is switchable without switching the sign of the polarization.

In addition, we have compared our computed value of $d_{33,\text{eff}}$ for the polycrystalline HfO_2 sample with the experimental results obtained by the group of Alexei Gruverman. Our result is in reasonable good agreement with the experimental estimation. Notwithstanding, there is experimental evidence of positive longitudinal piezoelectric effect in HfO_2 samples present in the literature. Thus, it seems that the piezoelectric response in HfO_2 is sample-

dependent. An extensive experimental study is needed to know the factors (extrinsic vs intrinsic) controlling the piezoelectric response and its sign in this material.

Chapter 6

Engineering the piezoelectric response of HfO_2 by isovalent doping

In the previous chapter, we have learned about the piezoelectric properties of pure HfO_2. Next, this thesis has made an effort to improve the piezoelectric properties of pure HfO_2 by considering the isovalent chemical dopants, which replace the Hf atoms. We will discuss the results in this final chapter.

6.1 Motivation

PZT-based materials are the most widely used in piezoelectric device applications [21, 24]. Nevertheless, the thin-films of ZnO and AlN are recently used in bulk acoustic devices and MEMS applications due to their reasonable piezoelectric coupling [25–27, 31, 33, 34, 169].

In the search of novel piezoelectric materials, HfO_2 can be a promising candidate for its well-suited piezoelectric properties as well as CMOS compatibility, as already discussed in this thesis. Although the piezoelectric coefficient is relatively very small compared to PZT [164, 170], it can stand with AlN, ZnO-based thin films. Due to the large elastic constants, HfO_2 is very hard compared to PZT. Thus, it can show excellent mechanical quality.

Materials scientists have successfully modified the functioning of materials throughout the last century by chemical substitution (cation and anion) or alloying. Recently, it has been reported that the piezoelectric properties of AlN are enhanced more than two times of the pure system by Cr and Sc doping [171–173].

In this present work, we have tried to engineer the piezoelectric coefficient of HfO_2 by considering the isovalent dopants Si, Ge, Ti, Zr, and Pb. We will discuss our approach in the following sections.

6.2 The Model System

For the sake of simplicity, we consider tetravalent dopants Si, Ge, Ti, Zr, and Pb, which can replace Hf without any accompanying charge states or defects inside the lattice. In this study, we work with the 48-atom supercell of the usual FE-phase of HfO_2 as described in Chapter 4.

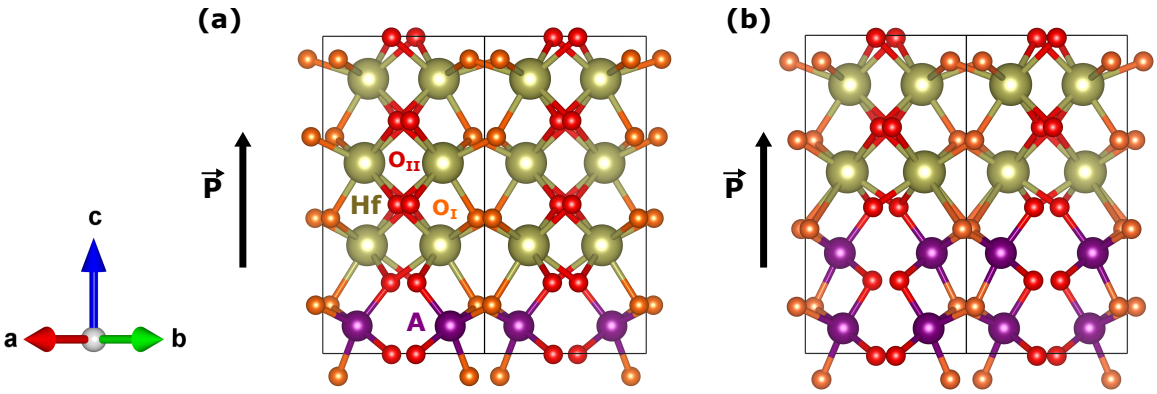

Figure 6.1: Considered dopant arrangements at (a) 25% and (b) 50% doping concentrations in 48-atom supercell, where A represents the dopants (in violet).

The 48-atom supercell allows us to consider various dopant arrangements at different concentrations in $Hf_{1-x}A_xO_2$ system, where A represents the dopant and x denotes the doping concentration level. However, we discovered that the FE state with a layer of small dopants perpendicular to the polar axis offers the lowest energy solution at all doping concentrations. In fact, with substantial Si doping, this layered FE-phase can be dominant over the m-phase (ground state phase) and t-phase of the material (discussed in detail in Chapter 4). These layered configurations of the dopants also can be expected from the way most of the HfO_2 films are grown (and doped) via the atomic layer deposition (ALD) technique. Thus, to explore the effect of dopants on the piezoelectric characteristics of HfO_2, we consider the layered structure perpendicular to the direction of polarization at 25% and 50% concentrations. Figure 6.1 shows the schematic of the model system considered in this work. Our cell size is compatible for considering the full layer of dopants only at 25% and 50% doping concentrations. We expect this "ordered doping" will yield results easier to analyze.

6.3 Results & Discussion

We start our first-principles calculations by relaxing the considered dopant configurations for each dopant at each concentration level. Then, we compute the piezoelectric tensors using DFPT for all the $Hf_{1-x}A_xO_2$ compounds, where A is the corresponding dopants (Si, Ge, Ti, Zr, and Pb) and x is the doping concentration level (25%, 50%).

The total piezoelectric coefficient $e^{\text{tot}}_{\alpha j}$ is decomposed of the purely electronic contribution ($\bar{e}_{\alpha j}$) and lattice-mediate part ($e^{\text{latt}}_{\alpha j}$) as follows (also discussed in Chapter2):

$$e^{\text{tot}}_{\alpha j} = \bar{e}_{\alpha j} + e^{\text{latt}}_{\alpha j} \tag{6.1}$$

where α represents the cartesian direction of polarization, and j is the strain in Voigt notation. Here we focus on the '33' component of the piezoelectric tensor. Figures 6.2 (a), (b), and (c) represent the evolution of $\bar{e}_{33}$, e^{latt}_{33}, and e^{tot}_{33}, respectively as a function of doping concentration for all the dopants. We note that $\bar{e}_{33}$ is always positive and nearly constant throughout the doping concentration range for all the dopants. Importantly, the lattice-mediated part presents a dopant-dependent behavior throughout the doping concentration range. At first glance, we notice two distinct behaviors exhibited by two different sorts

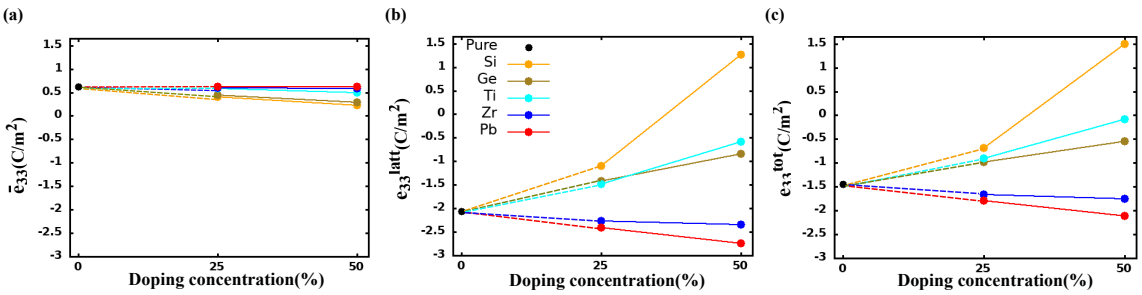

Figure 6.2: Computed piezoelectric coefficient e_{33} as a function of doping concentrations. (a) frozen-ion part ($\bar{e}_{33}$), (b) lattice-mediated part (e_{33}^{latt}), and (c) total piezoresponse (e_{33}^{tot}) of $Hf_{1-x}A_xO_2$ compound, where A denotes the dopant: Si (in orange), Ge (in cyan), Ti (in olive), Zr (in blue) and Pb (in red). The piezoreponse of the pure system is indicate by 0%.

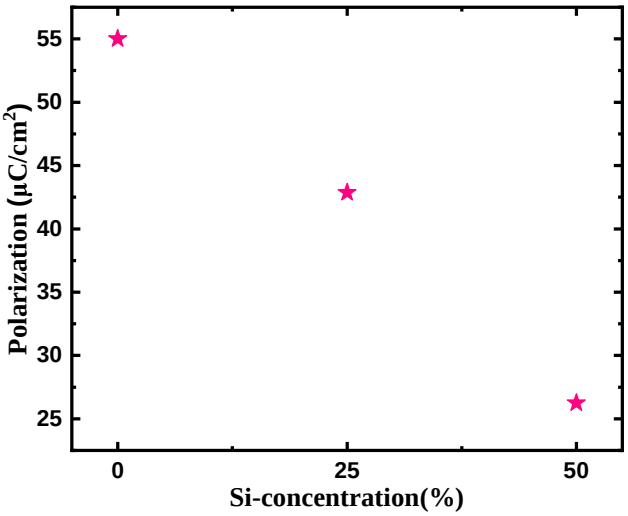

Figure 6.3: Computed polarization as a function of Si-concentration.

of dopants. The negative longitudinal effect of e_{33}^{latt} decreases for dopants smaller than Hf atoms, such as for Si, Ge, and Ti, whereas it increases for the big dopants Zr and Pb at both concentrations levels. The total piezoresponse also follows the same trend as e_{33}^{latt}.

Most interestingly, we find that the e_{33}^{latt} changes sign at 50% Si concentration. Figure 6.3 shows the evolution of polarization with increasing the Si concentration. We notice that the e_{33} changes sign even though the material remains in the same polar state (i.e., the polarization has the same sign throughout the doping concentration range). Switching signs of the e_{33} without switching the polarization is a very interesting feature that is unheard of in any ferroelectric perovskites. Note that, in Chapter 5, we have discussed such a situation where switching the sign of e_{33} is also possible by applying in-plane epitaxial compression.

Dopants	r	$\bar{e}_{33}$	e_{33}^{latt}	e_{33}^{tot}	a	b	c	P
Si	0.40	0.41	-1.10	-0.69	7.16	7.15	9.66	42
Ge	0.53	0.44	-1.42	-0.98	7.21	7.20	9.85	38
Ti	0.60	0.58	-1.48	-0.90	7.23	7.23	9.94	46
Pure	0.71	0.62	-2.06	-1.44	7.22	7.21	10.05	55
Zr	0.72	0.60	-2.27	-1.67	7.24	7.23	10.07	54
Pb	0.77	0.62	-2.41	-1.79	7.30	7.29	10.22	53

Table 6.1: Ionic radius r (Å), frozen-ion ($\bar{e}_{33}$), lattice-mediated (e_{33}^{latt}) and total (e_{33}^{tot}) response in (C/m^2), a (Å), b (Å), and c (Å) lattice parameter of the relaxed cell and Polarization P (μC/cm^2) of 25% doped systems. Data corresponding to the pure system is also present for comparison.

6.3.1 Correlation with ionic radius and lattice parameter

Here, we try to find some correlation between e_{33} and basic characteristics of the dopants, which could help us to understand the trend in e_{33}. Let us focus on the cases of 25% doping concentration.

Table 6.1 presents the ionic radius, decomposed piezoelectric coefficient $\bar{e}_{33}$, e_{33}^{latt}, and e_{33}^{tot}, the lattice parameters of the relaxed cell, and the calculated polarization for all the doped compounds. Interestingly, we find an overall correlation between the ionic radius and lattice-mediated part of the piezoresponse. The magnitude of the negative longitudinal piezoelectric effect in e_{33}^{latt} increases with increasing the ionic radius of the dopants. Additionally, we notice that the a, b, and c lattice parameters of all the systems follow the same trend. Thus, it indicates a size-dependent behavior of the dopants in the value of e_{33}. It is worth noting here that the relaxation of the $Hf_{1-x}A_xO_2$ cell results in a contraction in the c direction if the dopant is smaller than Hf, whereas it causes an expansion if the dopant is larger than Hf. Nonetheless, according to our estimated polarization values, all the compounds sustain the polarization with doping.

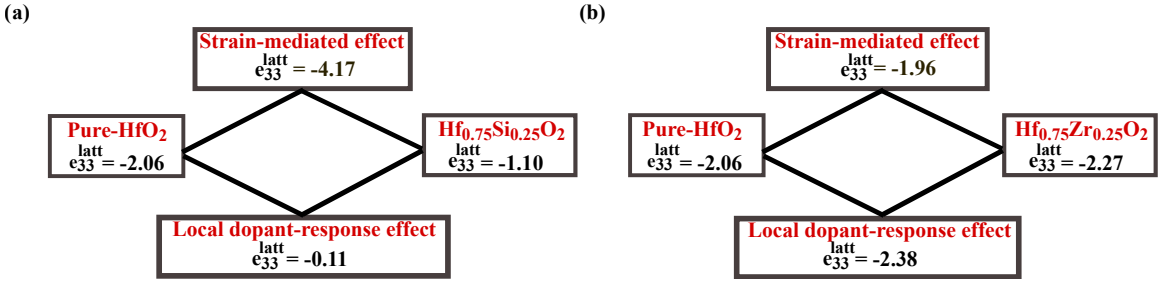

Figure 6.4: Schematic of the decomposed strain-mediated effect and the local dopant-response effect on e_{33}^{latt} in $Hf_{0.75}Si_{0.25}O_2$ and $Hf_{0.75}Zr_{0.5}O_2$ systems.

6.3.2 Strain-mediated effect vs local dopant-response effect

Having found two distinct behavior of the dopants, we choose two representative cases: Si among the small dopants and Zr among the large dopants, for further investigation. Let us note that the presence of the dopant imposes compressive or expansive strain in the HfO_2 lattice depending on the size of the dopants (see the value of lattice parameters of the doped

systems in Table 6.1). Thus, the changes in e_{33} may come from the strain in the unit-cell imposed by dopants or from the local response associated to dopants themselves.

To discriminate the strain-mediated effect from the particular response of the dopant atoms themselves (which we call "local dopant-response effect"), we have performed two different types of calculations. For the sake of the investigation, we focus on the 25% doping concentration level. At first, we consider $Hf_{0.75}A_{0.25}O_2$ system where A=Si/Zr inside the pure HfO_2 cell. Then we have fixed the lattice parameters to those of the pure HfO_2 cell and relaxed the atomic position of $Hf_{0.75}A_{0.25}O_2$ system. After that, we have calculated the piezoelectric coefficient e_{33} to see the local response of the dopants on it.

Next, we consider the pure HfO_2 system inside the relaxed $Hf_{0.75}A_{0.25}O_2$ cell. In this scenario, we've fixed the cell's lattice parameter to that of a $Hf_{0.75}A_{0.25}O_2$ cell and relaxed the atomic position of Hf and O atoms. The piezoelectric coefficient e_{33} is then calculated to see the effect of the strain imposed by the dopants.

Figures 6.4 (a) and (b) present the schematic of the decomposition of strain-mediated effect and local dopant-response effect on e_{33}^{latt} for $Hf_{0.75}Si_{0.25}O_2$ and $Hf_{0.75}Zr_{0.25}O_2$ systems, respectively. Here we focus on the e_{33}^{latt} since the lattice-mediated response is larger and mainly reflects the trend of the e_{33} with various dopants.

Let us now discuss the results for two different kinds of dopants systematically. We find that the value of e_{33}^{latt} in a relaxed cell of $Hf_{0.75}Si_{0.25}O_2$ is -1.10 C/m^2, which is closer to the value obtained by considering the local response of the dopants. Thus, the local dopant-response effect dominates over the strain-mediated effect on e_{33}^{latt} in $Hf_{0.75}Si_{0.25}O_2$.

On the other hand, we obtained the value of e_{33}^{latt} for the relaxed $Hf_{0.75}Zr_{0.25}O_2$ is -2.27 C/m^2. Both the values obtained by considering the strain-mediated effect and the local dopant response, in this case, are close to the relaxed cell value. However, the local response of the dopants dominates over the strain-mediated response. This suggests that the modest increase in e_{33}^{latt} in the relaxed $Hf_{0.75}Zr_{0.25}O_2$ cell compared to the pure HfO_2 system is caused by the local response of the dopants.

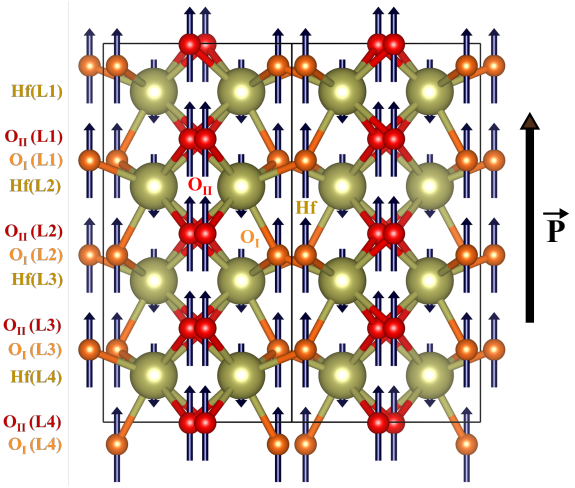

Figure 6.5: Schematic of the Λ_{33} component in pure HfO_2 with polarization pointing upward (denoted by black arrow). The arrows indicate the direction of force in a response of applied strain.The arrows do not reflect the magnitude of the forces. We mark the sub-lattices of each type of atoms in the figure for the sake of the explanation.

6.3.3 Physical insight

While the above discussion gives an understanding about the factor controlling the changes in e_{33} from the numerical point of view, the reason behind the different trend in e_{33} for different sizes of dopants can be further analyzed.

To understand the effect of dopants on e_{33}, we can track down the lattice-mediated part of the piezoresponse. We can write the $e_{\alpha j}^{\text{latt}}$ as (also presented in Chapter 2 and 5)

$$e_{\alpha j}^{latt} = \Omega_0 Z_{m\alpha} (\Phi^{-1})_{mn} \Lambda_{nj} \tag{6.2}$$

where Ω_0 is the volume of the unit-cell, Z is the Born effective charge, Φ is the force constant matrix, and Λ is the force response internal strain tensor. Here α denotes the Cartesian direction of the polarization, m and n are combined indices that run over all the atoms in the unit cell and the spatial directions of the displacement of each atom, j represents the direction of strain in Voigt notation.

In chapter 5, we have seen that the Λ_{33} component is the key in understanding the magnitude and sign of e_{33} in pure HfO_2. The Λ_{33} component quantifies the forces felt by atoms along z direction as a response to an applied strain along the same direction. Figure 6.5 shows the pictorial view of the Λ_{33} component for pure HfO_2 system in a 48-atom supercell. We notice that the strain-induced forces are negative in Hf atoms and positive in O_I and O_{II} atoms for all the sub-lattices marked in the Figure 6.5. The piezoelectrically active O_I atoms in all the sub-lattices move upward to preserve the vertical lying Hf$-O_I$ bond in an application of vertical stretching. These movements of the O_I atoms are opposite to the movements of the very same atoms while developing the polarization. Additionally, in all sub-lattices, downward forces on Hf atoms and upward forces on O_{II} atoms contribute to the lowering of polarization as a result of vertical stretching. This is consistent with getting a negative sign of e_{33} in pure HfO_2.

We will discuss our observations for the two representative doped cases in the following.

$\mathbf{Hf_{1-x}Si_xO_2}$

Let us start with the Λ_{33} component in $Hf_{1-x}Si_xO_2$ system. Figures 6.6 (a), (b) show the pictorial view of the Λ_{33} component at 25% and 50% Si concentrations, respectively. For the sake of explanation we divide the unit-cell into sub-lattices of each kind of atom as marked in Figures 6.6 (a) and (b). The forces on each sub-lattice contributes to either negative or positive value of e_{33}. Table 6.2 tabulates the contribution in e_{33} coming from the sub-lattice of each kind of atom.

At 25%, we notice that the first two sublattices (L1 & L2) of each atoms behave the same way as they do in the pure system, contributing to the negative e_{33} (see Table 6.2). However, the forces on the L3 & L4 sublattices of each kind of atom are opposite to the pure system (except for the O_I(L4)), which contribute to the positive e_{33}, as mentioned in Table 6.2. This behavior of the L3 & L4 atoms partly compensates the negative longitudinal effect in e_{33}. Hence, overall, this is consistent with the less negative e_{33} obtained at 25% Si concentration.

We notice that the forces on the O_I atoms at the interface feel the forces towards the Si atoms. Due to the shorter Si$-O_I$ (1.91 $\mathring{A}$) bond length compared to that of the Hf$-O_I$ bonds (2.17 $\mathring{A}$), the O_I atoms feel downward forces to maintain the suitable bond length with Si in an application of vertical stretching. This seems to be the main consequence of the Si doping, and the main mechanism by which it affects the response.

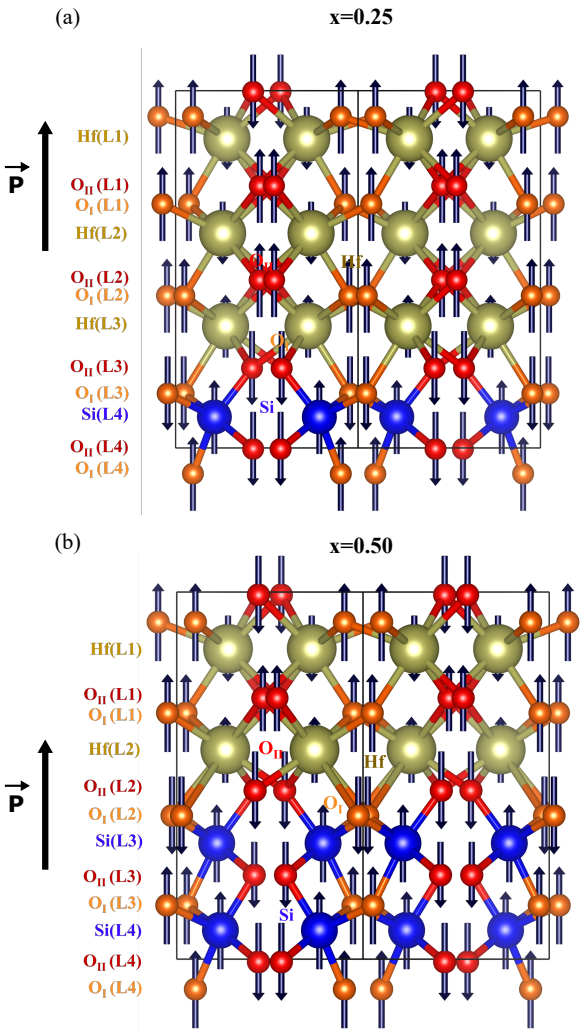

Figure 6.6: Schematic of the Λ_{33} component in $Hf_{1-x}Si_xO_2$ system with polarization pointing upward (denoted by the black arrow) at (a) 25%, and (b) 50% doping concentrations.The arrows indicate the direction of force in a response of applied strain. But they do not reflect the magnitude of the forces. We mark the sub-lattices of each type of atoms in the figure for the sake of the explanation.

Next, let us focus on the 50% case where we find the positive sign of e_{33} (see Figure 6.6(b) and Table 6.2).The first sub-lattice L1 exhibits the same behavior as the pure system, whereas the next three sub-lattices (L2, L3, and L4) tend to exhibit the opposed behavior. Note that O_I(L3) & O_I(L4) continue to behave like the pure system. Nevertheless, the contribution to the positive e_{33} dominates over the contribution to the negative e_{33}, which is consistent with getting a positive sign of e_{33} at 50% Si concentration.

The other small dopants, such as Ge and Ti, show similar behavior as of the $Hf_{1-x}Si_xO_2$ system. Although in these two cases e_{33} does not switch the sign, the magnitude is reduced with increasing the doping concentrations.

Sub-lattice	Pure	25%-Si	50%-Si	25%-Zr	50%-Zr
Hf(L1)	-	-	-	-	-
O_I(L1)	-	-	-	-	-
O_{II}(L1)	-	-	-	-	-
Hf(L2)	-	-	+	-	-
O_I(L2)	-	-	+	-	-
O_{II}(L2)	-	-	+	-	-
A(L3)	-	+	+	-	-
O_I(L3)	-	+	-	-	-
O_{II}(L3)	-	+	+	-	-
A(L4)	-	+	+	-	-
O_I(L4)	-	-	-	-	-
O_{II}(L4)	-	+	+	+	+

Table 6.2: The unit-cell of Pure, Si-doped HfO_2, and Zr-doped HfO_2 are decomposed into layers as shown in Figure 6.5, Figure 6.6, and Figure 6.7, respectively. We tabulate the contribution in e_{33} from each layer. A represents Hf/Si (Hf/Zr) depending on the doping concentration. The positive sign represents the contribution of the layer to positive e_{33}, and negative sign represents the contribution of the layer to negative e_{33}.

$\mathbf{Hf_{1-x}Zr_xO_2}$

In contrast, here we will discuss the enhancement of the negative longitudinal effect in e_{33} in the $Hf_{1-x}Zr_xO_2$ systems. Figures 6.7 (a) and (b) show the pictorial view of Λ_{33} component of $Hf_{1-x}Zr_xO_2$ system at 25% and 50% doping concentrations. Table 6.2 presents the contribution in positive or negative e_{33} coming from the sub-lattices of a particular kind of atom in the system. We notice that the $Hf_{1-x}Zr_xO_2$ follows the trend in pure HfO_2 system at both concentration levels, except for the O_{II}(L4) atoms where the direction of forces invert to the negative direction. Moreover, the magnitude of the forces on all the atoms is increased in these two cases compared to the pure system. Therefore, although the forces on the part of the O_{II} atoms contribute to a positive e_{33}, we get an overall enhancement of negative longitudinal effect in e_{33} with increasing the Zr concentration.

The $Hf_{1-x}Pb_xO_2$ follows the same trend as the Zr-doped system. We find that the value of e_{33} is enhanced at most 47% compared to the pure system by 50% of Pb doping.

6.4 Effect of isolated dopants

Finally, to further test the piezoelectric properties of doped HfO_2 in a less stable configuration, we calculate the e_{33} at 6.25% doping concentrations, where the dopant is isolated inside the lattice.

Figures 6.8 (a), (b), and (c) show the computed $\bar{e}_{33}$, e_{33}^{latt}, and e_{33}^{tot}, respectively for the isolated dopant configuration in $Hf_{1-x}A_xO_2$ compound, where x=0.0625. $\bar{e}_{33}$ remains a positive quantity for all the dopants. Interestingly, the e_{33}^{latt} part is always negative, and increases in magnitude, for all the dopants, and so does the e_{33}^{tot}. Surprisingly, we find that the magnitude of e_{33}^{tot} is highest for Si and lowest for Pb, which is exactly opposite of what we see in the layered configurations. These surprising results remain to be understood.

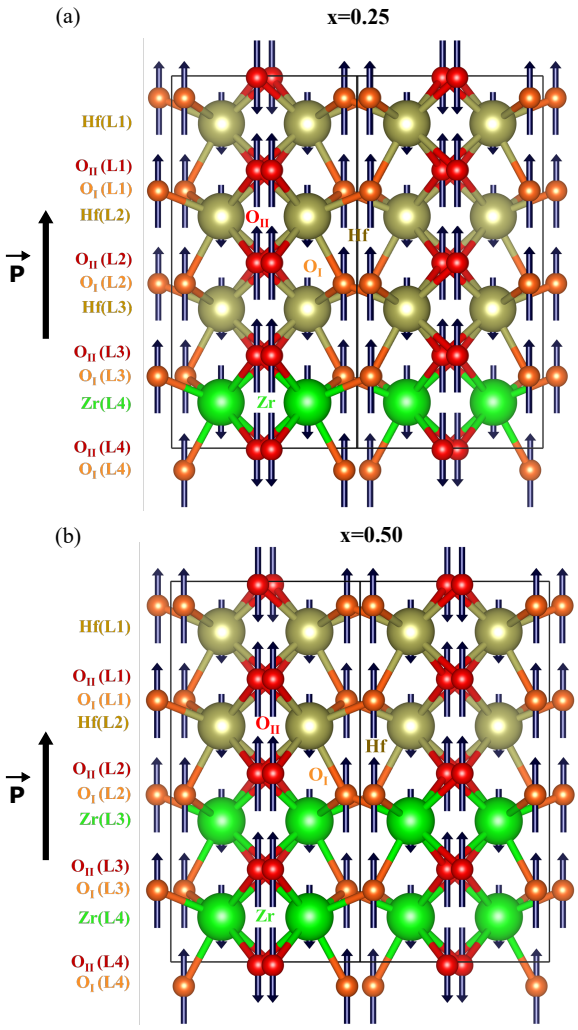

Figure 6.7: Schematic of the Λ_{33} component in $Hf_{1-x}Zr_xO_2$ system with polarization pointing upward (denoted by the black arrow) at (a) 25%, and (b) 50% doping concentrations.The arrows indicate the direction of force in a response of applied strain. But they do not reflect the magnitude of the forces. We mark the sub-lattices of each type of atoms in the figure for the sake of the explanation.

6.5 Conclusion

In this chapter, the dependence of the piezoelectric coefficient e_{33} on the isovalent dopants has been discussed. Our first-principles study predicted two distinct behavior of two different kinds of dopants for the configuration where dopant forming layer. The dopants smaller than Hf have lowered the negative effect in the value of e_{33}, whereas the dopants bigger than Hf have enhanced it. We find that the value of e_{33} is enhanced by 22% by Zr doping and 47% by Pb doping compared to the pure system. Conversely, we observe a situation where e_{33} switches sign at 50% Si doping. In Chapter 5, we have discussed that it is possible to switch the sign of e_{33} without switching the direction of polarization by applying in-plane epitaxial compression. Here we find another possible way to control the sign of the e_{33}.

This research is still ongoing, and we're working to better understand the dopant's

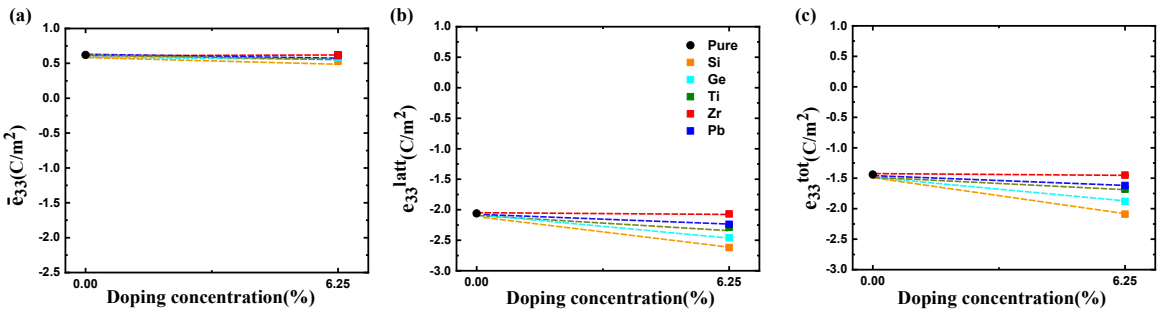

Figure 6.8: Computed piezoelectric coefficient e_{33} for isolated dopant configuration at 6.25% doping concentration. (a) frozen-ion part ($\bar{e}_{33}$), (b) lattice-mediated part (e_{33}^{latt}), and (c) total piezoresponse (e_{33}^{tot}) of $Hf_{1-x}A_xO_2$ compound, where A denotes the dopant: Si (in orange), Ge (in cyan), Ti (in olive), Zr (in blue) and Pb (in red). The piezoreponse of the pure system is indicate by 0%.

behavior in HfO_2 to come up with a simple and plausible explanation, particularly for the 50% Si-concentration where dopants change the sign of e_{33}. In addition, we are trying to understand the behavior of e_{33} in an isolated dopant configuration.

Nevertheless, this work has demonstrated the effect of isovalent dopants in the piezoelectric response of HfO_2. Additional studies can be done by considering other dopants as well as other possible modifications to tune the piezoelectric properties of HfO_2 to the point required for potential applications.

Chapter 7

Conclusions & Outlook

After the extensive investigation of ferroelectric random access memory for more than 60 years, it had been clear that the success or failure of ferroelectric memory depends on the choice and engineering of the ferroelectric material. The perovskite ferroelectrics have suffered from several issues including CMOS-incompatibility and scalability. Thus, the future development of memory technology had to rely on a material revolution. The emergence of ferroelectric HfO_2 in 2011 has generated tremendous attention due to the CMOS compatibility and the ability to retain the ferroelectricity in a few nanometer thicknesses. Consequently, the ferroelectricity in HfO_2 has become a general interest in both academic and industry communities. This thesis work started with the aim of understanding its piezoelectric response properties. However, our research efforts have developed through time.

The widely recognized ferroelectric orthorhombic phase of HfO_2 is believed to be metastable. Thus, understanding the origin of ferroelectricity in this material remained difficult. Many research works had focused on this issue by considering the role of the surface energy effects, chemical dopants, local strain, oxygen vacancies. Although the experimental reports suggested that dopant may facilitate the formation of the FE-phase of HfO_2, existing first-principles studies had reported that dopant alone is not sufficient to stabilize the FE-phase. In this thesis work, we have reconsidered the impact of dopants on the stability of the FE-phase. Surprisingly, we have noticed that some dopants have very strong preferences towards ordering inside the lattice: a fact that had been ignored by most of the first-principles studies in the literature. Most importantly, the ordering of the dopants impacts the stability of the ferroelectric phase of the material. We have predicted such a situation where the ferroelectric phase wins over the monoclinic phase (i.e. the usual ground state phase) and a competing paraelectric tetragonal phase with a full Si-layer perpendicular to the direction of polarization. The stability of the ferroelectric phase is mainly related to the size and the chemical environment of the comparatively small Si atoms. These findings are consistent with how most of the FE films of HfO_2 are grown using atomic layer deposition. Notwithstanding that our prediction is based on the ideal ferroelectric phase of HfO_2, the present study will change our perception of dopants inside the HfO_2 lattice and introduce a unique concept about how dopant ordering might help in the stabilization of the ferroelectric phase of HfO_2.

The discovery of lead-free and Si-technology compatible piezoelectrics has been increasingly important for the advancement of new technologies. In this context, the Si-compatible HfO_2 can be a promising candidate. However, the piezoelectric properties of HfO_2 have not

been extensively studied. Part of this thesis work has been focused on this domain. Recently it was revealed that HfO_2 presents a negative longitudinal piezoelectric effect, the origin of which was not clearly elucidated. Here, we have provided the physical insights behind the negative longitudinal piezoelectric effect in HfO_2. We have found that the piezoresponse of the material is controlled by the chemical environment of the piezoelectrically active oxygen atoms and its own way to maintain the suitable bond distance with the neighboring Hf atom as a response to applied strain. Most interestingly, we have predicted a way to control its magnitude and sign by applying epitaxial strain. To our best knowledge, switching the sign of the piezoelectric coefficient without switching the polarization is unheard of in any ferroelectrics prior. Since our prediction involved a large compressive strain, we admit that it may not be applicable in a practical situation. Nevertheless, our result is consistent with the physical explanation and suggests that HfO_2 may provide us with novel opportunities to tune its electromechanical response properties. It is worth mentioning here that there is experimental evidence of having a positive longitudinal piezoelectric coefficient as well as a negative longitudinal piezoelectric coefficient, depending on the FE sample of HfO_2. This finding reverberates with our prediction that the piezoresponse of HfO_2 can be switched without reversing its polarization state. Thus, the experimental question about the sign of the piezoelectric coefficient opens a new door for further research.

This thesis work has also engrossed in optimizing the piezoelectric response of HfO_2 by considering the isovalent chemical dopants Si, Ge, Pb, and Zr. We have predicted that the longitudinal piezoelectric coefficient of HfO_2 can be enhanced up to 47% compared to its pure system by doping with large isovalent atoms. On this note, further research in improving the piezoelectric coefficient in HfO_2 can be done considering other dopants. In addition, more possible ways (e.g. by applying the epitaxial strain) to optimize the piezoelectric coefficient of HfO_2 up to the point needed for applications can be investigated.

This work proves the importance of the dopant ordering in the phase stability and discusses the novel aspects of piezoelectricity in HfO_2. Thus, an interesting possible way forward would be to conduct similar research on other polar polymorphs of HfO_2 and ZrO_2, which are known to be important e.g. a recently reported rhombohedral phase that poses no wake-up effect and thus has great technological advantages [128, 129]. In the course of this thesis, we have studied the nature of ferroelectricity in this phase of HfO_2. However, the final outcomes of this investigation are not provided here due to a lack of time.

In sum, this thesis work has made some important discoveries regarding the way to stabilize the usual ferroelectric phase of HfO_2 on one hand. On the other hand, it has provided a detailed understanding of the piezoelectric properties of the material, which presents novel features unheard of among classic ferroelectric materials. This makes HfO_2 even more interesting and promising, and it has the potential to open new avenues for research both experimentally and theoretically. Thus, we believe that this work will contribute to the future development of this discipline.

Appendix A

List of publications

Published journal articles:

- Effect of Dopant Ordering on the Stability of Ferroelectric Hafnia
  S. Dutta, H. Aramberri, T.Schenk, and J.Íñiguez, Physica Status Solidi **14**, 2000047 (2020).

- Piezoelectricity in Hafnia
  S. Dutta, P. Buragohain, S. Glinsek, C. Richter, H. Aramberri, H. Lu, U. Schroeder, E. Defay, A. Gruverman, and J.Íñiguez, Nature Communications **12**, 7301 (2021)

- Wake-up Free Ferroelectric Rhombohedral Phase in Epitaxially Strained ZrO_2 Thin Films
  J.P.B. Silva, R.F. Negrea, M.C. Estrate, S. Dutta, H. Aramberri, J.Íñiguez, F.G. Figueiras, C. Ghica, K.C. Sekhar, and A.L. Kholkin, ACS Applied Materials & Interfaces **13**, 43 (2021)

In-preparation:

- Piezoelectric properties of Hafnia as a function of doping
  S. Dutta, N. Federova, and J.Íñiguez

Bibliography

[1]K. M. Rabe, K. M. Rabe, C. H. Ahn, and J.-M. Triscone, *Physics of ferroelectrics: a modern perspective*, 1st-Edition (Springer Publishing Company, Incorporated, 2007).

[2]R. D. King-Smith and D. Vanderbilt, "Theory of polarization of crystalline solids", Physical Review B **47**, 1651–1654 (1993).

[3]L. D. Landau, "On the theory of phase transitions", Zh. Eksp. Teor. Fiz. **7**, 19–32 (1937).

[4]L. D. Landau and E. M. Lifshitz, *Statistical physics* (Pergamon Press, Oxford, 1980).

[5]A. Montoya, A. Ocampo, and C. March, "Piezoelectric transducers and applications", in (Jan. 2008), pp. 289–306.

[6]J. Briscoe and S. Dunn, *Nanostructured piezoelectric energy harvesters* (Jan. 2014).

[7]J. F. Nye et al., *Physical properties of crystals: their representation by tensors and matrices* (Oxford university press, 1985).

[8]L. W. Martin and A. M. Rappe, "Thin-film ferroelectric materials and their applications", Nature Reviews Materials **2**, 1–15 (2016).

[9]H. Ishiwara, M. Okuyama, and Y. Arimoto, *Ferroelectric random access memories: fundamentals and applications*, Vol. 93 (Springer, 2004).

[10]J. Y. Kim, M.-J. Choi, and H. W. Jang, "Ferroelectric field effect transistors: progress and perspective", APL Materials **9**, 021102 (2021).

[11]M. Grundmann, *Physics of semiconductors*, Vol. 11 (Springer, 2010).

[12]E. Yurchuk, *Electrical characterisation of ferroelectric field effect transistors based on ferroelectric* HfO_2 *thin films*, Vol. 4 (Logos Verlag Berlin GmbH, 2015).

[13]H. J. Kim, M. H. Park, Y. J. Kim, Y. H. Lee, T. Moon, K. D. Kim, S. D. Hyun, and C. S. Hwang, "A study on the wake-up effect of ferroelectric $Hf_{0.5}Zr_{0.5}O_2$ films by pulse-switching measurement", Nanoscale **8**, 1383–1389 (2016).

[14]J. Meena, S. Sze, U. Chand, and T.-Y. Tseng, "Overview of emerging non-volatile memory technologies", Nanoscale Research Letters **9**, 1–33 (2014).

[15]Z. Fan, J. Chen, and J. Wang, "Ferroelectric HfO_2-based materials for next-generation ferroelectric memories", Journal of Advanced Dielectrics **06**, 1630003 (2016).

[16]J. Müller, P. Polakowski, S. Mueller, and T. Mikolajick, "Ferroelectric hafnium oxide based materials and devices: assessment of current status and future prospects", ECS Journal of Solid State Science and Technology **4**, N30–N35 (2015).

[17]R. J. Baker, CMOS C*ircuit* D*esign,* L*ayout, and* S*imulation*, 3rd (Wiley-IEEE Press, 2010).

[18]T. Ito, "Research and development of advanced CMOS technologies", Fujitsu Scientific & Technical Journal **39**, 3–8 (2003).

[19]T. S. Böscke, J. Müller, D. Bräuhaus, U. Schröder, and U. Böttger, "Ferroelectricity in hafnium oxide thin films", Applied Physics Letters **99**, 102903 (2011).

[20]M. T. Bohr, R. S. Chau, T. Ghani, and K. Mistry, "The high-k solution", IEEE Spectrum **44**, 29–35 (2007).

[21]A. M. Manjón-Sanz and M. R. Dolgos, "Applications of piezoelectrics: old and new", Chemistry of Materials **30**, 8718–8726 (2018).

[22]K. Uchino, "Introduction to Piezoelectric Actuators and Transducers", Report, International Center for Actuators and Transducers, Penn State University, 40 (2003).

[23]G. Kalimuldina, N. Turdakyn, I. Abay, A. Medeubayev, A. Nurpeissova, D. Adair, and Z. Bakenov, "A review of piezoelectric PVDF film by electrospinning and its applications", Sensors (Basel, Switzerland) **20**, 5214 (2020).

[24]M. Falkowski and A. Kersch, "Optimizing the piezoelectric strain in zro$_2$- and HfO$_2$-based incipient ferroelectrics for thin-film applications: an ab initio dopant screening study", ACS Applied Materials & Interfaces **12**, 32915–32924 (2020).

[25]H. Conrad, J. U. Schmidt, W. Pufe, F. Zimmer, T. Sandner, H. Schenk, and H. Lakner, "Aluminium nitride: a promising and full CMOS compatible piezoelectric material for MOEMS applications", Smart Sensors, Actuators, and MEMS IV **7362**, 165–174 (2009).

[26]P. Muralt, J. Conde, A. Artieda, F. Martin, and M. Cantoni, "Piezoelectric materials parameters for piezoelectric thin films in GHz applications", International Journal of Microwave and Wireless Technologies **1**, 19–27 (2009).

[27]S. Marauska, T. Dankwort, H. Quenzer, and B. Wagner, "Sputtered thin film piezoelectric aluminium nitride as a functional MEMS material and CMOS compatible process integration", Procedia Engineering **25**, EurosensorsXXV, 1341–1344 (2011).

[28]J. Zhao, J. Han, Y. Xing, W. Lin, L. Yu, X. Cao, Z. Wang, X. Zhou, X. Zhang, and B. Zhang, "Fabrication and application of flexible AlN piezoelectric film", Semiconductor Science and Technology **35**, 035009 (2020).

[29]M. Zhang, J. Yang, C. Si, G. Han, Y. Zhao, and J. Ning, "Research on the piezoelectric properties of AlN thin films for MEMS applications", Micromachines **6**, 1236–1248 (2015).

[30]K. Tonisch, V. Cimalla, C. Foerster, H. Romanus, O. Ambacher, and D. Dontsov, "Piezoelectric properties of polycrystalline AlN thin films for MEMS application", Sensors and Actuators A: Physical **132**, 658–663 (2006).

[31]L.-z. Kou, W.-l. Guo, and C. Li, "Piezoelectricity of ZnO and its nanostructures", in 2008 Symposium on Piezoelectricity, Acoustic Waves, and Device Applications (2008), pp. 354–359.

[32]F. J. von Preissig, H. Zeng, and E. Sok Kim, "Measurement of piezoelectric strength of ZnO thin films for MEMS applications", Smart Material Structures **7**, 396–403 (1998).

[33]A. Kuoni, R. l Holzherr, M. Boillat, and N. F. de Rooij, "Polyimide membrane with ZnO piezoelectric thin film pressure transducers as a differential pressure liquid flow sensor", Journal of Micromechanics and Microengineering **13**, S103–S107 (2003).

[34]J. Zhou, P. Fei, Y. Gao, Y. Gu, J. Liu, G. Bao, and Z. L. Wang, "Mechanical-electrical triggers and sensors using piezoelectric micowires/nanowires", Nano Letters **8**, 2725–2730 (2008).

[35]P. Polakowski and J. Müller, "Ferroelectricity in undoped hafnium oxide", Applied Physics Letters **106**, 232905 (2015).

[36]D. Martin, J. Müller, T. Schenk, T. M. Arruda, A. Kumar, E. Strelcov, E. Yurchuk, S. Müller, D. Pohl, U. Schröder, S. V. Kalinin, and T. Mikolajick, "Ferroelectricity in Si-doped HfO_2 revealed: a binary lead-free ferroelectric", Advanced Materials **26**, 8198–8202 (2014).

[37]T. S. Böscke, S. Teichert, D. Bräuhaus, J. Müller, U. Schröder, U. Böttger, and T. Mikolajick, "Phase transitions in ferroelectric silicon doped hafnium oxide", Applied Physics Letters **99**, 112904 (2011).

[38]T. D. Huan, V. Sharma, G. A. Rossetti, and R. Ramprasad, "Pathways towards ferroelectricity in hafnia", Physical Review B **90**, 064111 (2014).

[39]M. Pešić, U. Schroeder, and T. Mikolajick, "Chapter 10.1 - ferroelectric one transistor/one capacitor memory cell", Woodhead Publishing Series in Electronic and Optical Materials, edited by U. Schroeder, C. S. Hwang, and H. Funakubo, 413–424 (2019).

[40]S. Mueller, "Ferroelectric HfO_2 and its impact on the memory landscape", in 2018 IEEE international memory workshop (IMW) (2018), pp. 1–4.

[41]M. H. Park, Y. H. Lee, T. Mikolajick, U. Schroeder, and C. S. Hwang, "Review and perspective on ferroelectric HfO_2-based thin films for memory applications", MRS Communications **8**, 795–808 (2018).

[42]X. Zhang, M. Takahashi, K. Takeuchi, and S. Sakai, "64 kbit ferroelectric-gate-transistor-integrated NAND flash memory with 7.5 V program and long data retention", Japanese Journal of Applied Physics **51**, 04DD01 (2012).

[43]J. Celinska, V. Joshi, S. Narayan, L. McMillan, and C. Paz de Araujo, "Effects of scaling the film thickness on the ferroelectric properties of $SrBi_2Ta_2O_9$ ultra thin films", Applied Physics Letters **82**, 3937–3939 (2003).

[44]T. Mikolajick, C. Dehm, W. Hartner, I. Kasko, M. Kastner, N. Nagel, M. Moert, and C. Mazure, "FeRAM technology for high density applications", Microelectronics Reliability **41**, 947–950 (2001).

[45]D. Jung, B. Jeon, H. Kim, Y. Song, B. Koo, S. Lee, S. Park, Y. Park, and K. Kim, "Highly manufacturable 1T1C 4 Mb FRAM with novel sensing scheme", in International Electron Devices Meeting 1999. Technical Digest (1999), pp. 279–282.

[46]J. Muller, T. S. Boscke, S. Muller, E. Yurchuk, P. Polakowski, J. Paul, D. Martin, T. Schenk, K. Khullar, A. Kersch, W. Weinreich, S. Riedel, K. Seidel, A. Kumar, T. M. Arruda, S. V. Kalinin, T. Schlosser, R. Boschke, R. van Bentum, U. Schroder, and T. Mikolajick, "Ferroelectric hafnium oxide: a CMOS-compatible and highly scalable approach to future ferroelectric memories", 2013 IEEE International Electron Devices Meeting, 10.8.1–10.8.4 (2013).

[47]J. Muller, E. Yurchuk, T. Schlosser, J. Paul, R. Hoffmann, S. Muller, D. Martin, S. Slesazeck, P. Polakowski, J. Sundqvist, M. Czernohorsky, K. Seidel, P. Kucher, R. Boschke, M. Trentzsch, K. Gebauer, U. Schroder, and T. Mikolajick, "Ferroelectricity in HfO_2 enables nonvolatile data storage in 28 nm HKMG", 2012 Symposium on VLSI Technology (VLSIT), 25–26 (2012).

[48]P. Polakowski, S. Riedel, W. Weinreich, M. Rudolf, J. Sundqvist, K. Seidel, and J. Muller, "Ferroelectric deep trench capacitors based on al:hfo2 for 3d nonvolatile memory applications", 2014 IEEE 6th International Memory Workshop (IMW), 1–4 (2014).

[49]M. H. Park, H. J. Kim, Y. J. Kim, W. Lee, T. Moon, and C. Hwang, "Evolution of phases and ferroelectric properties of thin $Hf_{0.5}Zr_{0.5}O_2$ films according to the thickness and annealing temperature", Applied Physics Letters **102** (2013).

[50]D. Zhou, J. Xu, Q. Li, Y. Guan, F. Cao, X. Dong, J. Müller, T. Schenk, and U. Schröder, "Wake-up effects in Si-doped hafnium oxide ferroelectric thin films", Applied Physics Letters **103** (2013).

[51]T. Schenk, U. Schroeder, M. Pešić, M. Popovici, Y. V. Pershin, and T. Mikolajick, "Electric field cycling behavior of ferroelectric hafnium oxide", ACS Applied Materials & Interfaces **6**, 19744–19751 (2014).

[52]M. Pešić, F. P. G. Fengler, L. Larcher, A. Padovani, T. Schenk, E. D. Grimley, X. Sang, J. M. LeBeau, S. Slesazeck, U. Schroeder, and T. Mikolajick, "Physical mechanisms behind the field-cycling behavior of HfO_2-based ferroelectric capacitors", Advanced Functional Materials **26**, 4601–4612 (2016).

[53]F. P. G. Fengler, M. Hoffmann, S. Slesazeck, T. Mikolajick, and U. Schroeder, "On the relationship between field cycling and imprint in ferroelectric $Hf_{0.5}Zr_{0.5}O_2$", Journal of Applied Physics **123**, 204101 (2018).

[54]P. D. Lomenzo, Q. Takmeel, C. Zhou, C. M. Fancher, E. Lambers, N. G. Rudawski, J. L. Jones, S. Moghaddam, and T. Nishida, "TaN interface properties and electric field cycling effects on ferroelectric Si-doped HfO_2 thin films", Journal of Applied Physics **117**, 134105 (2015).

[55]M. H. Park, H. J. Kim, Y. J. Kim, Y. H. Lee, T. Moon, K. D. Kim, S. D. Hyun, F. Fengler, U. Schroeder, and C. S. Hwang, "Effect of Zr content on the wake-up effect in $Hf_{1-x}Zr_xO_2$ films", ACS Applied Materials & Interfaces **8**, 15466–15475 (2016).

[56]C. Richter, T. Schenk, M. H. Park, F. A. Tscharntke, E. D. Grimley, J. M. LeBeau, C. Zhou, C. M. Fancher, J. L. Jones, T. Mikolajick, and U. Schroeder, "Si Doped Hafnium Oxide| A "Fragile" ferroelectric system", Advanced Electronic Materials **3**, 1–12 (2017).

[57]U. Schroeder, C. Richter, M. H. Park, T. Schenk, M. Pešić, M. Hoffmann, F. P. G. Fengler, D. Pohl, B. Rellinghaus, C. Zhou, C.-C. Chung, J. L. Jones, and T. Mikolajick, "Lanthanum-doped hafnium oxide: a robust ferroelectric material", Inorganic Chemistry **57**, 2752–2765 (2018).

[58]M. Hoffmann, U. Schroeder, T. Schenk, T. Shimizu, H. Funakubo, O. Sakata, D. Pohl, M. Drescher, C. Adelmann, R. Materlik, A. Kersch, and T. Mikolajick, "Stabilizing the ferroelectric phase in doped hafnium oxide", Journal of Applied Physics **118**, 072006 (2015).

[59]A. G. Chernikova, M. G. Kozodaev, D. V. Negrov, E. V. Korostylev, M. H. Park, U. Schroeder, C. S. Hwang, and A. M. Markeev, "Improved ferroelectric switching endurance of La-doped $Hf_{0.5}Zr_{0.5}O_2$ thin films", ACS Applied Materials & Interfaces **10**, 2701–2708 (2018).

[60]M. H. Park, Y. H. Lee, H. J. Kim, Y. J. Kim, T. Moon, K. D. Kim, J. Müller, A. Kersch, U. Schroeder, T. Mikolajick, and C. S. Hwang, "Ferroelectricity and antiferroelectricity of doped thin HfO_2-based films", Advanced Materials **27**, 1811–1831 (2015).

[61]S. Clima, D. J. Wouters, C. Adelmann, T. Schenk, U. Schroeder, M. Jurczak, and G. Pourtois, "Identification of the ferroelectric switching process and dopant-dependent switching properties in orthorhombic HfO_2: a first principles insight", Applied Physics Letters **104**, 092906 (2014).

[62]U. Schroeder, E. Yurchuk, J. Müller, D. Martin, T. Schenk, P. Polakowski, C. Adelmann, M. I. Popovici, S. V. Kalinin, and T. Mikolajick, "Impact of different dopants on the switching properties of ferroelectric hafniumoxide", Japanese Journal of Applied Physics **53**, 08LE02 (2014).

[63]S. Migita, H. Ota, H. Yamada, A. Sawa, and A. Toriumi, "Thickness-independent behavior of coercive field in HfO_2-based ferroelectrics", in 2017 IEEE Electron Devices Technology and Manufacturing Conference (EDTM) (2017), pp. 255–256.

[64]K. D. Kim, Y. H. Lee, T. Gwon, Y. J. Kim, H. J. Kim, T. Moon, S. D. Hyun, H. W. Park, M. H. Park, and C. S. Hwang, "Scale-up and optimization of $HfO_2 - ZrO_2$ solid solution thin films for the electrostatic supercapacitors", Nano Energy **39**, 390–399 (2017).

[65]Y. Yun, P. Buragohain, M. Li, Z. Ahmadi, Y. Zhang, X. Li, H. Wang, L. Tao, H. Wang, J. E. Shield, et al., "Intrinsic ferroelectricity in y-doped HfO_2 thin films", arXiv preprint arXiv:2109.05071 (2021).

[66]M. H. Park, Y. H. Lee, H. J. Kim, T. Schenk, W. Lee, K. D. Kim, F. P. Fengler, T. Mikolajick, U. Schroeder, and C. S. Hwang, "Surface and grain boundary energy as the key enabler of ferroelectricity in nanoscale hafnia-zirconia: A comparison of model and experiment", Nanoscale **9**, 9973–9986 (2017).

[67]T. Shiraishi, K. Katayama, T. Yokouchi, T. Shimizu, T. Oikawa, O. Sakata, H. Uchida, Y. Imai, T. Kiguchi, T. J. Konno, and H. Funakubo, "Impact of mechanical stress on ferroelectricity in ($Hf_{0.5}Zr_{0.5}O_2$) thin films", Applied Physics Letters **108** (2016).

[68]R. Batra, T. D. Huan, J. L. Jones, G. Rossetti, and R. Ramprasad, "Factors favoring ferroelectricity in hafnia: a first-principles computational study", The Journal of Physical Chemistry C **121**, 4139–4145 (2017).

[69]Y. Zhou, Y. K. Zhang, Q. Yang, J. Jiang, P. Fan, M. Liao, and Y. C. Zhou, "The e ff ects of oxygen vacancies on ferroelectric phase transition of HfO_2 - based thin film from first-principle", **167**, 143–150 (2019).

[70]T. Shimizu, T. Yokouchi, T. Oikawa, T. Shiraishi, T. Kiguchi, A. Akama, T. J. Konno, A. Gruverman, and H. Funakubo, "Contribution of oxygen vacancies to the ferroelectric behavior of $Hf_{0.5}Zr_{0.5}O_2$ thin films", Applied Physics Letters **106**, 112904 (2015).

[71]J. Müller, U. Schroeder, T. Böscke, I. Mueller, U. Boettger, L. Wilde, J. Sundqvist, M. Lemberger, P. Kuecher, T. Mikolajick, and L. Frey, "Ferroelectricity in yttrium-doped hafnium oxide", Journal of Applied Physics **110**, 114113–114113 (2011).

[72]J. Müller, T. S. Böscke, U. Schröder, S. Mueller, D. Bräuhaus, U. Böttger, L. Frey, and T. Mikolajick, "Ferroelectricity in simple binary ZrO_2 and HfO_2", Nano Letters **12**, 4318–4323 (2012).

[73]S. Mueller, J. Mueller, A. Singh, S. Riedel, J. Sundqvist, U. Schroeder, and T. Mikolajick, "Incipient ferroelectricity in Al-doped HfO_2 thin films", Advanced Functional Materials **22**, 2412–2417 (2012).

[74]R. Materlik, C. Künneth, M. Falkowski, T. Mikolajick, and A. Kersch, "Al-, Y-, and La-doping effects favoring intrinsic and field induced ferroelectricity in HfO2: A first principles study", Journal of Applied Physics **123** (2018).

[75]C. Künneth, R. Materlik, M. Falkowski, and A. Kersch, "Impact of four-valent doping on the crystallographic phase formation for ferroelectric HfO_2 from first-principles: implications for ferroelectric memory and energy-related applications", ACS Applied Nano Materials **1**, 254–264 (2018).

[76]R. Materlik, C. Künneth, T. Mikolajick, and A. Kersch, "The impact of charge compensated and uncompensated strontium defects on the stabilization of the ferroelectric phase in HfO_2", Applied Physics Letters **111**, 082902 (2017).

[77]M. Falkowski, C. Künneth, R. Materlik, and A. Kersch, "Unexpectedly large energy variations from dopant interactions in ferroelectric HfO_2 from high-throughput ab initio calculations", npj Computational Materials **4**, 73 (2018).

[78]M. Dogan, N. Gong, T.-P. Ma, and S. Ismail-Beigi, "Causes of ferroelectricity in HfO_2-based thin films: an ab initio perspective", Phys. Chem. Chem. Phys. **21**, 12150–12162 (2019).

[79]X. Xu, F.-T. Huang, Y. Qi, S. Singh, K. M. Rabe, D. Obeysekera, J. Yang, M.-W. Chu, and S.-W. Cheong, "Kinetically stabilized ferroelectricity in bulk single-crystalline $HfO_2 : Y$", Nature Materials **20**, 826–832 (2021).

[80]T. Mimura, T. Shimizu, and H. Funakubo, "Ferroelectricity in $YO_{1.5} - HfO_2$ films around 1m in thickness", Applied Physics Letters **115**, 032901 (2019).

[81]J. Bouaziz, P. Rojo Romeo, N. Baboux, and B. Vilquin, "Imprint issue during retention tests for HfO_2-based FRAM: an industrial challenge?", Applied Physics Letters **118**, 082901 (2021).

[82]P. Buragohain, A. Erickson, P. Kariuki, T. Mittmann, C. Richter, P. D. Lomenzo, H. Lu, T. Schenk, T. Mikolajick, U. Schroeder, and A. Gruverman, "Fluid imprint and inertial switching in ferroelectric $La : HfO_2$ capacitors", ACS Applied Materials & Interfaces **11**, 35115–35121 (2019).

[83]H. Wei, H. Wang, Y. Xia, D. Cui, Y. Shi, M. Dong, C. Liu, T. Ding, J. Zhang, Y. Ma, N. Wang, Z. Wang, Y. Sun, R. Wei, and Z. Guo, "An overview of lead-free piezoelectric materials and devices", J. Mater. Chem. C **6**, 12446–12467 (2018).

[84]M. Falkowski and A. Kersch, "Optimizing the piezoelectric strain in ZrO_2 and HfO_2-based incipient ferroelectrics for thin-film applications: an ab initio dopant screening study", ACS Applied Materials & Interfaces **12**, 32915–32924 (2020).

[85]X. Wu, D. Vanderbilt, and D. R. Hamann, "Systematic treatment of displacements, strains, and electric fields in density-functional perturbation theory", Physical Review B - Condensed Matter and Materials Physics **72**, 1–13 (2005).

[86]X. Gonze, "Perturbation expansion of variational principles at arbitrary order", Physical Review A **52**, 1086–1095 (1995).

[87]X. Gonze, "First-principles responses of solids to atomic displacements and homogeneous electric fields: Implementation of a conjugate-gradient algorithm", Physical Review B - Condensed Matter and Materials Physics **55**, 10337–10354 (1997).

[88]D. R. Hamann, X. Wu, K. M. Rabe, and D. Vanderbilt, "Metric tensor formulation of strain in density-functional perturbation theory", Physical Review B - Condensed Matter and Materials Physics **71** (2005).

[89]M. Gajdoš, K. Hummer, G. Kresse, J. Furthmüller, and F. Bechstedt, "Linear optical properties in the projector-augmented wave methodology", Physical Review B - Condensed Matter and Materials Physics **73**, 1–9 (2006).

[90]S. Baroni and R. Resta, "Ab initio calculation of the macroscopic dielectric constant in silicon", Physical Review B **33**, 7017–7021 (1986).

[91]M. Born and R. Oppenheimer, "Zur Quantentheorie der Molekeln", Annalen der Physik **389**, 457–484 (1927).

[92]P. Hohenberg and W. Kohn, "Inhomogeneous electron gas", Physical Review **136**, B864–B871 (1964).

[93]D. M. Ceperley and B. J. Alder, "Ground state of the electron gas by a stochastic method", Physical Review Letters **45**, 566–569 (1980).

[94]J. P. Perdew, K. Burke, and M. Ernzerhof, "Generalized gradient approximation made simple", Physical Review Letters **77**, 3865–3868 (1996).

[95]J. P. Perdew and W. Yue, "Accurate and simple density functional for the electronic exchange energy: Generalized gradient approximation", Physical Review B **33**, 12–14 (1986).

[96]C. Lee, W. Yang, and R. G. Parr, "Development of the Colle-Salvetti correlation-energy formula into a functional of the electron density", Physical Review B **37**, 785–789 (1988).

[97]A. D. Becke, "Density-fnnctional exchange-energy approximation with correct asymptotic behavior", Physical Review **38**, 3098–3100 (1988).

[98]J. P. Perdew, A. Ruzsinszky, G. I. Csonka, O. A. Vydrov, G. E. Scuseria, L. A. Constantin, X. Zhou, and K. Burke, "Restoring the density-gradient expansion for exchange in solids and surfaces", Physical Review Letters **100**, 1–4 (2008).

[99]N. W. Ashcroft and N. D. Mermin, *Solid State Physics* (Holt-Saunders, 1976).

[100]M. C. Payne, M. P. Teter, D. C. Allan, T. A. Arias, and J. D. Joannopoulos, "Iterative minimization techniques for ab initio total-energy calculations: molecular dynamics and conjugate gradients", Rev. Mod. Phys. **64**, 1045–1097 (1992).

[101]H. J. Monkhorst and J. D. Pack, "Special points for Brillouin-zone integrations", Physical Review B **13**, 5188–5192 (1976).

[102]N. Troullier and J. L. Martins, "Efficient pseudopotentials for plane-wave calculations", Physical Review B **43**, 1993–2006 (1991).

[103]D. R. Hamann, M. Schlüter, and C. Chiang, "Norm-conserving pseudopotentials", Physical Review Letters **43**, 1494–1497 (1979).

[104]D. Vanderbilt, "Optimally smooth norm-conserving pseudopotentials", Physical Review B **32**, 336–339 (1985).

[105]D. Vanderbilt, "Soft self-consistent pseudopotentials in a generalized eigenvalue formalism", Physical Review B **41**, 7892–7895 (1990).

[106]P. E. Blöchl, "Projector augmented-wave method", Physical Review B **50**, 17953–17979 (1994).

[107]G. Kresse and J. Hafner, "Ab initio molecular dynamics for open-shell transition metals", Physical Review B **48**, 13115–13118 (1993).

[108]G. Kresse and J. Furthmüller, "Efficiency of ab-initio total energy calculations for metals and semiconductors using a plane-wave basis set", Computational Materials Science **6**, 15–50 (1996).

[109]R. Materlik, C. Kunneth, and A. Kersch, "The origin of ferroelectricity in $Hf_{1-x}Zr_xO_2$: A computational investigation and a surface energy model", Journal of Applied Physics **117** (2015).

[110]Y. Qi, S. Singh, C. Lau, F.-t. Huang, X. Xu, F. J. Walker, C. H. Ahn, S.-w. Cheong, and K. M. Rabe, "Stabilization of competing ferroelectric phases of HfO_2 under epitaxial strain", Physical Review Letters **125**, 257603 (2020).

[111]A. Raeliarijaona and R. E. Cohen, "Origin of ferroelectricity in hafnia from epitaxial strain", in (2021).

[112]T. Schenk, C. M. Fancher, M. H. Park, C. Richter, C. Künneth, A. Kersch, J. L. Jones, T. Mikolajick, and U. Schroeder, "On the Origin of the Large Remanent Polarization in La:HfO_2", Advanced Electronic Materials **5**, 1–9 (2019).

[113]C. Wang, M. Zinkevich, and F. Aldinger, "The zirconia–hafnia system: DTA measurements and thermodynamic calculations", Journal of the American Ceramic Society **3758**, 3751–3758 (2006).

[114]H. Zhu, C. Tang, L. R. C. Fonseca, and R. Ramprasad, "Recent progress in ab initio simulations of hafnia-based gate stacks", Journal of Material Science, 7399–7416 (2012).

[115]L.-g. Liu and L.-g. Liu, "New high pressure phases of ZrO_2 and HfO_2", Journal of Physics and Chemistry of Solids **41**, 2–5 (1980).

[116]J. M. Leger, P. E. Tomaszewski, L. D. P.-c. Materiaux, and A. Briand, "Pressure-induced phase transitions and volume changes in HfO_2 up to 50 GPa", Physics and Chemistry of Minerals **47**, 75–83 (1993).

[117]M. Yoshimura, "Phase stability of zirconia", American Ceramic Society Bulletin **67**, 1950–1955 (1988).

[118]R. Terki, G. Bertrand, H. Aourag, and C. Coddet, "Structural and electronic properties of zirconia phases : A FP-LAPW investigations", Materials Science in Semiconductor Processing **9**, 1006–1013 (2006).

[119]G. Teufer, "The crystal structure of tetragonal ZrO_2", Acta Crystallographica **15**, 1187–1187 (1962).

[120]R. Ruh and P. W. R. Corfield, "Crystal structure of monoclinic hafnia and comparison with monoclinic zirconia", Journal of the American Ceramic Society **53**, 126–129 (1970).

[121]J. E. Jaffe, R. A. Bachorz, and M. Gutowski, "Low-temperature polymorphs of ZrO_2 and HfO_2: A density-functional theory study", Physical Review B - Condensed Matter and Materials Physics **72**, 1–9 (2005).

[122]O. Ohtaka, T. Yamanaka, and S. Kume, "Synthesis and X-ray structural analysis by the rietveld method of orthorhombic hafnia", Journal of the Ceramic Society of Japan **99**, 826–827 (1991).

[123]J. Kang, E.-C. Lee, and K. J. Chang, "First-principles study of the structural phase transformation of hafnia under pressure", Physical Review B **68**, 054106 (2003).

[124]Y. Kudoh, H. Takeda, and H. Arashi, "In situ determination of crystal structure for high pressure phase of ZrO_2 using a diamond anvil and single crystal x-ray diffraction method", Physics and Chemistry of Minerals **13**, 233–237 (1986).

[125]J. Müller, T. S. Böscke, D. Bräuhaus, U. Schröder, U. Böttger, J. Sundqvist, P. Kücher, T. Mikolajick, and L. Frey, "Ferroelectric $Zr_{0.5}Hf_{0.5}O_2$ thin films for nonvolatile memory applications", Applied Physics Letters **99**, 112901 (2011).

[126]B.-t. Lin, Y.-w. Lu, J. Shieh, and M.-j. Chen, "Induction of ferroelectricity in nanoscale ZrO2 thin films on Pt electrode without post-annealing", Journal of the European Ceramic Society, 2–6 (2016).

[127]S. V. Barabash, "Prediction of new metastable HfO_2 phases: toward understanding ferro- and antiferroelectric films", Journal of Computational Electronics **16**, 1227–1235 (2017).

[128]Y. Wei, P. Nukala, M. Salverda, S. Matzen, H. J. Zhao, J. Momand, A. S. Everhardt, G. Agnus, G. R. Blake, P. Lecoeur, B. J. Kooi, J. Íñiguez, B. Dkhil, and B. Noheda, "A rhombohedral ferroelectric phase in epitaxially strained $Hf_{0.5}Zr_{0.5}O_2$ thin films", Nature Materials **17**, 1095–1100 (2018).

[129]J. P. B. Silva, R. F. Negrea, M. C. Istrate, S. Dutta, H. Aramberri, J. Íñiguez, F. G. Figueiras, C. Ghica, K. C. Sekhar, and A. L. Kholkin, "Wake-up free ferroelectric rhombohedral phase in epitaxially strained ZrO_2 thin films", ACS Applied Materials & Interfaces **13**, PMID: 34694130, 51383–51392 (2021).

[130]A. Kersch and M. Falkowski, "New Low-energy crystal structures in ZrO_2 and HfO_2", physica status solidi (RRL) – Rapid Research Letters **2100074**, 10–13 (2021).

[131]R. Materlik, "Stabilization of ferroelectricity in hafnia, zirconia and their mixtures by dopants and interface energy first principles calculations and a phenomenological model", Bibliographic information available from INIS: http://inis.iaea.org/search/search.aspx?orig_q=RN:5200799 Available from: https://tud.qucosa.de/api/qucosa%3A36171/attachment/ATT-0/, PhD thesis (Jul 2019).

[132]I. A. El-Shanshoury, V. A. Rudenko, and I. A. Ibrahim, "Polymorphic behavior of thin evaporated films of zirconium and hafnium oxides", J Amer Ceram Soc, 264–268 (May 1970).

[133]I. MacLaren, T. Ras, M. MacKenzie, A. J. Craven, D. W. McComb, and S. D. Gendt, "Texture, twinning, and metastable "tetragonal" phase in ultrathin films of HfO_2 on a si substrate", Journal of The Electrochemical Society **156**, G103 (2009).

[134]X. Zhao and D. Vanderbilt, "First-principles study of structural, vibrational, and lattice dielectric properties of hafnium oxide", Physical Review B **65**, 233106 (2002).

[135]X. Zhao and D. Vanderbilt, "Phonons and lattice dielectric properties of zirconia", Physical Review B **65**, 075105 (2002).

[136]X. Zhao and D. Vanderbilt, "First-principles study of structural, vibrational and lattice dielectric properties of hafnium oxide", Physical Review B **65**, 233106 (2002).

[137]D. Fischer and A. Kersch, "The effect of dopants on the dielectric constant of hfo2 and zro2 from first principles", Applied Physics Letters **92**, 012908 (2008).

[138]G.-M. Rignanese, X. Gonze, G. Jun, K. Cho, and A. Pasquarello, "First-principles investigation of high-κ dielectrics: comparison between the silicates and oxides of hafnium and zirconium", Physical Review B **69**, 184301 (2004).

[139]G. D. Wilk, R. M. Wallace, and J. M. Anthony, "Hafnium and zirconium silicates for advanced gate dielectrics", **484** (2003).

[140]E. Yurchuk, J. Müller, S. Knebel, J. Sundqvist, A. P. Graham, T. Melde, U. Schröder, and T. Mikolajick, "Impact of layer thickness on the ferroelectric behaviour of silicon doped hafnium oxide thin films", Thin Solid Films **533**, EMRS 2012 Symposium L, 88–92 (2013).

[141]E. D. Grimley, T. Schenk, T. Mikolajick, U. Schroeder, and J. M. LeBeau, "Atomic structure of domain and interphase boundaries in ferroelectric HfO_2", Advanced Materials Interfaces **5**, 1–9 (2018).

[142]J. Müller, U. Schröder, T. S. Böscke, I. Müller, U. Böttger, and J. Mu, "Ferroelectricity in yttrium-doped hafnium oxide", **114113**, 1–6 (2011).

[143]T. Shimizu, "Ferroelectricity in HfO_2 and related ferroelectrics", Journal of the Ceramic Society of Japan **126**, 667–674 (2018).

[144]V. V. Lemanov, E. P. Smirnova, P. P. Syrnikov, and E. A. Tarakanov, "Phase transitions and glasslike behavior in $Sr_{1-x}Ba_xTiO_3$", Physical Review B **54**, 3151–3157 (1996).

[145]R. Batra, T. D. Huan, G. A. Rossetti, and R. Ramprasad, "Dopants promoting ferroelectricity in hafnia: insights from a comprehensive chemical space exploration", Chemistry of Materials **29**, 9102–9109 (2017).

[146]T. Shimizu, T. Mimura, T. Kiguchi, T. Shiraishi, T. Konno, Y. Katsuya, O. Sakata, and H. Funakubo, "Ferroelectricity mediated by ferroelastic domain switching in HfO_2-based epitaxial thin films", Applied Physics Letters **113**, 212901 (2018).

[147]S. E. Reyes-Lillo, K. F. Garrity, and K. M. Rabe, "Antiferroelectricity in thin-film ZrO_2 from first principles", Physical Review B **90**, 140103 (2014).

[148]S. Coh and D. Vanderbilt, "Structural stability and lattice dynamics of SiO_2 cristobalite", Physical Review B **78**, 054117 (2008).

[149]B. Cordero, V. Gómez, A. E. Platero-Prats, M. Revés, J. Echeverría, E. Cremades, F. Barragán, and S. Alvarez, "Covalent radii revisited", Journal of the Chemical Society. Dalton Transactions, 2832–2838 (2008).

[150]R. D. Shannon, "Revised effective ionic radii and systematic studies of interatomic distances in halides and chalcogenides", Acta Crystallographica Section A **32**, 751–767 (1976).

[151]P. D. Lomenzo, C. C. Chung, C. Zhou, J. L. Jones, and T. Nishida, "Doped $Hf_{0.5}Zr_{0.5}O_2$ for high efficiency integrated supercapacitors", Applied Physics Letters **110**, 0–5 (2017).

[152]T. Schenk, M. Hoffmann, J. Ocker, M. Pešić, T. Mikolajick, and U. Schroeder, "Complex internal bias fields in ferroelectric hafnium oxide", ACS Applied Materials and Interfaces **7**, 20224–20233 (2015).

[153]E. D. Grimley, T. Schenk, X. Sang, M. Pešić, U. Schroeder, T. Mikolajick, and J. M. LeBeau, "Structural changes underlying field-cycling phenomena in ferroelectric HfO_2 thin films", Advanced Electronic Materials **2**, 10.1002/aelm.201600173 (2016).

[154]J. Liu, S. Liu, L. H. Liu, B. Hanrahan, and S. T. Pantelides, "Origin of pyroelectricity in ferroelectric HfO_2", Physical Review Applied **12**, 034032 (2019).

[155]J. Liu, S. Liu, J.-Y. Yang, and L. Liu, "Electric auxetic effect in piezoelectrics", Physical Review Letter **125**, 197601 (2020).

[156]T. Schenk, N. Godard, A. Mahjoub, S. Girod, A. Matavz, V. Bobnar, E. Defay, and S. Glinsek, "Toward Thick Piezoelectric HfO_2-Based Films", Physical Status Solidi – Rapid Research Letters **14** (2020).

[157]S. Starschich, D. Griesche, T. Schneller, R. Waser, and U. Böttger, "Chemical solution deposition of ferroelectric yttrium-doped hafnium oxide films on platinum electrodes", Applied Physics Letters **104**, 1–5 (2014).

[158]M. J. Haun, E. Furman, S. J. Jang, H. A. McKinstry, and L. E. Cross, "Thermodynamic theory of $PbTiO_3$", Journal of Applied Physics **62**, 3331–3338 (1987).

[159]A. Kvasov, L. J. McGilly, J. Wang, Z. Shi, C. S. Sandu, T. Sluka, A. K. Tagantsev, and N. Setter, "Piezoelectric enhancement under negative pressure", Nature Communications **7**, 1–8 (2016).

[160]D. Damjanovic, M. Budimir, M. Davis, and N. Setter, "Piezoelectric anisotropy: enhanced piezoelectric response along nonpolar directions in perovskite crystals", Journal of Materials Science **41**, 65–76 (2006).

[161]W. Heywang, K. Lubitz, and W. Wersing, eds., *Piezoelectricity: evolution and future of a technology* (Springer-Verlag Berlin Heidelberg, 2008).

[162]T. S. Böscke, J. Müller, D. Bräuhaus, U. Schröder, and U. Böttger, "Ferroelectricity in hafnium oxide thin films", Applied Physics Letters **99**, 102903 (2011).

[163]A. Chouprik, M. Spiridonov, S. Zarubin, R. Kirtaev, V. Mikheev, Y. Lebedinskii, S. Zakharchenko, and D. Negrov, "Wake-up in a $Hf_{0.5}Zr_{0.5}O_2$ film: a cycle-by-cycle emergence of the remnant polarization via the domain depinning and the vanishing of the anomalous polarization switching", ACS Applied Electronic Materials **1**, 275–287 (2019).

[164]S. Dutta, P. Buragohain, S. Glinsek, C. Richter, H. Aramberri, H. Lu, U. Schroeder, E. Defay, A. Gruverman, and J. Íñiguez, "Piezoelectricity in hafnia", Nature Communications **12**, 7301 (2021).

[165]J. Roedel, W. Jo, K. T. P. Seifert, E.-M. Anton, T. Granzow, and D. Damjanovic, "Perspective on the Development of Lead-free Piezoceramics", Journal of the American Ceramic Society **92**, 1153–1177 (2009).

[166]A. L. Kholkin, E. K. Akdogan, A. Safari, P. F. Chauvy, and N. Setter, "Characterization of the effective electrostriction coefficients in ferroelectric thin films", Journal of Applied Physics **89**, 8066–8073 (2001).

[167]P. Sharma, T. J. Reece, S. Ducharme, and A. Gruverman, "High-resolution studies of domain switching behavior in nanostructured ferroelectric polymers", Nano Letters **11**, 1970–1975 (2011).

[168]I. Katsouras, K. Asadi, M. Li, T. B. Van Driel, K. S. Kjær, D. Zhao, T. Lenz, Y. Gu, P. W. Blom, D. Damjanovic, M. M. Nielsen, and D. M. De Leeuw, "The negative piezoelectric effect of the ferroelectric polymer poly(vinylidene fluoride)", Nature Materials **15**, 78–84 (2016).

[169]M.-A. Dubois and P. Muralt, "Properties of AlN thin films for piezoelectric transducers and microwave filter applications", Applied Physics Letters **74** (1999).

[170]P. Marton and C. Elsässer, "First-principles study of structural and elastic properties of the tetragonal ferroelectric perovskite $Pb(Zr_{0.50}Ti_{0.50})O_3$", Physica Status Solidi (b) **248**, 2222–2228 (2011).

[171]F. Tasnádi, B. Alling, C. Höglund, G. Wingqvist, J. Birch, L. Hultman, and I. A. Abrikosov, "Origin of the anomalous piezoelectric response in wurtzite $Sc_{1-x}Al_xN$ alloys", Physical Review Letter **104**, 137601 (2010).

[172]M. A. Caro, S. Zhang, T. Riekkinen, M. Ylilammi, M. A. Moram, O. Lopez-Acevedo, J. Molarius, and T. Laurila, "Piezoelectric coefficients and spontaneous polarization of ScAlN", Journal of Physics: Condensed Matter **27**, 245901 (2015).

[173]S. Manna and C. S. of Mines. Department of Mechanical Engineering, *Design and discovery of new piezoelectric materials using density functional theory* (Colorado School of Mines, 2018).